UNIVERSITY OF TURIN

Department of Medical Sciences
Doctoral School of Medical Physiopathology
Cycle XXXV

Thesis title:

*"**Radiomics in nuclear medicine and hybrid imaging for the study of heterogeneity in solid tumors: diagnostic and prognostic potential through the example of the neuroendocrine tumor model**"*

Candidate

Dr Virginia Liberini

Tutor

Prof. Desirée Deandreis

PhD coordinator:

Prof. Franco Veglio

Scientific Sector: Nuclear Medicine MED/12
Doctoral Course (D.M.45/2013)

ACADEMIC YEARS 2019-2022

INDEX

CHAPTER 1

1. INTRODUCTION

In recent years, new diagnostic and therapeutic techniques have created significant advances in cancer treatment, but also new challenges. Advances in technology with the development of new diagnostic tools, such as positron emission tomography / computed tomography (PET/CT), and treatment modalities are driving developments in cancer care [1]. PET/CT is undoubtedly an evolving technology also thanks to the development of new target-specific radiopharmaceuticals. Although [18F]F-fluorodeoxyglucose ([18F]F-FDG) undoubtedly remains the milestone of the PET/CT method, the development of new radiopharmaceuticals has brought about considerable benefit for better diagnostic framing of many pathologies: as in the case of prostate cancer thanks to the development of radiopharmaceuticals linked to choline or prostate-specific membrane antigen (PSMA) and in the case of neuroendocrine tumors thanks to the development of [68Ga]Ga-DOTA-peptides.

Over the last decade, technology has also led to an important evolution in the diagnostic field: from a purely diagnostic and qualitative tool, oncological imaging has acquired a central role in the context of personalized medicine. In fact, since the beginning of this decade, advances in hardware and software have made it possible to identify and use semi-quantitative and quantitative data extrapolated from imaging in clinical practice for the study of tissue pathophysiology with what is known as 'radiomics'. In medical imaging, radiomics is a relatively new and rapidly evolving field; this discipline, through the use of a large number of complex mathematical functions, makes it possible to extend the field of evaluation of images acquired by any imaging method, radiological and/or nuclear medical [2, 3].

Radiomics, using bioinformatic approaches, thus makes it possible to move from a simple qualitative assessment to a more complex quantitative evaluation, providing a vast wealth of numerical data on underlying pathophysiological phenomena that are inaccessible to simple visual analysis. Radiomics applied to next-generation imaging, including PET, could make a valuable contribution in oncology with several potential

applications: differentiating benign from malignant disease, histopathological characterization, predicting response to cancer therapy and potential resistance to chemotherapy and radiotherapy, distinguishing subsets of malignancies with a better prognosis from those with a poor prognosis, recognizing patterns of post-therapy failure, assessing response to neoadjuvant treatment, and evaluating patients who may benefit from adjuvant therapy [4–7]. Radiomics might help the 'in vivo' and non-invasive assessment of tumor heterogeneity. Histopathology is crucial in tumor classification; however, the assessment of tumor aggressiveness is generally performed by biopsy of one lesion, leading to a potential grading underestimation [8], since tumor heterogeneity is both spatial (inter and intratumoral heterogeneity) and time-related (more aggressive cell clones developing over time) [9, 10]. Thus, although multiple-lesion biopsy sampling is not feasible, grading heterogeneity among primary and secondary lesions is not negligible and a non-invasive approach, such as the evaluation of PET imaging by radiomics, could support the evaluation of this heterogeneity [11].

Neuroendocrine tumors (NET) are a heterogeneous group of malignancies represented by different histological subtypes and different primary locations [12]; neuroendocrine neoplasms (NENs) encompass a broad spectrum of neoplasms ranging from well-differentiated indolent tumors to highly aggressive and poorly differentiated neuroendocrine carcinomas [13–15]. Histopathology is crucial in tumor classification and Ki-67 is currently used to define tumor grading in GEP NET [16]. New generation imaging technologies, including PET, might offer their contribute to the evaluation of tumor heterogeneity [4–6]. At present, PET imaging with [68Ga]Ga-DOTA-peptides analogs to the somatostatin (SST) is considered the state of the art to quantify SST receptors in vivo [17, 18], while [18F]F-FDG PET/CT is used to metabolically characterize more aggressive and higher grade NET lesions [19]. This dual approach has been recently evaluated leading to the development of the NETPET score [20]. Nevertheless, the simple in vivo quantification of receptor expression is not sufficient to characterize the biology of the tumor and the intra patients and intratumor heterogeneity. This drawback might be solved with a better characterization of tumor heterogeneity by the extraction of radiomic features (RFs), as a surrogate biomarker for NET lesions characterization [21], from the [68Ga]Ga-DOTA-peptide PET/CT [22–25].

While scientific interest in radiomics applied to PET imaging is rapidly increasing, the methodological approach needs to be validated and standardized and, thus, harmonization among protocols is needed [2, 26, 27]. Although radiomics is developing rapidly, it nevertheless requires the development of a methodology with the aim of achieving reproducibility, standardization, and prospective validation of the data collected. The application of a repeatable and reproducible method is indispensable because of the variability of the scanner hardware from different manufacturers, the radiopharmaceutical used, the injected activity, the acquisition time after injection, the acquisition time for each couch, the CT parameters used to correct the attenuation of the PET data and further technical parameters can significantly influence the collected data and the values of the extracted radiomic features [1, 25, 28–30].

Therefore, the aim of this thesis is to examine the potential technical and clinical applications of radiomics on nuclear medical imaging in the specific setting of neuroendocrine tumors.

CHAPTER 2

2.1. NEUROENDOCRINE TUMORS

Neuroendocrine neoplasms (NENs) comprise a wide variety of heterogeneous neoplasms, which originate from the diffuse neuroendocrine system and can therefore arise in anybody district. These tumors are considered rare, with an incidence of about 3-5 new cases/100,000 inhabitants/year, although new data from the *US Surveillance Epidemiology and End Results Program (SEER)* show an increase in the incidence of the disease of about 520% over the last 32 years (1973-2005), with an annual rate of 5.8% [31]. This increase in incidence can probably be attributed to the introduction of new and/or more sophisticated diagnostic tools (such as PET/CT and MRI). Although ubiquitous, these tumors most frequently affect the gastro-entero-pancreatic tract, about 33%, and the bronchopulmonary system, about 25%.

In the gastro-entero-pancreatic tract, based on SEER data, gastro-intestinal and pancreatic neuroendocrine tumors (GEP-NET) are second in frequency only to colon cancer [32–36]. They can also arise in any part of the gastro-entero-pancreatic tract, but most frequently occur in the small intestine (30.8 %), followed by the rectum (26.3 %), colon (17.6 %), pancreas (12.1 %), stomach (8.9 %) and appendix (5.7 %). The survival of patients with GEP-NET depends on the site, and the stage according to the TNM classification and the WHO histopathological classification (Table 1), which expresses both the morphological appearance of the tumor and its proliferative activity in terms of the number of mitoses and proliferation index (by assessing the Ki67 index and thus the disease grading). Further prognostic factors are somatostatin receptor expression, the tumor's spontaneous evolution speed, and the patient's age. However, the prognosis for these tumors is overall superior to that of adenocarcinoma with the same location: higher for GEP-NETs of the rectum and appendix, lower for GEP-NETs of the small bowel and pancreas, where the prognosis is associated with many concomitant variables.

Table 1. Classification and grading criteria for GEP-NENs, according to the WHO 2019 Grading Classification.

Classification	Differentiation	Nomenclature	Grade	Mitotic rate (mitoses/2 mm^2)	Ki-67 index
NETs	Well differentiated	NET, G1	Low	<2	<3%
		NET, G2	Intermediate	2-20	3-20%
		NET, G3	High	>20	>20%
NECs	Poorly differentiated	NEC, small-cell type (SCNEC)	High	>20	>20%
		NEC, large-cell type (LCNEC)	High	>20	>20%
MiNEN	MiNEN	Well or poorly differentiated	Variable	Variable	Variable

NOTE:
- *SCNEC*: small-cell neuroendocrine carcinoma; *LCNEC*: large-cell neuroendocrine carcinoma;
- *MiNEN*: mixed neuroendocrine-non-neuroendrocrine neoplasm;
- mitotic rates are determined by counting in 50 fields of 0.2 mm2;
- the *Ki-67* proliferation index is determined by counting at least 500 cells in the regions of highest labelling (hot-spots), which are identified at scanning magnification.

Neuroendocrine neoplasms of the lung are a heterogeneous group of tumors with different morphological aspects and different levels of clinical aggressiveness [37–40]. They account for about 2% of primary lung cancers. Within the NEN group, four morphological variants are identified based on epidemiological, genetic, pathological, and clinical data:

- typical carcinoid (CT): low-grade tumors; composed of cells with an organoid, trabecular, palisade or ribbon-like appearance, separated by a delicate fibrovascular stroma. The individual cells are regular and have uniform round nuclei and a modest amount of eosinophilic cytoplasm. They are characterized by < 2 mitoses/hpf and absence of necrosis;
- atypical carcinoid (AC): intermediate-grade tumors; has a histological composition remains similar to that of typical carcinoids, however they tend to show greater cell atypia, increased cellularity, nucleoli, lymphatic invasion and disorganized architecture. They are characterized by > 2-10 mitoses/hpf and/or foci of necrosis;
- large cell neuroendocrine carcinoma (NE): malignant tumors, with no notable differences in survival between them:
    - large cell neuroendocrine carcinoma (LCNEC), in this case, the cells may retain an organoid appearance, but also present with diffuse and disorganized growth. They are characterized by > 10 mitoses/hpf and extensive areas of necrosis;
    - small cell carcinoma (SCLC): in this case the epithelial cells are small, with little cytoplasm, well-defined cell borders, finely granular nuclear chromatin

(salt-and-pepper type picture), and no conspicuous nucleoli. The cells are round, oval, or spindle-shaped with significant nuclear remodeling; they grow in clusters with neither glandular nor squamous organization. The mitotic count is high and associated with the presence of numerous apoptotic detritus.

Thus, a spectrum based on the identification of four different histological subtypes results in a definite clinical prognostic scheme with precise implications for follow-up and clinical treatment (predominantly surgical in CT, multimodal in CA, predominantly chemo-radiotherapeutic in LCNEC/SCLC).

According to the World Health Organization (WHO) classifications, the grading of neuroendocrine tumors is based on analysis of the histopathological examination of the tumor cytological or biopsy specimen, which shows the morphological features of the tumor and its proliferative activity in terms of the number of mitoses or proliferation index (Ki67 index). This allows the identification of NET (neuroendocrine tumor) for low- to intermediate-grade tumors, G1 and G2, and the identification of NEC (neuroendocrine carcinoma) for high-grade tumors, G3. Based on this premise, the current WHO classifications of neuroendocrine tumors are given below (Table 2).

Table 2. WHO classification of thoracic and digestive neuroendocrine neoplasms.

	Thoracic	**WHO 2015**		**Gut**	**WHO 2010**		**Pancreas**	**WHO 2017**	
		Mitotic Index	*Necrosis*		*Mitotic Index*	*Ki67 Index*		*Mitotic Index*	*Ki67 Index*
Well-differentiated*	TC	<2/10HPF	No	NET G1	<2/10HPF	<2%	NET G1	<2/10HPF	<3%
	AC	2-10/10HPF	Yes	NET G2	2–20/10HPF	3-20%	NET G2	2–20/10HPF	3-20%
							NET G3	>20/10HPF	>20%
Poorly differentiated*	NEC	>10/10HPF	Yes	NEC	>20/10HPF	>20%	NEC	>20/10HPF	>20%
Mixed neoplasms	Combined			MANEC			MiNENs		

NOTE: *TC* typical carcinoid*, AC* atypical carcinoid*, NET* neuroendocrine tumor*, NEC* neuroendocrine carcinoma*, MANEC* mixed adenoneuroendocrine carcinoma*, MiNEN* mixed neuroendocrine/non-neuroendocrine neoplasm*, HPF* high-power field.
**Morphologically well-differentiated or poorly differentiated*

NENs are usually sporadic in nature; although they may be related to certain hereditary syndromes, such as multiple endocrine neoplasia type 1 (MEN 1), type 2 (MEN 2), Von Hippel-Lindau syndrome (VHL), neurofibromatosis type 1 and tuberous sclerosis [15].

For all neuroendocrine tumors, specific neuroendocrine markers are used to determine the neuroendocrine tumor phenotype: such as chromogranin A (CgA) and synaptophysin, the most reliable for sensitivity and specificity, but also CD56, PGP 9.5, TTF-1, CDX-2, Isl-1, PDX-1 and neuro-specific enolase (NSE) [41, 42].
A remarkable feature of NENs is the expression of somatostatin receptors (SSTRs) in well-differentiated tumors, with SSTRs type 1 and type 2 being present in the vast majority of NENs, while SSTRs type 3 and type 5 are expressed by approximately 60% of cases, and SSTR type 4 only rarely [43].
The knowledge of histopathological and molecular characteristics of NENs as well as the availability of more accurate diagnostic tools and therapeutic options allow for a personalized approach to these diseases, with potential benefits in treatment response and survival. *In-vivo* imaging of SSTR expression in NENs is feasible since the development of [^{123}I]I-labelled tyr-3-octreotide in 1989 [44, 45], when Krenning et al. documented for the first time positive [^{123}I]I-labelled tyr-3-octreotide scans obtained for two meningiomas, two gastrinomas and one carcinoid [45]. In the last decade, the accuracy in NENs detection by [^{111}In]In-pentetreotide (Octreoscan®) single-photon emission computed tomography / computed tomography (SPECT/CT) has been surpassed by [68Ga]Ga-DOTA-labelled somatostatin analog PET/CT. Compared to SPECT radiopharmaceuticals, somatostatin analog PET/CT has also the advantage of lower radiation exposure, earlier and shorter acquisition times, higher spatial resolution, and the possibility of tracer uptake quantitation [46, 47].

The main [68Ga]Ga-DOTA-labelled somatostatin analogues clinically available today are [68Ga]Ga-DOTA-TATE (DOTA, Tyr(3)-octreotate), [68Ga]Ga-DOTA-NOC (DOTA,1-Nal(3)-octreotide), and [68Ga]Ga-DOTA-TOC (DOTA, D-Phe1, Tyr (3)-octreotide). Currently, these are the most promising radiotracers for the study of well-differentiated NENs (G1 and G2 with low-intermediate levels of the ki67 index, <10%). While, in case of high levels of ki67 index (>10%), high-grade NET (G3), NEC, or in case of [68Ga]Ga-DOTA-peptide imaging of SSTR-negative lesions, patients are also candidates for [18F]F-FDG PET/CT [39, 48–50]. [18F]F-FDG is a glucose analog in

which a fluorine atom replaces the OH group at position 2; the tracer accumulates in the intracellular space in the form of [18F]F-FDG-6PO4 proportionally to the cellular requirement for this metabolic substrate. Although generally slow-growing and with a low rate of glucose metabolism, neuroendocrine tumors with a high proliferation index (ki67) and a low degree of differentiation are more likely to be detected by [18F]F-FDG PET/CT scan, and the presence of FDG-positive lesions is associated with a worse disease outcome [51].

Recently, Chan et al. [20] proposed a staging protocol by means of multiple imaging with [18F]F-FDG PET/TC and [68Ga]Ga-DOTA-peptides, resulting in the formulation of a new score, the "NETPET grade" (Figure 1), which could help in the prognostic evaluation of the patient and the resulting therapeutic decisions. However, at present, this protocol is little used: in fact, imaging with multiple tracers, although potentially providing the most accurate biological characterization of the disease, is not feasible in all patients and should only be considered in selected cases.

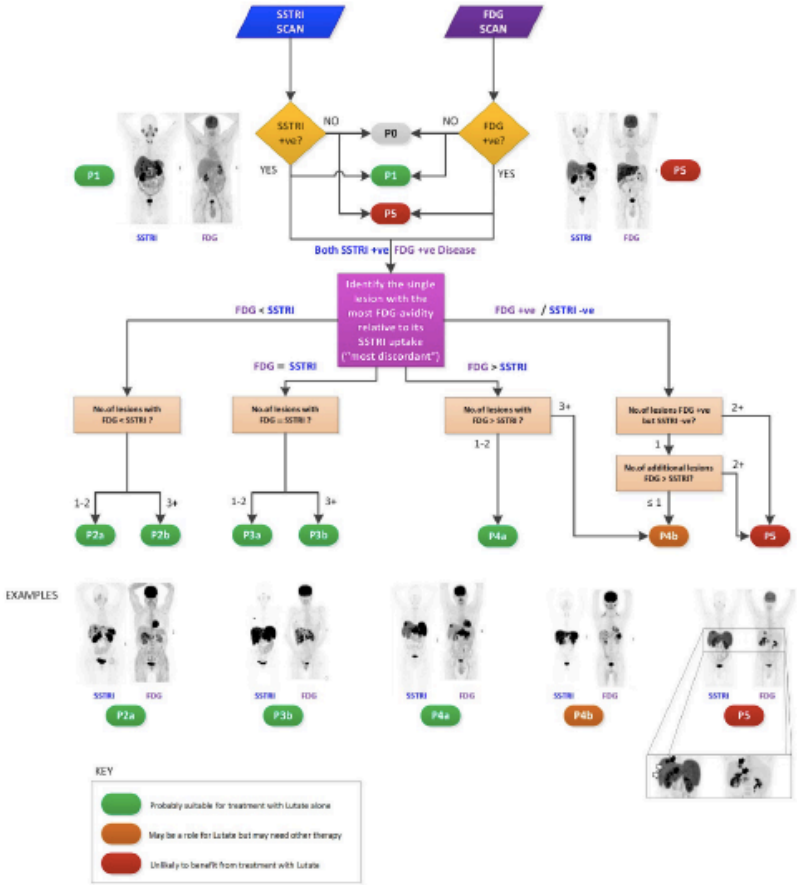

Figure 1. *NETPET grading flowchart. Chan, David LH et al.* ***Dual Somatostatin Receptor/FDG PET/CT Imaging in Metastatic Neuroendocrine Tumours: Proposal for a Novel Grading Scheme with Prognostic Significance.*** *Theranostics (2017): 1149–1158. PMC. Web. 20 May 2018.*

This drawback might be solved with a better characterization of tumor heterogeneity by the extraction of RFs, as a surrogate biomarker for NET lesions characterization, from both [68Ga]Ga-DOTA-labelled somatostatin analogs and/or [18F]F-FDG PET/CT [21–25].

Nuclear medical imaging provides indispensable information for staging, monitoring, and treatment choice: - detect the primary lesion, its local extension, and relationship with surrounding structures; - staging according to TNM in order to assess the best surgical and/or pharmacological therapeutic approach; - evaluate the response to therapy and the eventual need for a change of treatment during follow-up; - provide an indirect measure of cell differentiation through [68Ga]Ga-DOTA-peptide PET/CT; - identify patients who are candidates for treatment with cold and hot somatostatin analogs (Peptide Receptor Radionuclide Therapy - PRRT - based on the use of [177Lu]Lu-DOTA-labelled somatostatin analogs) [52–55]. As mentioned above, the application of a radiomic approach could implement the information extracted from PET/CT imaging in each of these settings.

2.2. RADIOMIC

Although the PET/CT examination can be evaluated by qualitative analysis exclusively, the development of effective methods for the measurement of a radiopharmaceutical's quantitative distribution and uptake into the disease site began to appear of great importance.

The most effective and simple method is a semi-quantitative dimensionless parameter, the Standardised Uptake Value (SUV), which has provided a measure that is widely applicable in clinical routine. The SUV is calculated according to the following formula:

$$\mathbf{SUV} = \frac{\text{Detected activity (Bq) / gr of tissue}}{\text{Injected activity (Bq) / body weight (gr)}}$$

This parameter expresses the ratio between the amount of radiopharmaceutical accumulated in a target lesion (defined as volume in ml or weight in grams) and the amount of tracer that would hypothetically be present in a region of equal volume if the

tracer was homogeneously distributed throughout the body. Therefore, an SUV value > 1 indicates a preferred concentration in a defined lesion, on the contrary, an SUV value < 1 indicates a lower concentration in the target lesion than what we might consider a background radioactive concentration. SUV requires accurate measurement of administered activity, injection time, scan time, and patient weight and is influenced by PET scanner performance characteristics and image reconstruction factors.

Radiomics allows to increase in the number of semi-quantitative and quantitative parameters that can be quantified by extracting a large number of quantitative characteristics (features) from medical images using data-characterization algorithms and bioinformatics approaches [1, 2, 22, 28, 29]. These features, namely radiomics features (RFs), have the potential to uncover disease characteristics that fail to be appreciated by the naked eye, leading to the possibility to quantify specific tumor attributes and phenotypes. RFs can be divided into morphological features, such as compactness and sphericity; first-order features, which describe the distribution of voxel intensities within the specified tumor volume; second-order static features or texture features, which can characterize the spatial interrelationships of intensity between tumor voxels; higher-order statistical features [56, 57]. Distinctive RFs can help to better describe the biological behavior of the disease in different settings and, consequently, to develop more accurate decision support models by combining medical imaging data (non-invasive and whole-body biomarkers) with other patient characteristics, such as molecular and histopathological tumor characteristics [1].

Most of the additional parameters used by radiomics in PET/CT imaging concern intra-tumor heterogeneity, although other features related to shape or other parameters have also been described. The most used methods include statistical methods (first-, second-, and high-order), fractals, or transformation-based approaches, which convert the spatial information of an image into frequency-scale (Fourier) information [58].

First-order statistical functions do not capture any spatial information but represent global measurements of a tumor. These include:

- standard parameters such as SUV, metabolic volume (MV) or somatostatin receptor-expressing tumor volume (SRETV) and total glycolysis of the lesion (TLG=MV*SUVmean) or total lesion somatostatin receptor expression (TLSRE=SRETV*SUVmean);

- parameters extrapolated from the voxel intensity frequency histogram, such as global heterogeneity (with data such as skewness and kurtosis describing the shape of the histogram), entropy (describing the randomness of voxel values), and energy or uniformity (describing the homogeneity of voxel values).

Second-order and high-order statistical functions, on the other hand, contain information on the spatial relationships between the intensities of more than two voxels and derive co-occurrence or difference matrices to provide local or regional measures of heterogeneity, often referred to as 'texture analysis'. In addition, the use of run-length encoding (RLE) algorithms and dimensional matrices provide information on a set of voxels or a group of similar voxels for a given aspect.

Commonly used second-order features include entropy, energy, homogeneity, and contrast (which should not be confused with first- or high-order features bearing the same names), these features measure the relationships between pairs of voxels. High-order features include those extrapolated from the grey tone difference matrices between neighboring voxels, such as coarseness (coarseness), contrast (contrast), busyness (busyness), and complexity (complexity). All these features are designed to best represent the human perception of heterogeneity and texture within an image.

Despite the vast potential of radiomics in the nuclear medicine field, their application in clinical practice is still challenging and not yet validated; indeed, several factors can affect the resulting quantitative imaging biomarker measurement. Also, imaging analysis procedures such as tumor segmentation methods, grey-level intensity discretization, and image reconstruction algorithms can affect the robustness, repeatability, and reproducibility of these variables and their results [2, 26, 57, 59–61].

Recently, several documents have been provided by the scientific community to increase the robustness of these tools, such as the Radiomics Quality Score (RQS) [1], a point-based system that guides the researcher to use a rigorous methodological approach for performing radiomics, and the Imaging Biomarker Standardization Initiative (IBSI) [58], that aims to provide image biomarker nomenclature and definitions, benchmark data sets, and benchmark values to verify image processing and image biomarker calculations, as well as reporting guidelines, for high-throughput image analysis. In a recent review, Zwanenburg [26] identified and described the main pitfalls of data analysis that affect the reproducibility and generalizability of radiomics studies, dividing them into macro-areas: patient selection (sample size, injected

radiopharmaceutical activity, patient movement, etc.), image acquisition (characteristics of the tomograph and type of acquisition used), image reconstruction (number of iterations, subsets, etc.), segmentation, image processing, image biomarker computation, and modeling. In 2022, as a result of a cooperative effort between the European Association of Nuclear Medicine (EANM) and the Society of Nuclear Medicine and Molecular Imaging (SNMMI), new guidelines have been developed with the aim of providing current best practices and recommendations for relevant aspects of radiomic analyses, including study design, quality assurance, data collection, the impact of acquisition and reconstruction, detection and segmentation, standardization and implementation of features, as well as appropriate modeling schemes, model evaluation and interpretation [62].

These recommendations are increasing researchers' understanding of the more technical aspects of radiomics, leading to a gradual harmonization and standardization of these approaches, making radiomics clinical future application more than just a hypothetical mirage.

CHAPTER 3

3. AIMN OF THE STUDY

Considering the data presented above, the aim of this doctoral project was to analyze the use of radiomics in neuroendocrine neoplasms.

The objectives of this project are:

- to develop a repeatable and reproducible methodology for the radiomic analysis of PET/CT images with the aim of achieving reproducibility, standardization, and prospective validation of the collected data. The application of a repeatable and reproducible method is indispensable, because the variability of the scanner hardware from different manufacturers, the radiopharmaceutical used, the injected activity, the acquisition time after injection, the acquisition time for each couch, the CT parameters used for the attenuation correction of the PET data, and further technical parameters can significantly influence the collected data and the values of the extracted RFs;
- to assess the impact on PET image quantification of different image reconstruction methods;
- to verify if there is a correlation between texture parameters extracted from PET/CT imaging and histopathological data in staging neuroendocrine tumors;
- to verify if there is a correlation between texture parameters extracted from PET/CT imaging and prognostic indices of disease already known or under investigation (clinical and laboratory data and immunohistochemical and genetic features);
- to identify, in association with prognostic data already known in the literature, the package of texture parameters that are indicators of tumor aggressiveness, which may help the diagnostic/therapeutic decision-making process by diversifying the different tumor clusters with different biological and clinical behavior;
- identifying parameters and indicators that can help and predict response to therapy, with a focus on PRRT.

CHAPTER 4

4. TECHNICAL STUDIES

4.1. DEVELOPMENT OF 3D-PRINTED INSERTS FOR NEMA-PHANTOM SIMULATING NECROTIC TUMOR LESIONS FOR THE EVALUATION OF REPRODUCIBILITY OF PET/CT RADIOMIC FEATURES

4.1.1. Publication details

Liberini V. et al. ***Development of 3D-printed inserts for NEMA-phantom simulating necrotic tumor lesions for the evaluation of reproducibility of PET/CT radiomic features*** Abstracts book of the Annual Congress of the European Association of Nuclear Medicine – EAMN Annual Congress 2022 - TROP (Top Rated Oral Presentation) Session: Radiomics - Oral Presentation. Annual Congress of the European Association of Nuclear Medicine October 15-19, 2022 Barcelona, Spain. Eur J Nucl Med Mol Imaging 49 (Suppl 1), 1–751 (2022). https://doi.org/10.1007/s00259-022-05924-4

4.1.2. Introduction and aim

Radiomic features (RFs) are quantitative features extracted from medical images that can provide disease information undetectable to the human eye, improving the clinical decision support system. Many variables influence the robustness of RFs and limit their use. In this study, we investigated the use of a phantom with 3D-printed inserts, simulating necrotic tumor lesions, to analyze the impact of different reconstruction parameters and different radionuclides on the reproducibility of PET-RFs.

4.1.3. Material and Methods

A tumoral lesion with a necrotic core extracted from a real PET/CT image served as a model to create the insert. The lesion was segmented manually using LifeX software, and the NIFTI-file of the segmented lesion was converted to an STL-file using ITK-snap software. Finally, the insert was created on the free-web-app Tinkercard using the STL-file and creating a proper stem and screw for screwing the insert onto the phantom.

The transparent resin (FormLabs Standard Resin Cartridges Clear) insert was printed with the Form3+ 3D-printer (FormLabs) in six different sizes (maximum size of 54 mm), as shown in Figure 2.

Figure 2. *The figure schematically shows the steps of lesion construction: from the segmentation of the PET image with LIFEx, to the creation of the lesions with TINKERCARD and their printing with the 3D resin printer.*

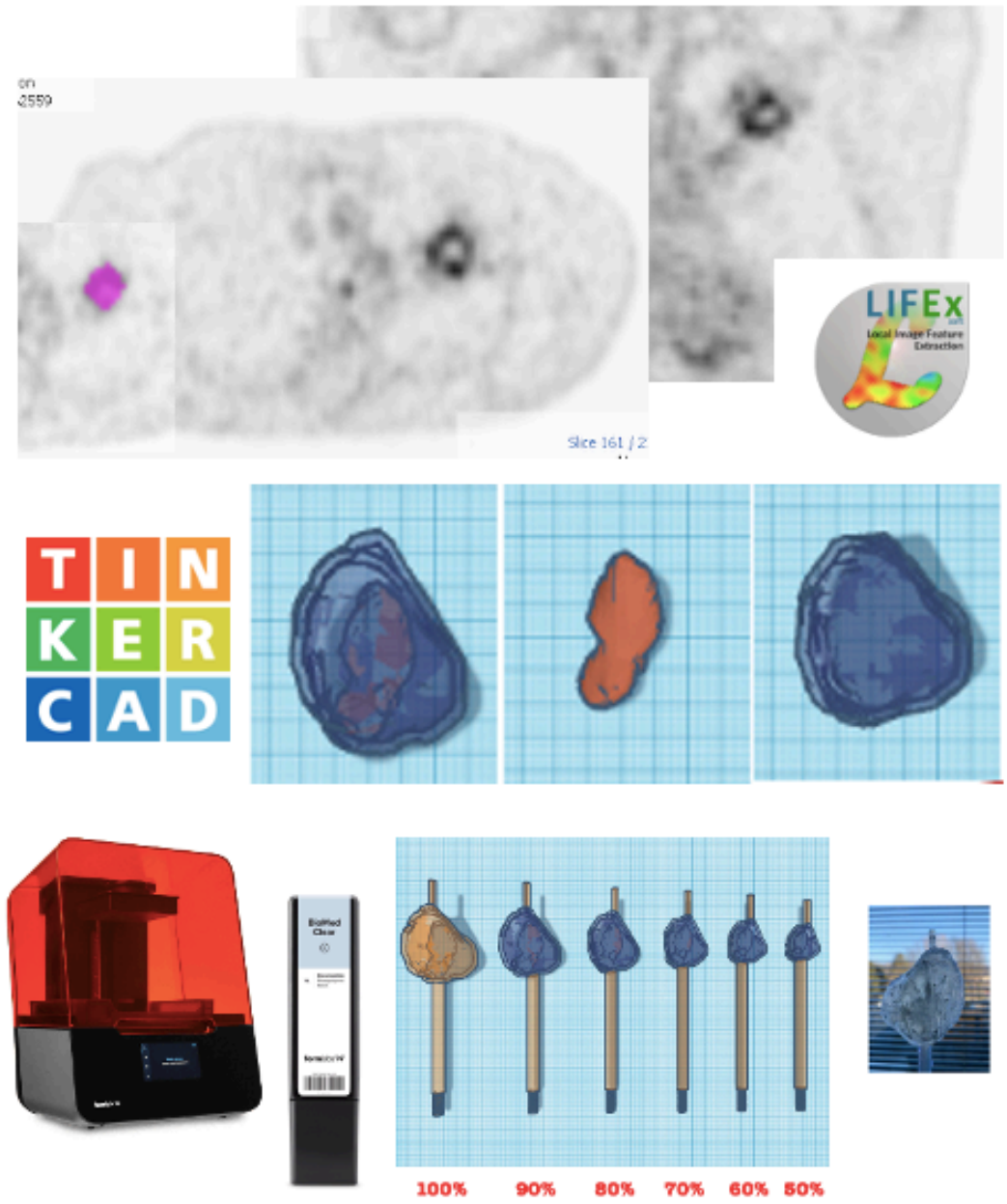

The inserts were placed in the NEMA NU 2-2012 IQ phantom and scanned twice with two different radioisotopes ([18F]F and [68Ga]Ga) solutions. The lesions were filled with the same activity solutions of 21 MBq/l and the large background compartment of the NEMA IQ phantom with5.3 MBq/l. Phantom scans were reconstructed with different parameters (acquisition time: 1.5-5 min, iterations: 3-10), as shown in Figure 3.

Figure 3. *The figure shows the 3D-printed inserts placed in the NEMA NU 2-2012 IQ phantom and scanned with [18F]F- and [68Ga]Ga solutions, respectively.*

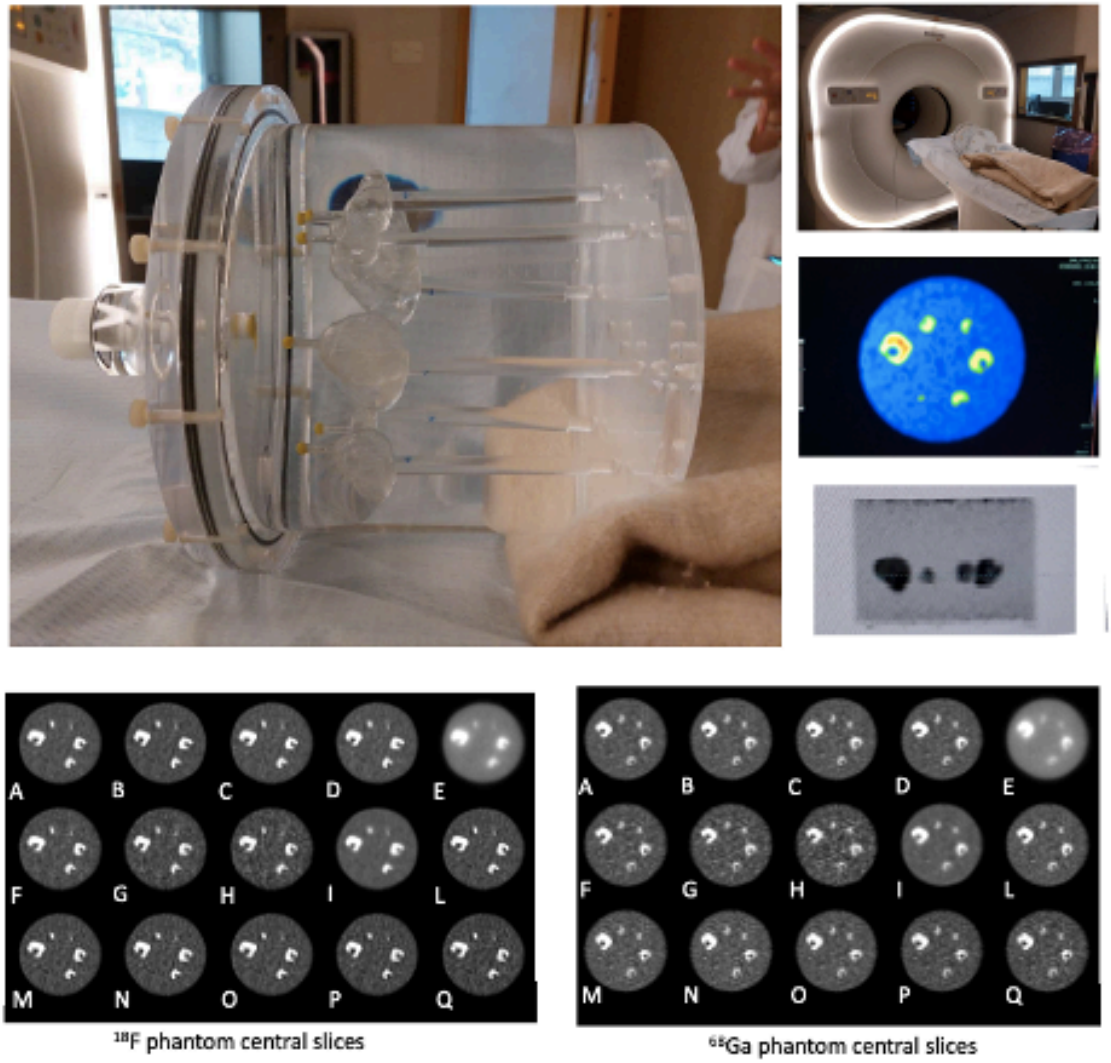

^{18}F phantom central slices

^{68}Ga phantom central slices

The images were analyzed and segmented by a nuclear physician and 52 RFs were extracted with LifeX software. Relative trends of RFs and coefficients of variation (COV) were analyzed. Wilcoxon tests were applied to assess the differences between the RF associated with the two radioisotopes.

4.1.4. Results

The majority of RFs were found to be sensitive to variations in the reconstruction parameters. Among the acquisition and reconstruction parameters, for both radioisotopes with an equal number of iterations, the number of subsets had the major impact on RFs, with COV greater than 50% for 13 RFs.

Relative trends of RFs for different iterations showed in most cases a large variation applying from 3 to 5 iterations and low variation applying from 5 and 10 iterations, regardless of the volume of the inserts, as shown in Figure 4.

Figure 4. *The impact of iterations on the RFs stability for each 3D-printed inserts for [18F]F- and [68Ga]Ga acquisition, respectively.*

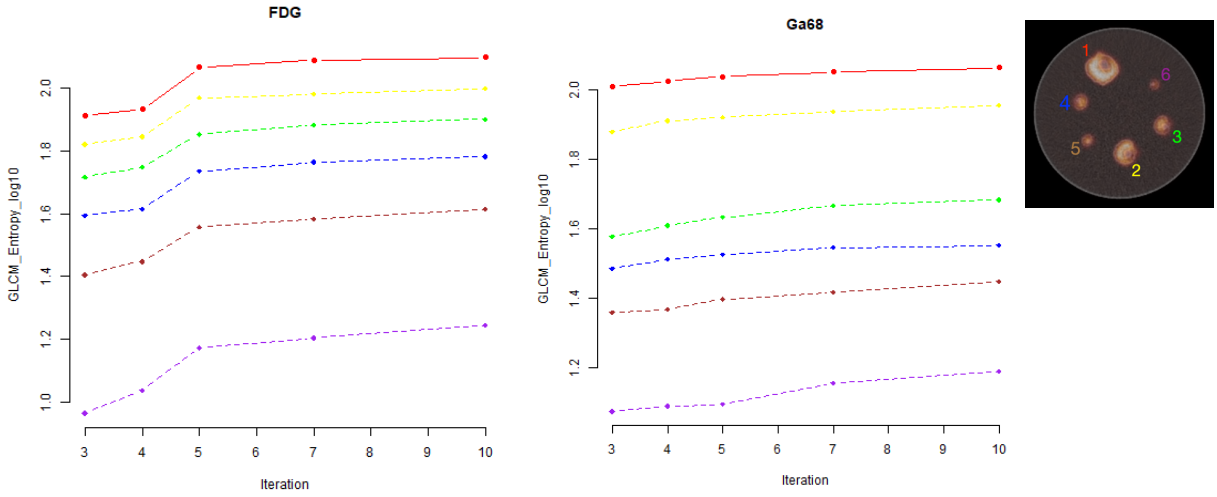

For different acquisition times, most RFs showed COV <20%. Significative differences between [18F]F- and [68Ga]Ga-RFs were observed for 14 RFs (4 conventional and 10 texture RFs).

Pearson correlation coefficients greater than 0.8 between RFs values and insert volumes were obtained for 75% of RFs for both radioisotopes.

4.1.5. Discussion and conclusion

These implemented and user-friendly 3D-printed inserts for NEMA-phantom allow to evaluate the impact of different acquisition and reconstruction parameters on RFs. This approach appears promising for the standardization of PET protocols and the harmonization of data in multicenter radiomic studies.

4.2. IMPACT OF SEGMENTATION AND DISCRETIZATION ON RADIOMIC FEATURES IN 68Ga-DOTA-TOC PET/CT IMAGES OF NEUROENDOCRINE TUMOR

4.2.1. Publication details

Liberini V. et al. ***Impact of segmentation and discretization on radiomic features in 68Ga-DOTA-TOC PET/CT images of neuroendocrine tumor.*** EJNMMI Phys. 2021 Feb 27;8(1):21. doi: 10.1186/s40658-021-00367-6. PMID: 33638729; PMCID: PMC7914329.

4.2.2. Introduction and aim

While scientific interest in radiomics applied to PET imaging is rapidly increasing, the methodological approach needs to be validated and standardized and, thus, harmonization among protocols is needed [2, 26, 27]. Indeed, imaging analysis procedures such as tumor segmentation methods, grey-level intensity discretization and image reconstruction algorithm can affect the RFs [2, 26, 57, 59–61]. Robustness analysis measures variability of RFs with respect to these factors. The identification of robust RFs for [68Ga]Ga-DOTATOC PET-CT is fundamental, since this innovative modality might be used as prognostic and predictive tool for evaluating tumor heterogeneity in NEN. To our knowledge there is only one study evaluating the robustness of RFs in function of image acquisition and reconstruction parameters for [68Ga]Ga-DOTA-peptides PET/CT [63], while the extraction of RFs and the assessment of RFs robustness in [18F]F-FDG PET/CT imaging has been broadly explored [64–68].

The objective of this study was to evaluate the robustness of RFs in function of segmentation methods and discretization settings in [68Ga]Ga-DOTATOC PET/CT images.

4.2.3. Material and Methods

270 consecutive patients affected by NEN referred to our institution to perform [68Ga]Ga-DOTATOC PET/CT between February 2017 and July 2019 were reviewed

(IRB protocol: CS2/477), in accordance with the procedure guidelines for PET imaging [48, 69, 70]. The inclusion criteria of the present study were: 1) histologically proven NEN; 2) patients who underwent [68Ga]Ga-DOTATOC PET/CT for staging in treatment-naïve patients or restaging after surgery; 3) willing to sign an informed consent form (ICF). Exclusion criteria were 1) age < 18 years; 2) previous systemic therapies. Forty-nine patients with a total of 60 lesions matched the inclusion criteria and were considered in this analysis. Primary tumor sites were GEP-NET, lung NET and others NET in 77.5% (38/49), 18.4% (9/49) and 4.1% (2/49) of cases, respectively.

For each lesion, a three-dimensional volume of interest (VOI) was manually delineated (VOI_m), slice-by-slice, in the OSEM PET image by four nuclear medicine physicians, by using the software LIFEx v. 4.81 (IMIV/CEA, Orsay, France - www.lifexsoft.org) [71]. For each VOI, three different thresholds were applied corresponding to the 20, 30 and 40% of the maximum SUV of the VOI, obtaining VOI_{20}, VOI_{30} and VOI_{40}, respectively [72, 73]. All lesions were also contoured with a semi-automatic edge-based (SAEB) method, using a MATLAB (MathWorks) homemade code, based on the active contour model proposed by Chan and Vese [74], as shown in Figure 5.

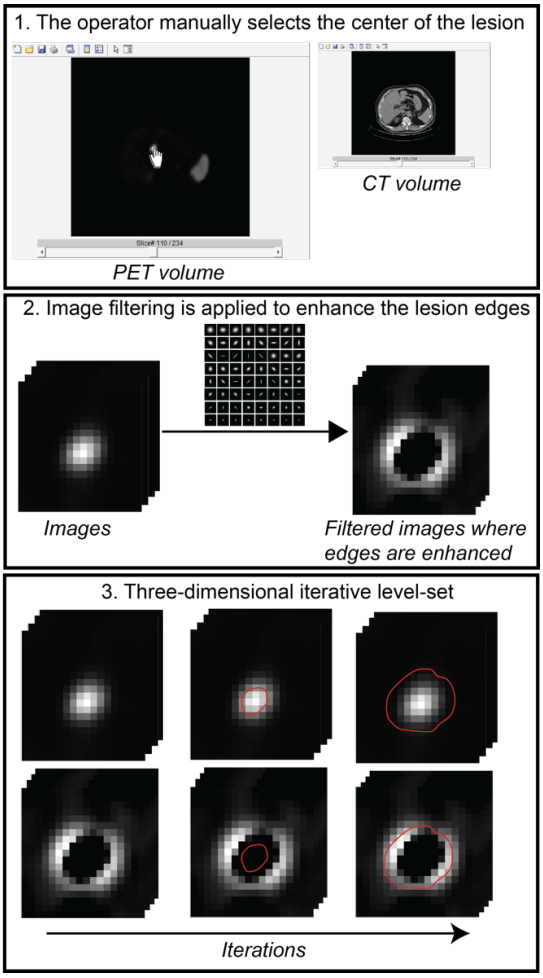

Figure 5. *Semi-automatic edge-based (SAEB) algorithm workflow. The algorithm requires the intervention of an operator to insert the central point of the lesion (1) through an interface created in MATLAB, the operator can view both the PET and the CT images separately. As a second step, edge preserving filters are applied to the image to emphasize the edge of the lesion (2) and, after that, and a level-set is used which is a shape that evolves iteratively over the image (3). The level-set acts both on the original image of the lesion and on the filtered image in which the contours are highlighted. The iteration 0 of the level set, which would be the initialization, is the center of the lesion indicated by the operator. The final outline of the lesion is achieved at the end of the process.*

Fifty-two RFs were extracted, using LIFEx in agreement with the Imaging Biomarker Standardization Initiative (IBSI) [58] description, applying different intensity rescale factors for gray-level discretization: two absolute (AR60=0-60, AR80=0-80) and one relative (RR=min-max of the VOI SUV). Dice similarity coefficient (DSC) was calculated to quantify agreement between different segmentation methods. STAPLE algorithm was used to compute the probabilistic estimate of the true segmentation from manual masks. The impact of different parameters on RFs was assessed by Intra-class Correlation Coefficients (ICC).

4.2.4. Results

DSC mean value was 0.75 ±0.11 (0.45–0.92) between SAEB and STAPLE and 0.78 ±0.09 (0.36–0.97) between the four manual segmentations.

1) Robustness of RFs to segmentation

1A) using no SUVmax threshold and applying the 3 intensity discretization settings:

Setting no threshold and applying the three different intensity rescale factors (AR60, AR80 and RR), 65.3% of RFs showed high robustness to segmentation using both AR60 and AR80 (7/10 conventional, 3/6 histogram, 2/4 shape and 22/32 textural) vs. 28.9% using RR intensity rescale factor (7/10, 0/6, 2/4, 6/32). The following RFs showed a loss of robustness applying the relative intensity rescale factor: HISTO_Entropy (both _log 10 and_log2), HISTO_Energy, GLCM (homogeneity, energy, contrast and dissimilarity), all the GLRLM features with the exception of RLNU, all the NGLDM features except from coarseness, the majority of GLZLM features with the exception of LZHGE, GLNU and ZLNU.

1B) using 40% SUVmax threshold and applying the 3 intensity discretization settings:

Using a 40% SUVmax threshold and applying the three different intensity rescale factors (AR60, AR80 and RR), the robustness of RFs to segmentation increased (ICC > 0.9 for 86.5%, 82.7% and 65.3% applying AR60, AR80 and RR respectively) but with a similar trend to the previous results.

1C) using AR80 and applying different SUVmax thresholds:

Setting intensity rescale factor to 0-60 SUV and applying different SUVmax thresholds (no threshold, 20, 30 and 40%), the percentage of highly robust RFs to segmentation

were 65.3%, 78.8%, 80.8% and 86.5% for no threshold, VOI_{20}, VOI_{30} and VOI_{40} respectively. An increase of the SUVmax threshold produced a substantial increase of ICC of the following features: SHAPE_Sphericity, SHAPE_Compacity, GLCM_Correlation, all GLRLM features, NGLDM_Coarseness, NGLDM_Contrast and GLZLM_ZP. On the contrary, the following features decreased their ICC values: HISTO_Kurtosis, HISTO_ExcessKurtosis, GLZLM_LZE, GLZLM_SZLGE and GLZLM_LZLGE.

2) Robustness of RFs to intensity discretization settings

2A) for each segmentation applying no SUVmax threshold:

Comparing the five VOI delineations (four operators and SAEB) and applying no SUVmax threshold (Figure 6), median value of ICC for intensity rescale factors was > 0.9 for the conventional and shape features and for HISTO_Skewness, HISTO_Kurtosis, HISTO_ExcessKurtosis, GLCM_Correlation, GLRLM_RLNU and GLZLM_GLNU. Overall, the percentage of highly robust features was 40.4% (10/10 conventional, 3/6 histogram, 4/4 shape and 3/32 textural). The majority of the remaining textural features showed poor robustness to discretization settings except for NGLDM_Coarseness which had a median ICC > 0.8.

2B) for each segmentation method applying 40% SUVmax threshold:

After increasing the isocontouring threshold (from no threshold to 40% SUVmax threshold) only GLCM_Correlation resulted to be highly robust among textural features. The rest of textural features remained were poorly robust (median ICC < 0.5) except from GLRLM_RLNU, NGLDM_Coarseness and GLZLM_GLNU.

3) Robustness of RFs to SUVmax threshold

Setting AR60 as intensity rescale factor, 51.9% of RFs (5/10 conventional, 3/6 histogram, 0/4 shape and 19/32 textural) showed high robustness to different SUVmax thresholds (no threshold, 20, 30 and 40%). Changing the intensity rescale factor to a relative one (RR), only seven RFs resulted to be highly robust: five of them were conventional (SUVstd, SUVmax, SUVpeak 0.5 and 1 mL, CONV_TLSRE) and two textural (NGLDM_Coarseness and GLZLM_ZLNU).

4.2.5. Discussion and conclusion

The major findings of our study are as follows: (a) quantitative comparison between a semi-automatic edge-based (SAEB) algorithm and manual segmentation showed a dice-coefficient similarity (DSC) of 0.75 ± 0.11 comparable to DSC between operators (0.78 ± 0.03). This results suggests that a semi-automatic algorithm might be able to substitute manual segmentation to solve operator variability; (b) the use of absolute intensity rescaling factor (AR60 and AR80) achieved higher robustness of RFs to segmentation and isocontouring thresholding than relative intensity rescaling factor; (c) increasing the SUVmax isocontouring threshold had a positive effect on RFs robustness to segmentation, the same is not true for robustness to intensity discretization settings which is higher with no SUVmax threshold.

Regarding inter-segmentation robustness, majority of RFs showed high robustness (ICC> 0.9) using absolute intensity rescale factors both AR60 and AR80. The less robust RFs was SHAPE_Sphericity, which describes the closeness of the VOI shape to a sphere and therefore is strongly sensitive to operator delineation. In line with previous studies [75], GLZLM (also called GLSZM) features and in particular the ones measuring zones with low grey-level (SZLGE and LZLGE) resulted to have a moderate robustness (ICC from 0.5 to 0.8) to segmentation. This is likely related to the lower uptake in lesions edges, where operator and SAEB segmentation showed a higher variability.

Another interesting result of our study is related to the negative impact of the relative intensity rescaling factor on the robustness to segmentation of the majority of textural features analyzed. As the rescaling is carried out according to the minimum and maximum values of the VOI, the same image is rescaled differently depending on the segmentation operator/method used, leading to high variability also in RFs values. Additional segmentation of the VOIs using a 40% SUVmax threshold mitigated the robustness decrease due to relative resampling since thresholding excluded low-grey voxels from the VOIs increasing the similarity between their minimum values. Anyway, it must be highlighted that the use of relative resampling is not recommended in PET images, as already observed in [18F]F-FDG PET/CT [76–78]. Moreover, NETs are characterized by an extremely variable expression of somatostatin receptors in [68Ga]Ga-DOTA-peptides with a corresponding broader range for SUV values (from close to 0 up to higher than 100) compared to [18F]F-FDG PET/CT, causing a greater

impact on the RR compared to AR, where the robustness of RFs is highest with AR60 comparing with AR80 at the expensive of information on voxels/lesions with an SUV uptake > 60.

When using an absolute intensity rescale factor, the SUVmax thresholding had no considerable impact on inter-segmentation ICC values of the most part of textural features. Instead, increasing SUVmax threshold increased robustness of conventional, shape and GLRLM features. In accordance with previous studies [26, 61], the impact of intensity discretization on textural features was stronger than segmentation. When using no SUVmax threshold, only four textural features resulted to be robust: GLCM_Correlation, GLRLM_RLNU, NGLDM_Coarseness and GLZLM_GLNU.

Our results suggest that the use of RFs is feasible also in [68Ga]Ga-DOTATOC PET/CT. The grey-level discretization influences the robustness of RFs, which vary depending on the use of relative or absolute resampling. The delineation of VOI had also an impact on the robustness of RFs, even if less relevant. These results suggest the needing to standardize the methodology used in the radiomic PET studies in [68Ga]Ga-DOTATOC PET/CT.

4.3. IMPACT OF PET DATA DRIVEN RESPIRATORY MOTION CORRECTION AND BSREM RECONSTRUCTION OF 68Ga-DOTATATE PET/CT FOR DIFFERENTIATING NEUROENDOCRINE TUMORS (NET) AND INTRAPANCREATIC ACCESSORY SPLEENS (IPAS)

4.3.1. Publication details

Liberini V. et al. ***Impact of PET data driven respiratory motion correction of ^{68}Ga-DOTATATE PET/CT for differentiating neuroendocrine tumors (NET) and intrapancreatic accessory spleens (IPAS).*** Sci Rep 11, 2273 (2021). https://doi.org/10.1038/s41598-020-80855-4

4.3.2. Introduction and aim

Accessory spleens are congenital foci of healthy splenic tissue that are separate from the main body of the spleen [79, 80] and are relatively common. Intrapancreatic accessory spleens (IPAS) appear as a solid contrast-enhancing mass, usually smaller than 3 cm, located within the tail of the pancreas [81–83]. Owing to their morphology and contrast characteristics at CT and MR imaging, they may be mistaken for pancreatic tumors, in particular NENs [84]. Hence, an accurate diagnosis may avoid unnecessary surgery or biopsy.

68Ga-labeled somatostatin analogue PET is the mainstay for the evaluation of the SSTR status of NEN. The biodistribution of somatostatin analogs is characterized by a physiological uptake in several organs, including spleen [85] and ectopic splenic tissue. Hence, IPAS may mimic pancreatic neuroendocrine tumors (pNET) and cause a false positive finding.

The aim of our study was to evaluate whether quantitative parameters of [68Ga]Ga-DOTATATE PET/CT can differentiate pNET from accessory spleens, including IPAS. For this purpose, the impact of novel Bayesian penalized likelihood reconstruction and respiratory data-driven motion correction of PET on quantitation were investigated [86].

4.3.3. Material and Methods

A total of 498 consecutive patients with neuroendocrine tumors (NET) who underwent [68Ga]Ga-DOTATATE PET/CT between March 2017 and July 2019 were retrospectively analyzed. Subjects with accessory spleens (n=43, thereof 7 IPAS) and pNET (n=9) were included, resulting in a total of 45 scans. PET images were reconstructed using ordered-subsets expectation maximization (OSEM) and a fully convergent iterative image reconstruction algorithm with β-values of 1000 ($BSREM_{1000}$). Indeed, BSREM increases the accuracy of lesion quantitation compared to OSEM by maximizing signal–to-noise ratio (SNR) while achieving almost full convergence [87–89]. In this study, the global strength of the regularization in BSREM (β-value) of 1000 was selected based on previous studies, analyzing the effect on image quality and considering both radionuclide properties and scanner characteristics [90–92].

A data-driven gating (DDG) technique (MotionFree^{TM}, GE Healthcare) was applied to extract respiratory triggers and use them for PET motion correction within both reconstructions. This technique utilizes a principal component analysis (PCA) to compute the spatiotemporal variation of list mode data. The algorithm provides a signal-to-noise measure of respiration-like frequencies within the data, denoted as *R-value*, that is configurable (*R-value threshold*). The determination of the *R*-value has a function of trigger: the *R*-value is measured at the end of base acquisition time for each bed position for which motion screening was prescribed and is used to make an on-the-fly decision whether motion has been detected. This then triggers the data acquisition to automatically be extended according to the prescribed acquisition time and data binning scheme used for motion correction (MC) [93]. In the default protocol, the quiescent phase of the respiratory cycle is set to 50% for motion correction, triggering an automatic data acquisition extension equaling to double the base acquisition time to preserve total count statistics. The *R*-value for triggering motion correction used for this study was $R = 10.0$ [94]. An example of IPAS uptake at PET/CT has shown in Figure 6.

Figure 6. [*68Ga]Ga-DOTATOC PET/CT showing an intrapancreatic accessory spleen mimicking a pancreatic neuroendocrine tumor. Contrast-enhanced CT image in portal-venous phase showing the lesion in the pancreatic tail (a). Contrast-enhanced CT image in arterial phase showing the enhancing lesion in the pancreatic tail. The lesion is characterized by mild [68Ga]Ga-DOTATATE uptake, more evident in OSEM-DDG (d) and BSREM-DDG (f) images (SUVmax 8.6 and 7.6, respectively) compared*

with OSEM(c) and BSREM (e) images without DDG (SUVmax 6.4 and 6.2, respectively). The PET volume of the accessory spleen is smaller in OSEM-DDG and BSREM-DDG images (980 mm and 814 mm, respectively) compared with OSEM and BSREM images without DDG (1400 mm and 1520 mm, respectively).

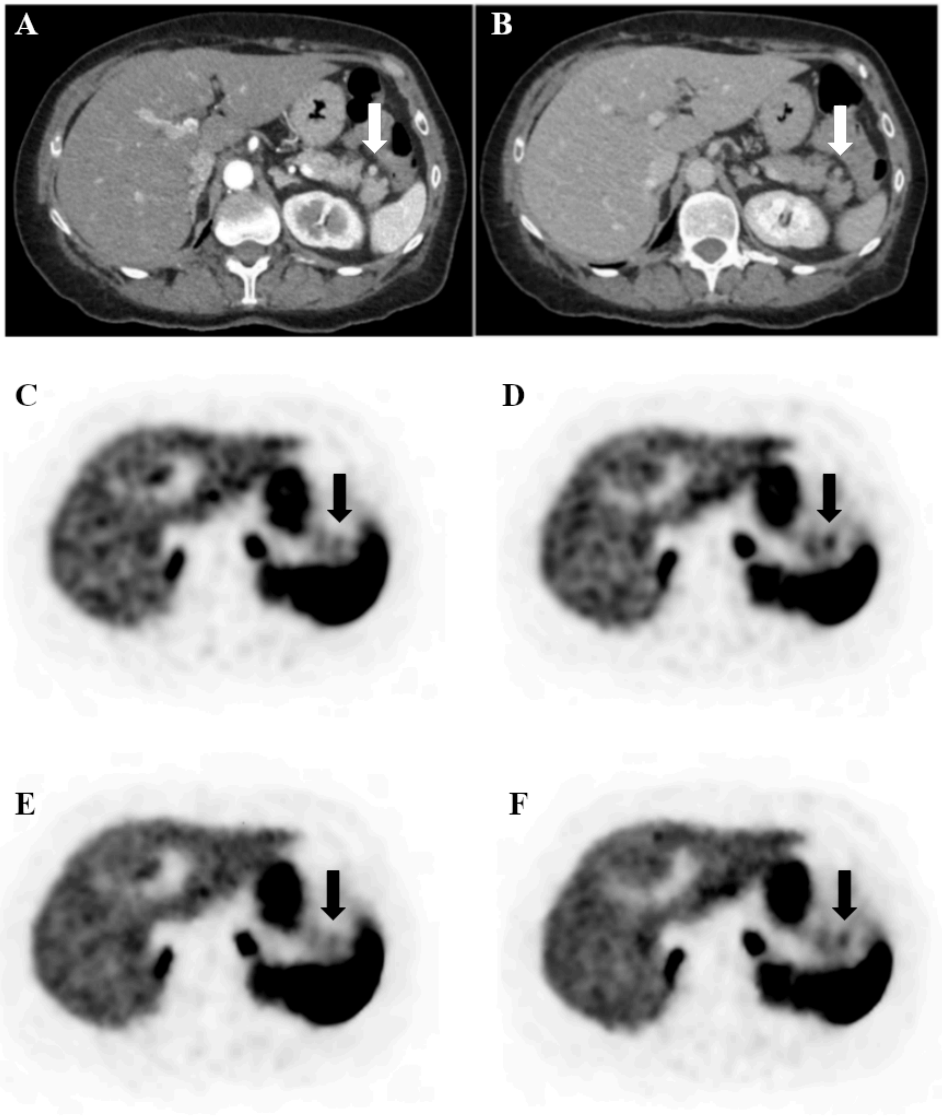

PET parameters among different samples were compared using non-parametric tests. Parameters (SUVmax, SUVmean and volume) of each sample (all accessory spleens, IPAS, pNETs, and all lesions) were compared among different reconstructions using Wilcoxon signed ranks test. The different reconstructions were compared as follows: - $BSREM_{1000}$ versus OSEM; - $BSREM_{1000}$-DDG with R = 10.0 + Q.Static™ versus $BSREM_{1000}$ half time/bed position ($BSREM_{1000}$ 1/2); - OSEM-DDG with R = 10.0 + Q.Static™ versus OSEM half time/bed position (OSEM 1/2); - $BSREM_{1000}$-DDG with R = 10.0 + Q.Static™ versus OSEM-DDG with R = 10.0 + Q.Static™.

Receiver operating characteristics (ROC) analyzed the ability of PET parameters to differentiate IPAS and pNETs.

4.3.4. Results

Out of 498 cases, accessory spleens were detected in 63 PET/CT scans of 63 patients (12.2%). Of these, PET list mode data was available in 38 scans (60.3%; mean age 56.4, range 33 - 83 years). The majority of accessory spleens (79.1%) were located perisplenic, particularly medial to the spleen (55.8%; splenic hilum, gastrosplenic ligament, splenorenal ligament), followed by an intrapancreatic location (16.3%; IPAS), and 4.6% were ectopic (splenic vessels and paracolic).

Significant correlations were observed between diameter (mm) and SUVmax of accessory spleens:

- in OSEM reconstruction with $r^2 = 0.779$, $p = 0.001$, 95% CI [0.515, 0.853] for Pearson correlation, and a coefficient of 1.266, with standard error equal to 0.167, $p = 0.001$ and $r^2 = 57.21\%$ for the linear regression equation;
- in BSREM reconstruction with $r^2 = 0.725$, $p = 0.001$, 95% CI [0.598, 0.885] for Pearson correlation, and a coefficient of 1.246, with standard error equal to 0.178, $p = 0.001$ and $r^2 = 53.43\%$ for the linear regression equation.

Out of 498 cases, pNET lesions (primary and metastatic) were detected in 9 PET/CT scans (1.8%; mean age 64.2, range 44 - 74 years), 2 with 1 accessory spleen and 1 pNET already included in the accessory spleen cohort.

Regarding the sub-cohort of patients retrospectively acquired and analyzed for the DDG reconstructions, SUVmax and SUVmean were able to distinguish pNET both from all accessory spleens and from IPAS, both in OSEM and in BSREM reconstructions, with the only exception of SUVmax of IPAS vs. pNET in OSEM. In particular, SUVmax can distinguish: - Accessory spleens vs. pNET in OSEM (p = 0.024) and BSREM (p = 0.014); - IPAS vs. pNET in BSREM (p = 0.034).

An even higher level of significance was achieved with DDG (R > 10.0), where SUVmax can distinguish: - Accessory spleens vs. pNET in both OSEM-DDG and BSREM-DDG (p = 0.002 each); - IPAS vs. pNET in both OSEM-DDG and BSREM-DDG (p = 0.033 each).

The relationship between SUVmax and PET volume for accessory spleen, IPAS and pNET separately in each reconstruction (OSEM, OSEM-DDG, BSREM and BSREM-DDG) is shown in Figure 7.

Figure 7. *Scatter plots showing the relationship between SUVmax and PET volume ofaccessory spleens, IPAS and pNETs in OSEM (a) and BSREM-DDG (b), respectively,in the sub-cohort of patients retrospectively acquired (42 accessory spleens, 6 IPAS and 8 pNET).*

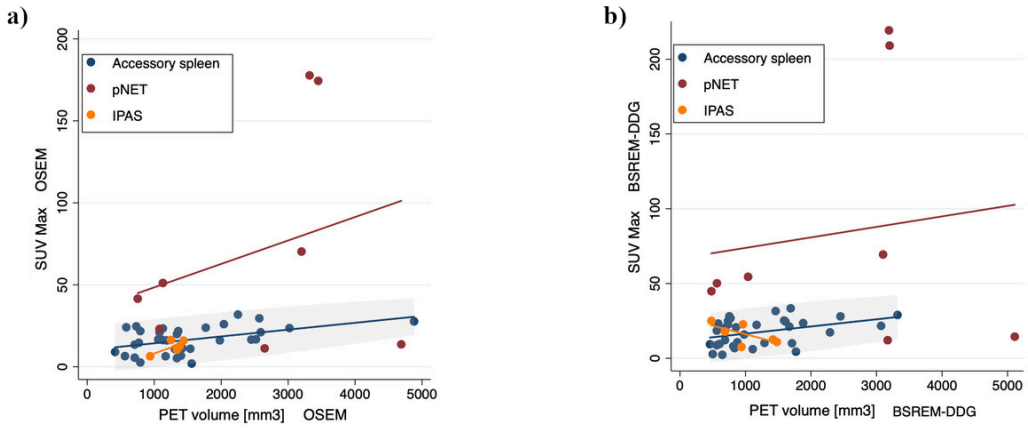

For differentiating accessory spleens and pNETs with specificity 100%, the ROC analysis yielded an AUC of 0.742 (sensitivity 56%) / 0.765 (sensitivity 56%) / 0.846 (sensitivity 62%) / 0.840 (sensitivity 63%) for SUVmax 36.7 / 41.9 / 36.9 / 41.7 in OSEM / $BSREM_{1000}$ / OSEM+DDG / $BSREM_{1000}$+DDG, respectively.

4.3.5. Discussion and conclusion

The major findings of our study are as follows: (1) both SUVmax and SUVmean are able to distinguish pNET from accessory spleens and IPAS, (2) SUVmax on the BSREM-DDG reconstruction yields the best results (p-value < 0.002 for pNET vs. accessory spleens and < 0.033 for pNET vs. IPAS), (3) different SUVmax cut-off between pNET and accessory spleens / IPAS were found for each reconstruction, (4) and BSREM-DDG reconstruction achieved the best ROC curve result (an SUVmax cut-off > 41.7 identifies a pNET with a specificity of 100% and a sensitivity of 75% (AUC 0.840)), (5) SUVmax of accessory spleens is linearily correlated with their volume.

Our results suggest a possible new indication for the use of [68Ga]Ga-DOTA-peptide PET/CT in clinical routine, confirming the ability of [68Ga]Ga-DOTATATE PET/CT to distinguish IPAS and pNET. Moreover, the impact of reconstruction algorithms is

one of the most relevant factors on the use of absolute quantitative methods for PET/CT. In our study, Bayesian penalized reconstruction data yielded slightly better results than OSEM distinguishing pNET from IPAS by SUVmax (p-value < 0.034 for BSREM vs. < 0.057 for OSEM) and for distinguishing pNET from accessory spleens by SUVmax (p-value < 0.014 for BSREM vs. < 0.024 for OSEM). This finding could be explained with the fact that the majority of well differentiated pNETs are characterized by significantly higher somatostatin receptor expression compared to the physiological uptake in splenic tissue (ectopic or not).

Besides the image reconstruction algorithm, PET image quality may also be affected by respiratory motion, leading to reduced quantitative accuracy and seemingly increased tumor/lesion volume. This problem affects particularly small lesions in the upper abdomen, such as accessory spleens, IPAS and pNET [95–98]. In our study, DDG increased the ability of PET parameters (SUVmax and SUVmean) to discriminate pNET from IPAS (SUVmax *p-value* < 0.033) and/or accessory spleens (SUVmax *p-value* < 0.002) both in BSREM and OSEM reconstructions. Furthermore, for all the lesions included in our study, DDG lead to a significant increase in SUVmax and SUVmean, both with BSREM and OSEM reconstructions (all p-values < 0.001), while a significant decrease in PET volume was only found with OSEM reconstruction (p-value < 0.001), in line with a recent study of Catalano et al. [99].

In conclusion, DDG-based motion correction is beneficial particularly for the assessment of small lesions that are subject to respiratory motion, also in the upper abdomen. $BSREM_{1000}$ leads to a significant increase of SUV parameters compared to OSEM, while DDG leads to a significant increase of SUV parameters and reduced PET volume compared to reconstructions without DDG.

CHAPTER 5

5. CLINICAL STUDIES

5.1. DIAGNOSTIC VALUE OF CONVENTIONAL PET PARAMETERS AND RADIOMIC FEATURES EXTRACTED FROM 18F-FDG-PET/CT FOR HISTOLOGIC SUBTYPE CLASSIFICATION AND CHARACTERIZATION OF LUNG NEUROENDOCRINE NEOPLASMS

5.1.1. Publication details

Thuillier P. et al. ***Diagnostic value of both conventional PET parameters and radiomic features extracted from ^{18}F-FDG PET/CT for histologic subtype classification and characterization of lung neuroendocrine neoplasms.*** Biomedicines. 2021 Mar 10;9(3):281. doi: 10.3390/biomedicines9030281. PMID: 33801987; PMCID: PMC8001140.

5.1.2. Introduction and aim

Lung neuroendocrine neoplasms (Lu-NENs) represent a group of rare neoplasms and are classified into four histological subtypes: lung neuroendocrine tumors (Lu-NETs), including typical (TC) and atypical carcinoid (AC), and lung neuroendocrine carcinomas (Lu-NECs), including large-cell neuroendocrine carcinomas (LCNECs) and small-cell neuroendocrine carcinomas (SCLCs) [100]. The prognosis of Lu-NENs is highly related to the histological subtypes. Lu-NECs are associated with a poor prognosis with a 5-year survival rate of 15% in LCNEC and 2% in SCLC, respectively, while patients affected by Lu-NETs hold a better prognosis. However, ACs are associated with poorer survival rates compared with TCs (44% and 87%, respectively) [101]. Thus, correct identification of the different Lu-NENs histological patterns is crucial in the decision-making process [40].

PET/CT is recommended to investigate Lu-NENs [48, 102]. [18F]F-FDG is widely used in Lu-NECs, but also in Lu-NETs [103, 104]; while [68Ga]Ga-DOTA-peptides PET/CT is suggested mainly in Lu-NETs (80% of tumor subtypes express somatostatin receptors) [51, 105]. Several studies assessed the diagnostic performance of dual [18F]F-FDG and [68Ga]Ga-DOTA-peptides-PET/CT in detecting lung carcinoid [106], suggesting their complementary role in discriminating TC from AC. Nevertheless, both exams are rarely performed before surgery.

Intratumoral tumor heterogeneity is one of the hallmarks of malignancy, aggressiveness, treatment response, and prognosis [21]. Indeed, PET radiopharmaceuticals present a different pattern of uptake within the tumor, however established conventional and volumetric PET parameters, such as SUV, MTV and TLG, do not allow for assessment of the heterogeneity of radiotracer uptake in a tumor. Recently, the extraction of RFs from [18F]F-FDG PET/CT was applied to characterize the histological pattern and prognosis of non-small cell lung cancers (NSCLCs) [107]. To the best of our knowledge, the radiomic approach has not yet been applied to characterize Lu-NENs.

In this study, we have hypothesized that both conventional PET parameters (i.e., SUV-based and volumetric parameters), and RFs extracted from [18F]F-FDG PET/CT might allow for more accurate definition of the histologic patterns and phenotypes of Lu-NENs. Therefore, the primary objective of this study was to investigate the diagnostic value of both conventional parameters and RFs to distinguish NETs from NECs and then, TC from AC. The secondary objective was to determine if these parameters are associated with pathological characteristics of tumor aggressiveness (such as mitotic index, presence of necrosis, and Ki-67 index), and TNM stage in Lu-NETs.

5.1.3. Material and Methods

Forty-four naïve-treatment patients on whom [18F]F-FDG PET/CT was performed for histologically confirmed Lu-NEN (n = 46) were retrospectively included. Inclusion criteria were: (a) Histologically proven Lu-NEN diagnosis (obtained by core biopsy in 10 samples or surgery in 36 samples) and classified according to the current WHO classification; (b) naïve-treatment patients who underwent [18F]F-FDG PET/CT; (c) patients who consented to participate in the study. Exclusion criteria were: (a) [18F]F-FDG PET/CT performed after surgery; (b) Cytological data available only. All clinical and histological data (age, gender, TNM) were collected.

All patients underwent [18F]F-FDG PET/CT on the same PET scanner (Philips Gemini DualsliceEXP scanner, PET AllegroTM system with Brilliance CT scanner, Philips MedicalSystems, Cleveland, OH). The median time interval between PET imaging and biopsy was 1.5 months (0–6 months), in accordance with the procedure guidelines for PET imaging.

Manual segmentation was performed by two operators allowing for extraction of four conventional PET parameters (SUVmax, SUVmean, MTV, and TLG) and 41 RFs, using LIFEx v. 6.0 (IMIV/CEA, Orsay, France). Manual segmentation for non-avid lesions was performed on the coupled CT images.

The continuous quantitative variables were compared by non-parametric tests (Mann–Whitney U or Kruskal–Wallis). For conventional PET parameters, we performed ROC analysis to assess the diagnostic performance of each of the conventional parameters to classify each lesion. The reproducibility of RFs between the two operators was assessed by ICC using a two-way mixed effects model. Among RFs with ICC > 0.9, the Mann–Whitney test was used to compare the RFs between each group of patients and select RFs able to discriminate the 2 groups of patients (Lu-NECs versus Lu-NETs and then TC versus AC). To reduce the potential redundancy among the RFs extracted in this study, the most useful predictive parameters were selected using the least absolute shrinkage and selection operator (LASSO) logistic regression model.
Then, a Pearson correlation analysis was performed between conventional PET parameters and RFs extracted from the LASSO regression. Then, a multivariate logistic regression analysis was performed to calculate a radiomic signature with the selected RFs. Finally, a ROC curve was used to illustrate the diagnostic performance of the model to predict the histological pattern.

5.1.4. Results

The main characteristics and clinical details of the 44 patients and 46 lesions histologically proven for Lu-NENs are represented in Table 3.

Table 3. Clinical and histological characteristics of the cohort.

Characteristics	Value	Characteristics	Value
Sex, n(%)		M-classification, n(%)	
Male	23 (52.3)	0	41 (89.1)
Female	21 (47.7)	1	5 (10.9)
Age (years) moy (DS)	62.8 (10.1)	Histological subtypes	
Lesion side, n(%)		TC	15 (32.6)
Right	29 (63)	AC	11 (23.9)
Left	17 (37)	TC or AC	1 (2.2)
Size (mm; moy(DS)	30.5 (16)	LCNEC	16 (34.8)
T-classification, n(%)		SCLC	3 (6.5)
1	17(37.0)	Mitosis/mm² (n=35)	
2	11 (23.9)	<2	15 (42.8)
3	8 (17.4)	2-10	10 (28.6)
4	0 (0)	10/mm²	10 (28.6)
X	10 (21.7)	Ki67% (n=45)	
N-classification, n(%)		≤5%	15 (33.3)
0	26 (56.5)	>5 and ≤20%	10 (22.2)
1	20 (43.5)	>20%	20 (44.4)

All conventional PET and volumetric parameters resulted higher in Lu-NECs compared to Lu-NETs ($p<0.001$). At ROC curve analysis, the best cut-off value to distinguish between Lu-NECs and Lu-NETs for SUVmax, SUVmean, MTV and TLG were 5.16 (Se=0.84, Sp=0.85 and Acc=0.85; AUC = 0.91), 3.69 (Se=0.79, Sp=0.96 and Acc=0.89; AUC = 0.91), 8.96 (Se=0.68, Sp=0.85 and Acc=0.78; AUC =0.8) and 38.67 (Se=0.79, Sp=0.89 and Acc=0.85; AUC =0.86), respectively (Figure 8).

Figure 8. *ROC curve analysis of the conventional and volumetric PET parameters (left) and Histo_Entropy_log10 (right)*

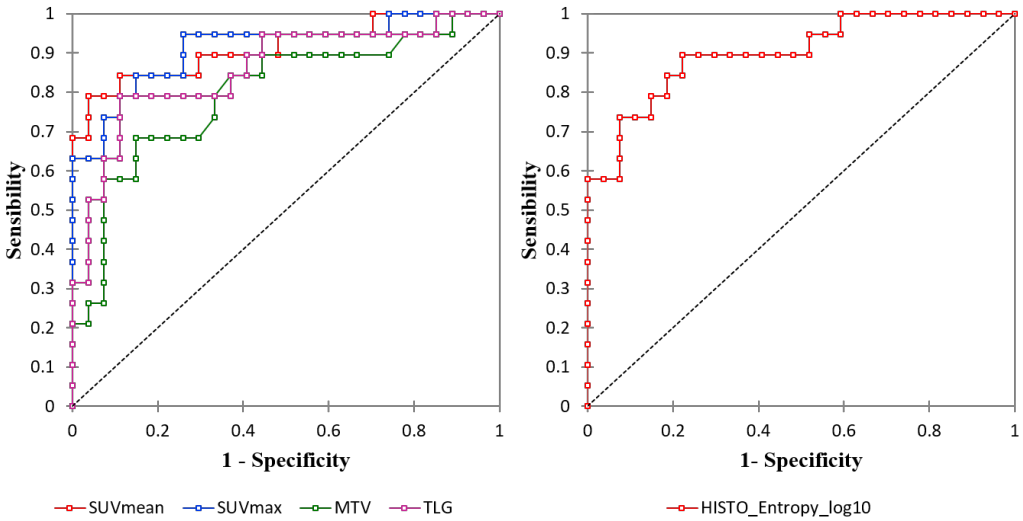

Regarding RFs, the inter-observer agreement between the two operators showed that 30/42 RFs (73.2%) were highly robust (6/6 histogram, 2/3 shape and 22/32 TFs;

ICC>0.9). Among the 30 RFs with ICC>0.9, 26 were significantly associated with histological subtypes (all p-values <0.05). Then, after LASSO implementation, HISTO_ Entropy_log10 was selected as the most predictive RF, with no significant advantages in adding more RFs to the model. At the ROC curve analysis, HISTO_ Entropy_log10 showed an AUC of 0.90, with a cut off value of 0.94 (Se=0.90, Sp=0.78 and Acc=0.83). Finally, HISTO_ Entropy_log10 was significantly positive correlated with SUVmax and SUVmean (r= 0.95 and 0.94 respectively). Combining both conventional parameters and HISTO_ Entropy_log10 in a logistic regression model, no significative advantages were found respect of the model with only SUVmean to predict the histological subtypes.

Finally, none of the conventional parameters were able to distinguish between TCs and ACs. Median SUVmax (3.62 versus 2.8; p=0.68) and SUVmean (2.37 versus 1.62; p=0.65) were not statistically different between TC and AC. None of the RFs was significantly different among TC and AC.

Regarding histological data, none of the PET parameters evaluated was associated with mitotic count or the presence of the necrosis (p>0.05). Stratifying TC and AC according to Ki-67 level, two TC presented Ki-67 >5%, while one AC had a Ki-67 ≤5% and two AC presented a Ki-67 >20. SUVmax and SUVmean showed a positive trend with Ki-67, without showing statistical significance (p=0.05 and 0.07 respectively). The two patients with AC and a Ki-67 index > 20% had much higher SUV values than TC and AC with Ki-67 <20%. Using Ki-67 as a continuous variable, there was an association between Ki-67 and SUVmax (R=0.52, p=0.007).

Regarding TNM status, SUVmax, MTV and TLG of the primary lesion were significantly associated with N+ status (p<0.05). At the ROC-curve analysis, SUVmax resulted the most accurate predictor of N+ status (AUC=0.78; p=0.004) with sensitivity=0.67, specificity=0.82 and accuracy=0.77, applying a cut-off of 4.11. In the Lu-NET subgroup, only 3 patients were M+ at the time of diagnosis and conventional and volumetric parameters showed a trend of correlation with M+ (p=0.08 for MTV and TLG).

5.1.5. Discussion and conclusion

Our study showed the good diagnostic performance of conventional parameters in the identification of Lu-NETs vs Lu-NECs allowing to discriminate these two groups of

patients, while our results did not suggest any potential additional value of the RFs. Regarding our subgroup analysis, considering Lu-NETs, we did not observe any difference between conventional PET parameters or RFs and TC and AC classification. On the other hand, higher value of conventional and volumetric PET parameters of the primary lesion were able to predict N+ status.

Regarding the diagnostic performance of RFs, we found that RFs do not provide additional information allowing us to discriminate Lu-NECs and Lu-NETs. Only HISTO_Entropy_log10 was selected by the LASSO regression, but it was highly correlated to conventional PET parameters. These results may be explained by the characteristics of our Lu-NENs population. First, even if several NETs might present high FDG-avidity, while several NECs hold low FDG-avidity, the broad difference in SUV values in NECs compared with NETs could lead to a broader difference in RF values between the two groups [108]. Moreover, the volume of Lu-NENs in our cohort was low (median value of MTV = 7.52 mL) and several studies reported that a radiomic approach does not provide additional information when the lesion metabolic volume is lower than 10 mL [109]. After LASSO implementation, HISTO_Entropy_log10 was also selected as the most predictive RF. At the ROC curve analysis, HISTO_Entropy_log10 showed a similar AUC of 0.91 but did not provide additional value comparing to the conventional PET parameters.

In the Lu-NET groups, we did not find any difference between TC and AC among all parameters when considering SUV parameters or other RFs. When related to the radiomic approach, these results could also be explained by the same reasons as for the Lu-NETs and Lu-NECs (i.e., no difference and a low SUV value in this case and a small size of lesions).

Nevertheless, a trend in the association between SUV values and the Ki-67 index, with special reference to the subgroup of cases with Ki-67 values exceeding 20%, has been found along with an association between SUV and N+ status. For this reason, conventional PET parameters might be applied to evaluate the tumor aggressiveness and to predict lymph node involvement in Lu-NETs. These preliminary results need to be validated in larger cohorts, even applying different methodologies, to assess the possible contribution of the radiomic analysis in PET imaging within this clinical setting.

5.2. PROGNOSTIC VALUE OF WHOLE-BODY PET VOLUMETRIC PARAMETERS EXTRACTED FROM 68GA-DOTATOC PET/CT IN WELL-DIFFERENTIATED NEUROENDOCRINE TUMORS

5.2.1. Publication details

Thuillier P. et al. ***Prognostic value of whole-body PET volumetric parameters extracted from 68Ga-DOTATOC-PET/CT in well-differentiated neuroendocrine tumors.*** J Nucl Med. 2022 Jul;63(7):1014-1020. doi: 10.2967/jnumed.121.262652. Epub 2021 Nov 5. PMID: 34740949.

5.2.2. Introduction and aim

NENs are a group of tumors of common embryological origin that can develop in multiple organs and secrete different hormones, leading to a variety of clinical presentations. They are most frequently observed in the gastroenteropancreatic tract (GEP–NENs) and the bronchopulmonary system. Although being relatively rare, their incidence has greatly increased in the last 30 years and estimated at approximately 5/100,0000/year [31].

PET/CT imaging with [68Ga]Ga-DOTA-SSTa is the mainstay for the "in vivo" evaluation of the SSTR on the NETs cells membranes [110, 111]. Overall, almost 90% of primary G1–G2 GEP-NETs present a PET-positive finding due to the high SSTR expression on the tumor cell surface [19]. In clinical practice [68Ga]Ga-DOTA-SSTa-PET/CT plays a major role in tumor characterization of NENs, in the assessment of disease extension and also to select properly the patient candidate for PRRT, becoming the gold standard in the diagnosis and management of WD-NETs [48, 112]. The prognostic value of [68Ga]Ga-DOTA-SSTa PET/CT imaging has been widely assessed in the literature, nevertheless mainly focusing on standardize uptake value (SUV) parameter [113, 114].

In the last few years, measures of metabolic tumor burden (MTB) from [18F]F-FDG-PET/CT images have been explored and showed a major prognostic value compared to semi quantitative parameters in several tumor models. MTB calculation is based on two PET parameters: MTV, which indicates the volume of metabolically active tumor, and

TLG, which is the product of SUVmean and MTV. More recently, two studies [115, 116] have interestingly demonstrated the prognostic utility of the somatostatin receptor tumor burden (SRTB) in patients with WD-NETs in predicting PFS, through the measurement of whole-body total lesion somatostatin receptor expression (TLSREwb) and somatostatin receptor expressing tumor volume (SRETVwb) from [68Ga]Ga-DOTATATE-PET/CT images.

Hence, the objective of this study is to evaluate the prognostic value of SRTB extracted from [68Ga]Ga-DOTATOC PET/CT in a large cohort of patients presenting WD-GEP-NETs and Lung-NETs.

5.2.3. Material and Methods

We retrospectively analyzed [68Ga]Ga-DOTATOC-PET/CT of 84 patients with histologically confirmed WD-NETs (51 G1, 30 G2 and 3 G3). Eligible patients matched all the following inclusion criteria: (1) histologically proven G1-G3 WD-NETs; (2) GEP or bronchopulmonary or unknown primary site; (3) [68Ga]Ga-DOTATOC-PET/CT performed in our department with at least 1 positive lesion; (4) follow-up > 6 months; (5) informed consent signed. Exclusion criteria were: (1) patient <18 years old; (2) incomplete histological data; (3) poorly differentiated neuroendocrine carcinoma; (4) concomitant metastatic neoplasia others than NET; (5) no evidence of disease at the time of [68Ga]Ga-DOTATOC-PET/CT; (6) refusal of data sharing according to ethical and privacy local law.

The following patient characteristics were retrieved from medical records: age, gender, genetic mutation if present, TNM stage at the time of PET imaging, tumor grade (G1, G2 or G3 according to Ki67% level (<3; 3-20; >20%, respectively), functional status, treatment history (surgery, radiotherapy, locoregional therapeutic procedures, prior systemic lines) and ongoing therapy after [68Ga]Ga-DOTATOC-PET/CT during the follow-up. Patients without history of treatment (excluding surgery) before PET were considered as “naive-treatment” patients.

All patients underwent PET/CT on an analog 3D PET scanner (Philips Gemini Dual-slice EXP scanner – PET Allegro^{TM} system with Brilliance CT scanner – Philips Medical Systems, Cleveland, OH), in accordance with the procedure guidelines for PET imaging [48].

For each PET/CT, all DOTATOC-avid lesions were segmented independently by two operators using a customized threshold based on the healthy liver SUVmax using LIFEx 6.0. For each lesion, SRETV and TLSRE (SRETV*SUVmean) were extracted. Then, we calculated the whole-body SRETV and TLSRE (SRETVwb and TLSREwb), defined as the sum of all SRETV and TLSRE, respectively. We classified each VOI according to its site including primary tumor, lymph node (ln), liver, bone and others (i.e. peritoneal, lung, and other rare metastatic sites). Then, we calculated the whole-body SRETV and TLSRE (SRETVwb and TLSREwb), defined as the sum of all lesions SRETV and TLSRE, respectively (Figure 9).

Figure 9. *Example of a 57-year-old female patient presenting a G3 well differentiated pancreatic NET. [68Ga]Ga-DOTATOC-PET/CT analysis (A: PET/CT fusion, B: PET imaging) showed high uptake in all lesions (highest SUVmax =104.4). SRTB analysis (C, D and E) found a SRETV and a TLSRE of 249ml and 4191g, respectively. Patient underwent PRRT and showed partial response according to RECIST 1.1 but finally progressive disease was reported 27 months after PET exam.*

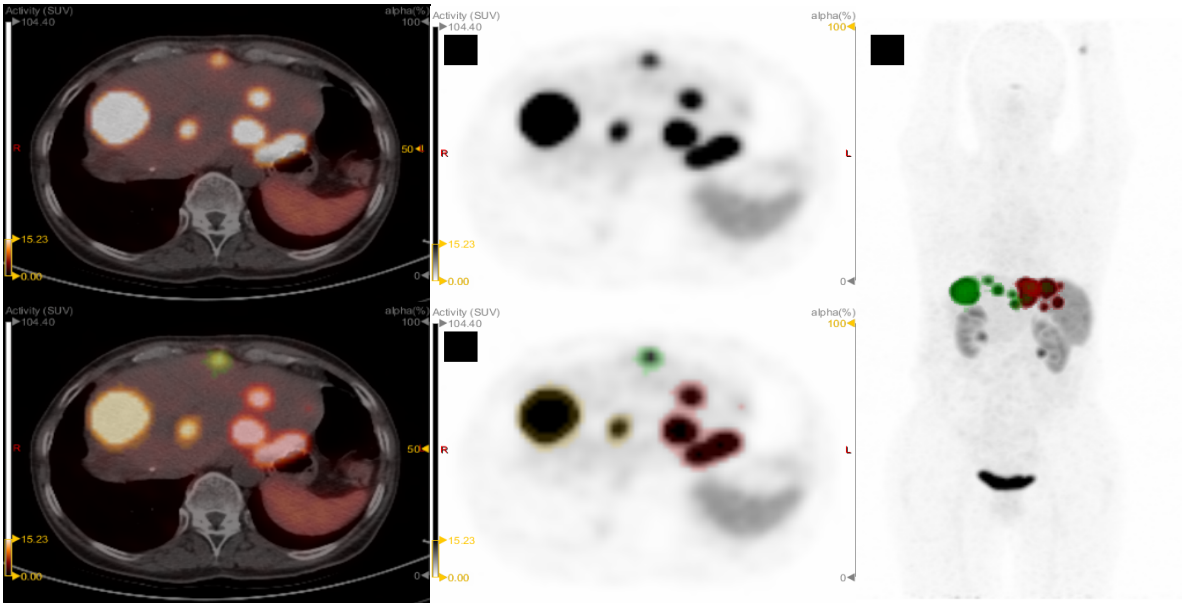

Time to progression (TTP) was defined as the combination of disease-free-survival (DFS) in patients undergoing curative surgery (n=10) and progression-free survival (PFS) for patients with unresecable disease (n=74). TTP and overall survival (OS) were studied using Kaplan-Meier analysis, log-rank test, and Cox's proportional hazard model.

5.2.4. Results

Among the 322 patients screened, 84 patients (38 male, 46 female; mean age 62.8±12 years) were included in the study. [68Ga]Ga-DOTATOC-PET/CT was performed for primary staging (n=34) or restaging (n=50). The most frequent primary tumor origin was the pancreas (39/84=46.4%). Fifty-four (64.3%) presented a metastatic disease at the time of PET/CT. Patients were classified as G1, G2 and G3 in 40.5, 55.9 and 3.6% of case, respectively. Forty-seven patients were considered treatment-naive before PET/CT.

In the whole cohort, a total of 442 lesions and subsequent VOI were segmented including primary (n=36; 8.1%), lymph node (n=72; 16.3%), liver (n=185; 41.9%), bone (n=114; 25.8%) and other categories of tumor sites (n=35; 7.9%), respectively. The median values of SUVmax, SRETV and TLSRE per-lesion were 9.7 [range,3.3-116.5], 4.0 ml [range,0.5-1980.3], and 24.8 g [range,1.8-21819.5], respectively. The median value of SRETVwb and TLSREwb were 32.4 ml [range,0-3078.7] and 338.3 g [range,0-22658.6], respectively.

For SRTB parameters, optimal cut-offs for predicting TTP were defined using the receiver operating characteristic (ROC) curve. For SRETVwb, the AUC was of 0.83 (best cut-off of 39.1ml with a sensibility, specificity, and accuracy of 0.86, 0.76 and 0.8, respectively. For TLSREwb, the AUC was of 0.79 with a best cut-off of 306.8g with a sensibility, specificity, and accuracy of 0.86, 0.74 and 0.79 respectively.

Using this threshold, Kaplan-Meier analysis revealed significant difference of TTP/OS for both SRETVwb and TLSREwb ($p<0.001$). Higher SRETVwb (≥39.1ml) and TLSREwb (>306.8g) were correlated with significantly shorter median TTP (TTP=12months; CI95% [10-23] vs not reached for both; $p<0.001$) and shorter median OS (OS not reached for both; $p<0.001$). SUVmax was not associated with TTP and OS ($p=0.08$ and $p=0.09$, respectively), as shown in Figure 10.

Figure 10. *Time to progression (left) and overall survival (right) in patients according to SUVmax (A, B), SRETVwb (C, D) and TLSREwb (E, F).*

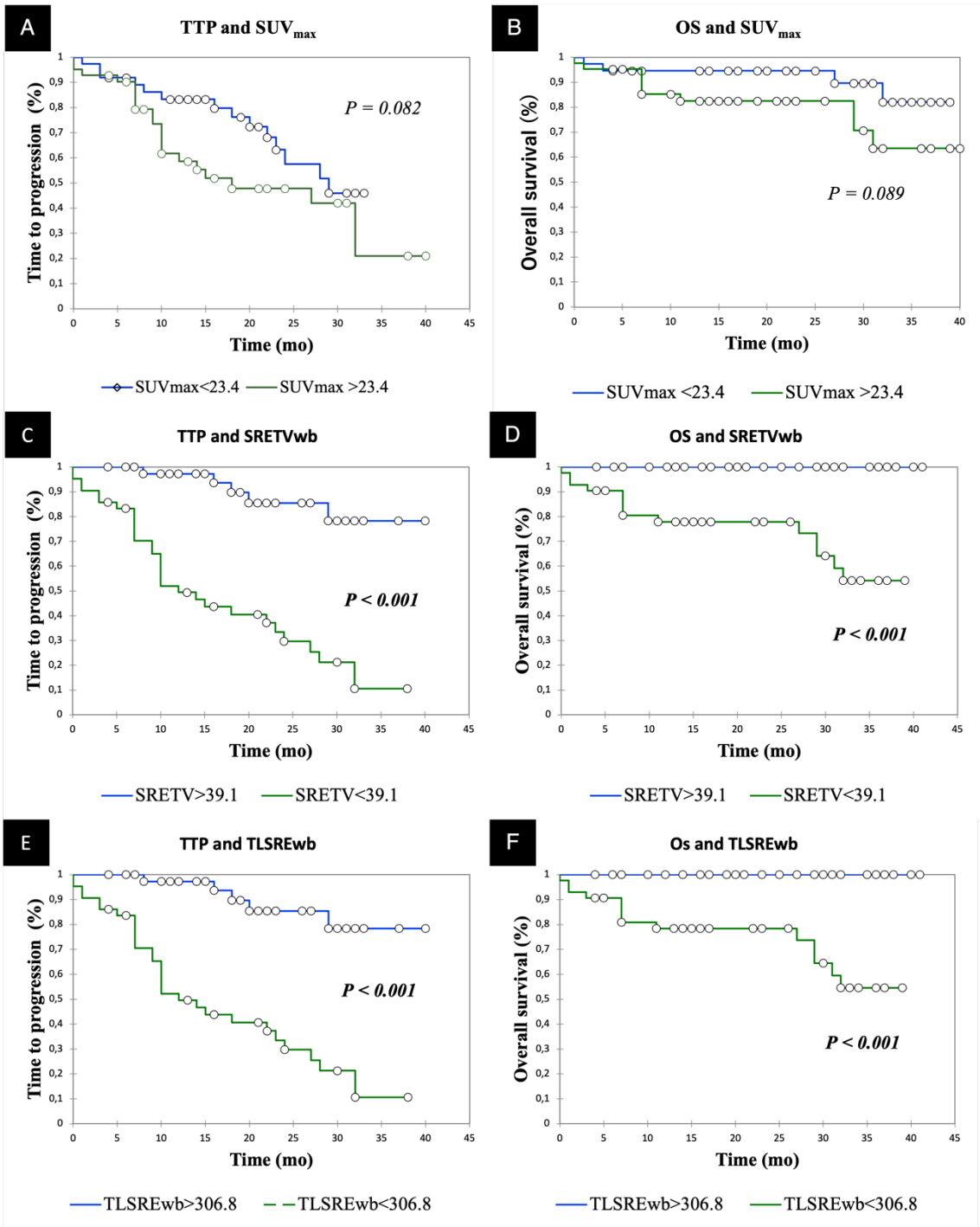

Thus, we performed a multivariate analysis and SRETVwb (>39.1ml) (HR=4.8 [1.6;14.5]; p=0.006) was the only independent predictor of TTP regardless of TNM stage, Ki67% level and treatment history (p=0.58, 0.85 and 0.39, respectively), as shown in Figure 11.

Figure 11. *Time to progression (left) and overall survival (right) in patients according to TNM stage (A, B) , grade (C, D) and treatment history (E, F).*

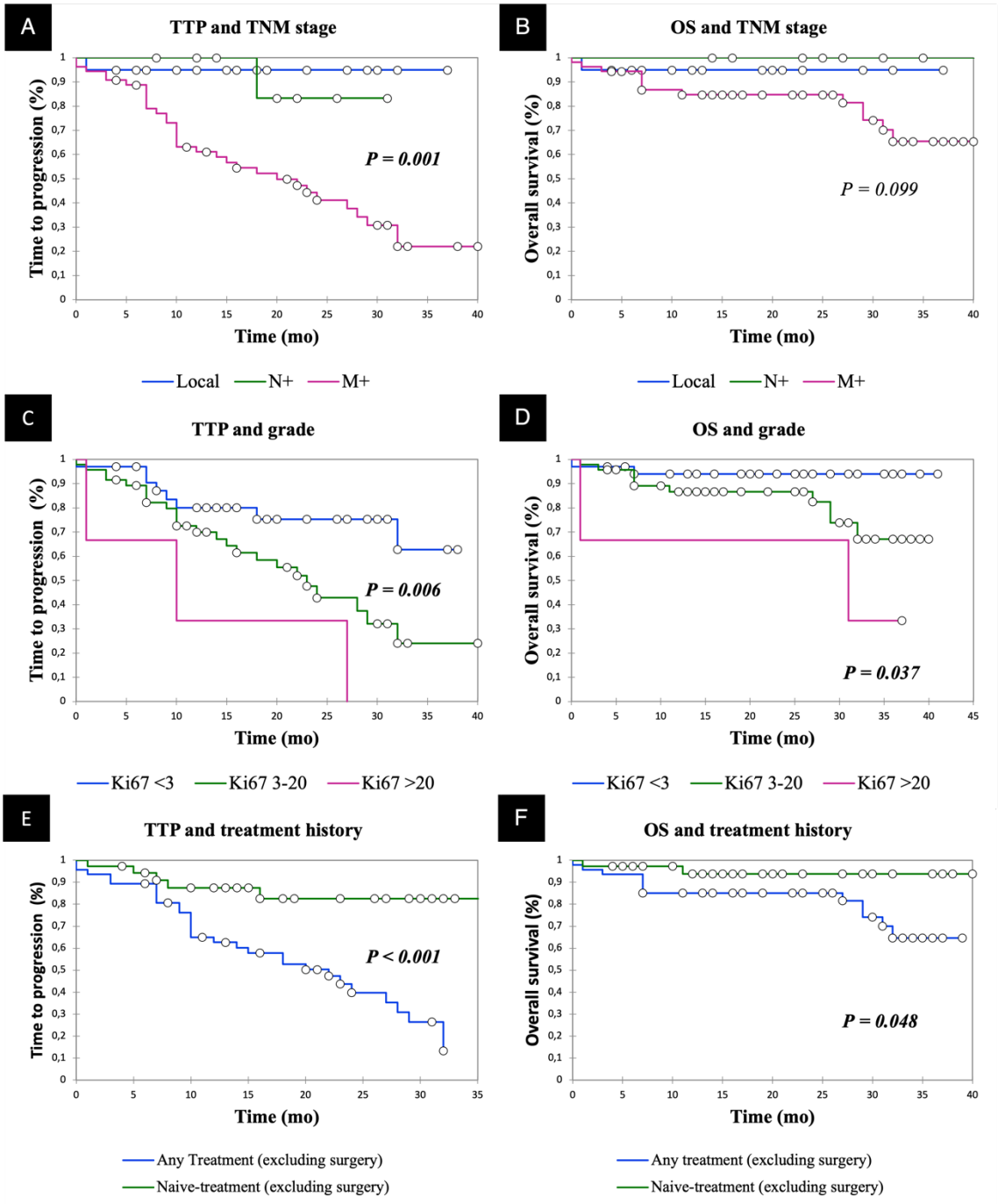

5.2.5. Discussion and conclusion

In our cohort SRETVwb and TLSREwb could predict TTP/OS in patients with WD-NETs and SRETVwb was the only independent prognostic parameter for TTP, regardless of histopathologic grade and TNM staging. SRETVwb extracted from

[68Ga]Ga-DOTATOC-PET/CT could have a prognostic utility in the clinical management of WD-NETs.

At univariate analysis we found that SRTB parameters, SRETVwb (≥39.1ml) and TLSREwb (≥306.8g) were significantly associated with TTP. Our results are consistent with the literature data. Regarding [68Ga]Ga-DOTATATE-PET/CT studies, in a prospective study including a large population of 184 patients with G1-G3 NETs, Tirosh et al. highlighted that SRETV≥7.0 mL and ≥35.8 mL were significantly associated with PFS and OS ($p<0.001$ both), respectively [115]. In another prospective study including only G1-G2 GEP-NETs, Toriihara et al. found that SRETVwb≥11.1ml and TLSREwb≥146.48g were associated with PFS [116].

In addition, Kim et al. [117] performed a retrospective study in 31 patients with unresectable or metastatic WD-GEP-NETs undergoing [68Ga]Ga-DOTATOC-PET/CT images before receiving lanreotide. In this study, lower tumor-to-liver ratio, SUVmax and higher SRETVwb (>58.9ml) were significantly associated with shorter PFS in univariate analysis, but only TLR (HR= 3.182, $p=0.021$) remained an independent factor for PFS in multivariate analysis. On the contrary, we showed that SUVmax was not associated with TTP, which is consistent with Tirosh et al. and Toriihara et al. studies [115, 116].

Furthermore, in our cohort SRETVwb was an independent prognosis parameter (HR=4.8 [1.6; 14.5]; $p=0.006$) in the multivariate analysis. Torihara et al. also highlighted that only SRETVwb was independently associated with PFS in survival analysis, but not TLSREwb. In our study, both parameters displayed a great degree of correlation ($R=0.916$), so we decided to only include SRETVwb in the multivariate analysis. Moreover, we showed that SRETVwb was an independent prognostic factor regardless of Ki67%, TNM stage and treatment lines before PET.

From a methodological point of view in our study, we chose a customized threshold based on liver SUVmax. To our knowledge, this is the second study in which such a segmentation method is used to assess the SRTB with [68Ga]Ga-DOTATOC-PET/CT in patients with WD-NETs [117]. This methodology presents the advantage to be fast, hence it could represent a useful tool to be used in clinical practice. Using this methodology, we found higher cut-off values of SRETVwb and TLSREwb in our study than those in studies assessing SRTB using [68Ga]Ga-DOTATATE. The literature showed that tumor uptake is higher and liver uptake is lower at [68Ga]Ga-DOTATOC versus [68Ga]Ga-DOTATATE, leading to higher tumor-to-liver ratio [118]. Hence, we

can assume that SRETVwb and TLSREwb might be lower using [68Ga]Ga-DOTATATE.

Moreover, assessing the reproducibility and robustness of SRTB calculation is important. In our study, we showed that the reproducibility between the two operators was excellent with ICC>0.9 for both SRETVwb and TLSREwb parameters. To our knowledge, there is no study assessing the reproducibility of SRTB parameters in [68Ga]Ga-DOTA-SSTa-PET/CT. Many studies showed that segmentation method can impact the reproducibility of MTVwb between operators in [18F]F-FDG-PET/CT imaging, especially threshold methods based on SUV>41% of SUVmax [73]. SRTB parameters in [68Ga]Ga-DOTA-SSTa-PET/CT might be more reproducible than MTVwb due to the higher signal-to-noise ratio.

Moreover, the evaluation of SRETVwb and TLSREwb changes (namely ΔSRETVwb and ΔTLSREwb) after initiation of systemic therapy may offer very promising perspectives, especially for patients treated with PRRT [119], and need to be assessed in futures studies. However, the initiation of SSA treatment or PRRT can modify liver uptake as previously reported [47] and impact the calculation of SRTB. Therefore, the systematic use of the pre-therapeutic liver SUVmax cut-off value could be a solution to follow the evolution of volumetric parameters (ΔSRETVwb and ΔTLSREwb) and should be evaluated [119].

In our cohort, whole-body volumetric [68Ga]Ga-DOTATOC-PET/CT parameters (SRETVwb and TLSREwb) were associated with TTP and OS. SRTB could have an additional value in comparison to conventional prognostic parameters and other standard PET parameters to predict patient's prognosis. SRTB approach could provide additional information to help clinicians in the treatment decision making and to guide follow-up of patients, thus supporting the implementation of these parameters in clinical practice for management of patients with WD-NETs. However, our findings need to be further confirmed in more homogeneous cohorts of patients and larger prospective studies are needed.

5.3. 68Ga-DOTATOC PET/CT-BASED RADIOMIC ANALYSIS AND PRRT OUTCOME: A PRELIMINARY EVALUATION BASED ON AN EXPLORATORY RADIOMIC ANALYSIS ON TWO PATIENTS

5.3.1. Publication details

Liberini V. et al. ***^{68}Ga-DOTATOC PET/CT based radiomic analysis and PRRT outcome: a preliminary evaluation based on an exploratory radiomic analysis on two patients.*** Front Med (Lausanne). 2021 Jan 26;7:601853. doi: 10.3389/fmed.2020.601853.

5.3.2. Introduction and aim

PRRT has proven to be an effective treatment for metastatic GEP-NET [120]. [177Lu]Lu-DOTATATE has been approved by European Medicine Agency (EMA) in 2017 for treating inoperable or metastatic GEP-NET with progressive disease. To evaluate the response to PRRT, the Delphic consensus assessment for GEP-NET [121] considers suboptimal both the Response Evaluation Criteria in Solid Tumors 1.1 (RECIST 1.1) and PET parameters derived by functional imaging (SUV), considering the high variability in somatostatin receptor expression and different histological patterns related to disease heterogeneity. [68Ga]Ga-DOTA-SSTR PET/CT allows to evaluate the in vivo expression of the SSTR in NET, and is considered a gatekeeper to select the proper candidate to PRRT [20, 48, 122]. Thus, the identification of new and reliable semi-quantitative and quantitative imaging parameters might be crucial to better select eligible patients and to assess the response to PRRT. Radiomic is a new innovative bioinformatic approach to the image's analysis [1, 57, 123].

We hypothesize that advanced semi-quantitative PET parameters and radiomic analysis applied to [68Ga]Ga-DOTATOC PET/CT might identify correctly tumoral heterogeneity and new parameters able to predict response to PRRT in NET patients. In this preliminary study, we retrospectively explored this hypothesis on two NET patients with liver metastases and different outcome from PRRT therapy.

5.3.3. Material and Methods

We retrospectively performed semiquantitative and radiomic analysis in [68Ga]Ga-DOTATOC PET/CT image of two patients both presenting with NET liver metastases, selected from a retrospective study approved by Local Ethical Committee (IRB protocol: CS2/477) of AOU Città della Salute e della Scienza. Both patients were treated with PRRT in a clinical trial (EUDRACT 2015-005546-63) approved by the Ethical Committee of "Area Vasta Emilia Nord" (AVEN) of the "Azienda USL-IRCCS of Reggio Emilia, Italy". Patients' information and dosimetry schedule for both patients are summarized in Figure 12.

Figure 12. *[68Ga]Ga-DOTATOC PET/CT (pre- (a) and post-therapy (b)) and [18F]F-FDG PET/CT (pre-therapy (c)) of Patient A; [68Ga]Ga-DOTATOC PET/CT (pre- (d) and post-therapy (e)) and [18F]F-FDG PET/CT (pre-therapy (f)) of Patient B; and patient history timeline of both Patient A and B. The pre- and post-therapy maximum intensity projection (MIP) of [68Ga]Ga-DOTATOC PET/CT of Patient B shows a homogeneous decreasing in size and somatostatin receptor expression of all the liver lesions. Patient A received 1 cycle of [90Y]Y-DOTATOC (1.7 GBq) followed by 6 cycles of [177Lu]Lu-DOTATOC (total cumulated activity 26.13 GBq) with a median estimated absorbed dose of 104.5 Gy (range:63-134). Patients B received 3 cycles of [90Y]Y-DOTATOC (cumulated activity of 3 GBq) followed by 3 cycles of [177Lu]Lu-DOTATOC (cumulated activity of 14.30 GBq) with a median estimated absorbed dose of 104 Gy (range:94-122).*

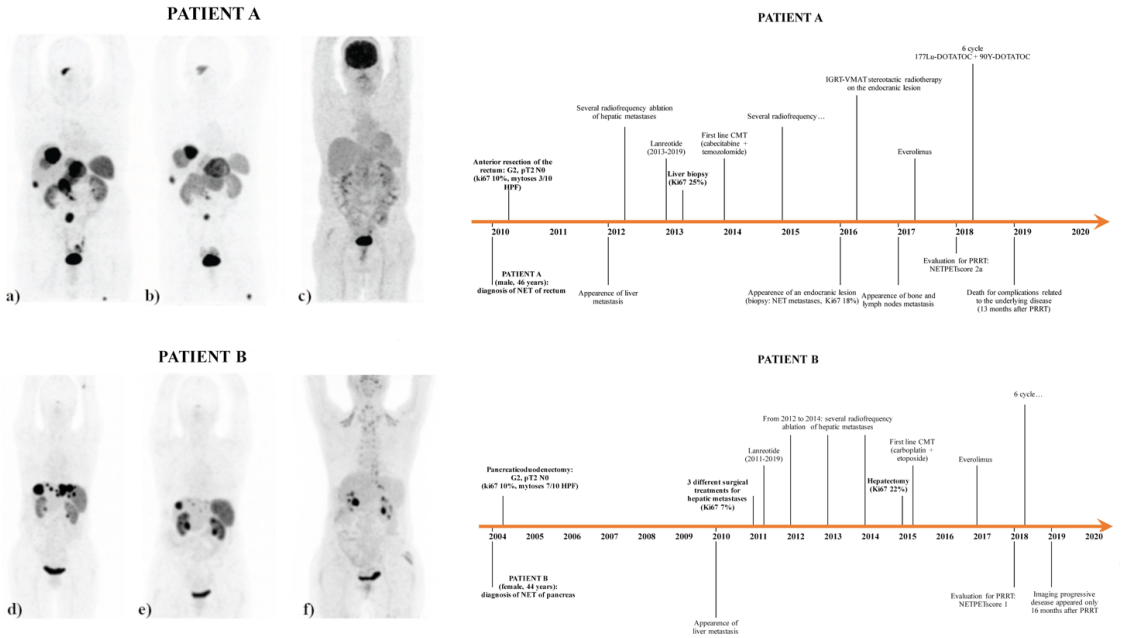

Patient-A had metastatic disease by G3 NET of rectum and Patient-B by G3 NET of the pancreas. Both patients underwent surgery as primary therapy (pT2N0, Ki67 10%) plus somatostatin analogue (lanreotide) administration. Both patients developed liver metastases, treated with multiple radiofrequency ablations, subsequently with chemotherapy after progression and later with everolimus. Liver biopsy revealed similar Ki67% patterns (Ki67 25% for patient A and 22% for patient B). PRRT was considered as third line of treatment according to clinical trials inclusions criteria. [18F]F-FDG PET/CT showed faint uptake in the lesions with NET- PET score of 2a for Patient A and score 1 for Patient B [20], while the [68Ga]Ga-DOTATOC PET/CT scan showed visually high uptake in all lesions. Six cycle of PRRT were administrated, completed in November 2018 for Patient A and in July 2018 for Patient B.

Patient A and patient B, according to the trial design, underwent several [177Lu]Lu- and [90Y]Y-DOTATATOC administrations. Tumor absorbed doses were calculated following the procedure described by Finocchiaro et al [124]. Similar biodistribution and kinetics for peptides labelled with [177Lu]Lu and [90Y]Y was generally assumed [125], therefore the results obtained with [177Lu]Lu were extrapolated to [90Y]Y, simply substituting physical decay constant λ and S factor, as reported in the paper of Guerrierio et al. [126]. Patient A received only one cycle of [90Y]Y due to radioisotope supply problems. However, the range of tumor absorbed doses for patient A (63-134 Gy) was comparable to the tumor absorbed doses for patient B (91-122 Gy). Patient A died for cancer-related disease 13 months after treatment, while Patient B at the end of follow up was alive with persistent disease and presented disease progression 16 months after PRRT (overall survival was 26 months after PRRT).

Patients underwent [68Ga]Ga-DOTATOC PET/CT before and after the end of PRRT treatment. According to RECIST 1.1, Patient-A was considered as non-responder to PRRT, while Patient-B achieved very good partial response.

Radiomic analysis was performed by manually contouring VOI by one operator and a total of 38 features were extracted using the software LIFEx v.5.10 (IMIV/CEA, Orsay, France) [71]. In both pre- and post-PRRT PET scans, two volumetric parameters, [127], were also evaluated: the somatostatin receptor expressing tumor volume (SRETV), representing the volume of the isocountouring derived volumes of interest (VOI) based

on percentage of 50% threshold of lesion maximum SUV (VOI_{50}) [73], and the total lesion somatostatin receptor expression (TLSRE), calculated by multiplying the SRETV of each lesion with its corresponding SUVmean value. Moreover, the whole-body SRETV ($SRETV_{wb\text{-}50}$) and TLSRE ($TLSRE_{wb\text{-}50}$) of each patient were also calculated in both pre- and after-PRRT scan.

The Mann-Whitney test was used to compare the RFs extracted by the VOI of the liver metastasis lesion of the two patients on the pre-PRRT scan. To evaluate the independence of the features, the correlation of each RF with all the others was studied using regression analysis, generating a Pearson correlation matrix. Two RFs were considered strongly correlated in case of correlation coefficient greater than 0.8 or lower than -0.8. Only RFs which were not strongly correlated with SUVmax and lesion PET volume were analyzed due to their already established role on PRRT as predictive and prognostic biomarkers [114–116, 128–130]**.** Finally, the Principal Component Analysis (PCA) was used to obtain an alternative visualization of correlated and independent RFs and to investigate the possibility of creating a smaller set of maximally uncorrelated RFs (principal components) able to explain the majority of total variation in the data set**.**

5.3.4. Results

The response to therapy was more heterogenous in Patient A with some liver and abdominal lesions increased in size, and others showing a partial response. A total of 8 liver metastases in Patient A and 10 liver metastases in Patient B were considered for inter-patient RFs comparison. Moreover, in patient A, 2 further lymph-nodes and 2 bone lesions were analyzed.

Comparing liver metastases of pre-PRRT scan, twenty-eight RFs resulted significantly different among patients A and B at the Mann-Whitney test. Figure 13 shows the results of the Pearson correlation to identify the non-redundant features. Moreover, the PCA of the first two principal components (PCs), performed in 26 features, explained the 83.8% of total variance (Figure 13).

Figure 13. *Pearson correlation matrix heat map, considering only the 26 radiomic features resulted significant at the Mann-Whitney test (a). This graphic displays the absolute value of the correlation coefficient between each pair of radiomic features, ranging from + 1 (positive linear correlation, in red)*

to – 1 (negative linear correlation, in green). The correlation coefficient of 0 is represented in yellow and identified radiomic features that are not correlate. Graphic representation of the features correlation plots resulted from the Principal Component Analysis (PCA), performed on the 26 radiomic features resulted significant at the Mann-Whitney test (b). It shows the relationships between features: positively correlated features are grouped together, and negatively correlated features are positioned on opposed quadrants. The distance between features and the origin measures the quality of the features on the factor map and features that are away from the origin are well represented on the factor map. The SUV-related RFs are visible in the lower left quadrant and the volume-related RFs in the lower right. The scree plot of the percentages of variation that each principal component (PC) account for shows that PC1 and PC2 identified 83.8% of the percentages of variation (c).

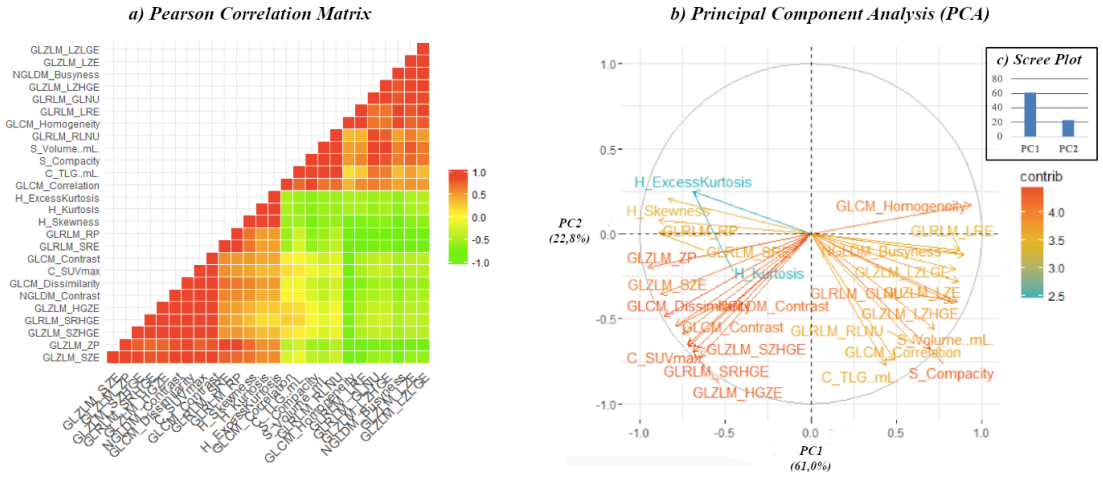

The relative correlation of these RFs with SUVmax and volume are shown in Figure 14. Seven second-order features resulted not correlated with both SUVmax and volume and statistically different among patient A and B (Figure 14).

Regarding the two volumetric parameters, baseline $TLSRE_{wb\text{-}50}$ and $SRETV_{wb\text{-}50}$ were 5524.7 mL and 493.8 mL for Patient A and 1780.2 mL and 35.2 mL for patient B, respectively. At the post PRRT PET scan, both $TLSRE_{wb\text{-}50}$ and $SRETV_{wb\text{-}50}$ increased in patient A ($TLSRE_{wb\text{-}50}$ 9291.6 mL ($\Delta TLSRE_{wb\text{-}50}$ +68,2%) and $SRETV_{wb\text{-}50}$ 991.0 mL ($\Delta SRETV_{wb\text{-}50}$ +100,7%) and decreased in patient B ($TLSRE_{wb\text{-}50}$ 202.4 mL ($\Delta TLSRE_{wb\text{-}50}$ -88,6%) and $SRETV_{wb\text{-}50}$ 23.2 mL ($\Delta SRETV_{wb\text{-}50}$ -51,7%).

Figure 14. *(a) Pearson correlation coefficients between radiomic features and SUVmax and and volume (mL), respectively; (b) the boxplot of the second-order features not correlated with both SUVmax and volume in non-responder and responder.*

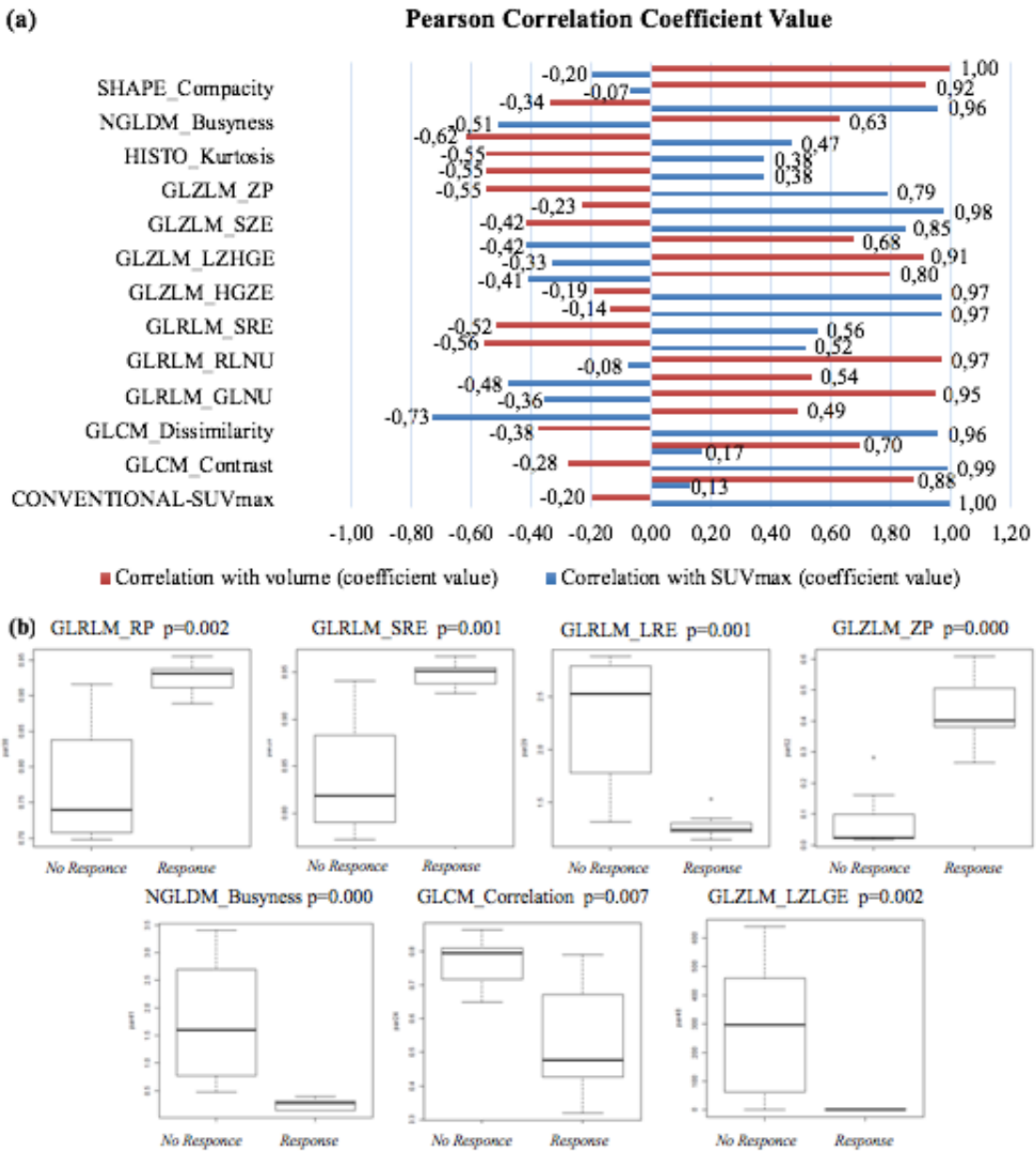

5.3.5. Discussion and conclusion

There is a lack of validated quantitative parameters able to predict the response to PRRT in PET imaging, while radiomic approach is emerging as a very promising analysis to study tumoral heterogeneity and should be evaluated for its prognostic and predictive role. Werner et al. [131] analyzed RFs on [68Ga]Ga-DOTA-peptides in 31 patients with G1/G2 pancreatic NET. They found that “TF entropy” (corresponding to GLCLM-entropy) was associated with overall survival (cutoff = 6.7, p= 0.02) and increasing entropy might be a predictor of a longer survival. In our study the median value of GLCLM-entropy was > 6.7 for Patient-B and < 6.7 for Patient-A, even if not

reached statistical significance. The Mann-Whitney test demonstrated a significant difference among the two patients in others twenty-eight RFs on baseline PET/CT, which could be related to differences in lesions behavior. Seven second-order RFs have been identified as poorly associated with SUVmax and PET volume parameters and might be considered as potential predictors of therapy response.

In the post-PRRT PET/CT scan of patient B, the value of GLRLM-LRE and NGLDM-Busyness increased in liver responder lesions ("*liver 6, 7 and 8*" with a decrease of SUVmax and PET volume). On the contrary, GLCM correlation, GLRLM-SRE, GLRLM-RP and GLZLM-ZP decreased in the same lesions (data are showed in Table 1). Furthermore, in a lesion ("*lymph node 1*") of Patient A, characterized by SUVmax decreasing, these RFs showed similar changes with the only exception of GLCM correlation, despite PET volume increasing (stable disease for RECIST 1.1). These changes have been not observed in non-responder lesions in both patients; in particular GLRLM SRE, GLRLM LRE, GLRLM RP, GLZLM ZP and NGLDM busyness did not change consistently, resulting almost stable. Finally, GLZLM-LZLGE changes seems less related to the PRRT response, as increasing and decreasing changes has been observed in both responder and non-responder lesions randomly. Furthermore, RF changes seem to be independent from the Gy delivered to the lesions.

While far from definitive, these data allow to hypothesize a potential role both for RFs in pre-therapy scan and ΔRFs changes as predictor of therapy response, in combination with predictive parameters (including standard semiquantitative PET parameters and dosimetry), if confirmed trough a prospective study [20, 121, 123, 127].

Regarding the two volumetric conventional PET parameters, the few data at present available in literature showed a significant correlation between the $SRETV_{wb\text{-}50}$ and disease progression. Tirosh et al. [115] observed an association between "[68Ga]Ga-DOTATATE TV" (corresponding to $SRETV_{wb\text{-}50}$) > 7.0 mL with higher risk for disease progression and "[68Ga]Ga-DOTATATE TV" > 35.8 ml was associated with higher disease-specific mortality. Toriihara et al. [116] showed an association between "[68Ga]Ga-DOTATATE ∑SRETV" (corresponding to $SRETV_{wb\text{-}50}$) > 11.29 mL and shorter progression free survival. In our study, the responder patient presented an $SRETV_{wb\text{-}50}$ of 35.2 mL at baseline PET/CT, just below the cut-off value associated with higher disease-specific mortality in Tirosh study. $SRETV_{wb\text{-}50}$ in non-responder patient was of far above the cut-off reported above (493.8 mL). These data are consistent with the different response and outcome to PRRT of our patients, namely

considering the higher tumor burden and the relative lower uptake of the lesions in the non-responder vs. the responder patient (mean TSR 2.35 for Patient A versus 8.80 for Patient B; mean TLR 7.44 for Patient A versus 24.81 for Patient B). Overall survival after PRRT was 26 months (at last follow-up patient was alive with disease) in patient-B, while was 13 months in Patient-A (died with disease). On the other hand, the median absorbed dose received by the two patients was very similar; therefore, in these two cases dosimetry cannot explain completely the different response, as well as negative pre-PRRT [18F]F-FDG PET/CT (Figure 1). Furthermore, the opposite trend of $TLSRE_{wb\text{-}50}$ and $SRETV_{wb\text{-}50}$ (increase in Patients-A, decrease in Patient-B) in accordance with RECIST 1.1 might suggest a role for these parameters also in PRRT response. To our knowledge, there are no studies, designed to evaluate the role of $\Delta SRETV_{wb}$ and $\Delta TLSRE_{wb}$ on therapy response.

Despite evaluated on only two patients, this preliminary analysis suggests the use of RFs and TLSREwb-50, SRETVwb-50 as parameters to evaluate response to PRRT in NET patients. Moreover, pre-therapy RFs and RFs changes observed from pre- to post-therapy scan might help to predict and to assess response to PRRT, leading to an optimization in the management of NET patients. These exploratory results need to be confirmed by future studies, enrolling a larger and more homogenous population.

5.4. [68Ga]DOTATOC PET/CT RADIOMICS TO PREDICT THE RESPONSE IN GEP-NETS UNDERGOING [177Lu]DOTATOC PRRT: THE "THERAGNOMICS" CONCEPT

5.4.1. Publication details

Laudicella R. et al. ***[68GA]DOTATOC PET/CT machine-learning applicationsin the prediction of response in GEP-NETS undergoing[177LU]DOTATOC PRRT: the ''THERAGNOMICS'' concept***. 15th National Congress of the Italian Association of Nuclear Medicine and Molecular Imaging (AIMN). Clin Transl Imaging 10 (Suppl 1), 1–111 (2022). https://doi.org/10.1007/s40336-022-00492-x

5.4.2. Introduction and aim

PRRT represents an effective treatment for metastatic or inoperable NET, recently approved in Europe, USA, and Canada for GEP forms [52, 53, 132]. PRRT is included in the theragnostics scenario, enabling, through a unique radiopharmaceutical administration for multiple cycles, a molecularly targeted therapeutic procedure (i.e., beta minus emission of [177Lu]Lu) and biodistribution imaging (i.e., gamma emission of [177Lu]Lu). However, although PRRT is effective in the majority of cases, approximately 15–30% of patients will progress during PRRT and can benefit from timely adjustments, therapy combinations, rapid sequencing, or alternatives.

Furthermore, the Delphic consensus for GEP-NET response to therapy assessment defined both the RECIST 1.1 criteria and PET parameters as suboptimal due to the high variability in SSTR expression, the different histological patterns related to disease heterogeneity, heterogeneous responses, and lack of standardized criteria for molecular imaging [121]. In addition, biochemical assessment of tumor markers, such as Chromogranin A is also suboptimal. However, promising and innovative approaches, such as NET TEST, have been proposed but they are highly costly and not easily accessible [133, 134]. Therefore, the identification of new and reliable quantitative imaging parameters, such as radiomics, could be crucial to better address eligible candidates and to assess the response to PRRT, early selecting the best therapeutic opportunity, avoiding high-costly treatments and related toxicities.

A few studies already assessed the potential application of machine-learning (ML) in GEP-NET to predict response to PRRT. However, such studies referred to very limited populations [119, 135], heterogeneous cohorts, or considered only predefined features [131, 135, 136]. Therefore, we aimed to develop a more robust radiomics ("radiOMICS") predictive model of response analyzing [68Ga]Ga-DOTATOC PET/CT images before and after complete [177Lu]Lu-DOTATOC PRRT ("THERAGNOstics") in well-differentiated, progressive, metastatic GEP NET, namely "Theragnomics" that can be applied in a clinical decision support system (CDSS).

5.4.3. Material and Methods

In this retrospective study, we included all consecutive well-differentiated GEP-NET patients who, between 1 April 2013 and 30 November 2019, underwent a baseline [68Ga]Ga-DOTATOC PET/CT within 2 months before beginning the PRRT with [177Lu]Lu-DOTATOC, and a follow-up [68Ga]Ga-DOTATOC PET/CT available within 9 months after the last PRRT cycle. CgA was also assessed before each PRRT cycle and at the end of the treatment. Clinical, laboratory, and [68Ga]Ga-DOTATOC PET/CT follow-up data were collected for a period of at least 3 months after the last cycle. Patients were not eligible if: (a) they were under 18 years of age; (b) lack of follow-up/baseline imaging and clinical data; (c) patients with other concomitant oncological pathology. In Figure 15, we describe the study workflow.

Figure 15. *Study workflow.*

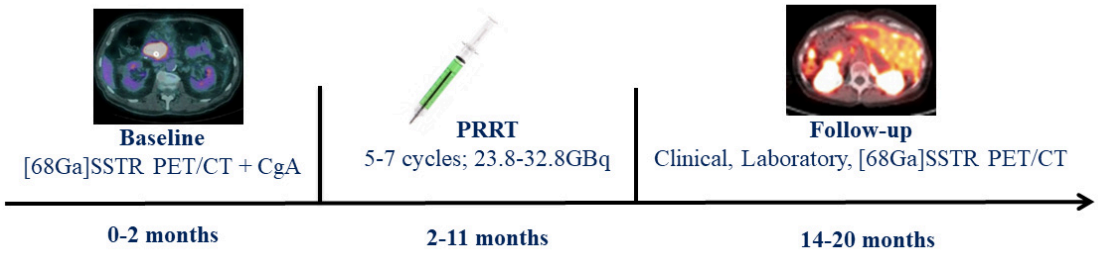

In comparison with baseline, [68Ga]Ga-DOTATOC PET/CT follow-up after PRRT determined the status of response to therapy for each lesion in terms of disease progression (PD, increase in lesion size/SUVmax of at least 25%) vs. stability (SD, increase-reduction in lesion size/SUVmax < 25%), reduction (PR, decrease in lesion size/SUVmax of at least 25%), or disappearance (CR). All PET/CT images were

qualitatively analyzed with a dedicated workstation and were interpreted by two nuclear medicine physicians. All patients completed full PRRT (at least 5 cycles) that began within 2 months after baseline [68Ga]Ga-DOTATOC PET/CT. Therapy response was routinely assessed on an individual lesion level.

Through LifeX, we extracted 65 PET features for each lesion detected at baseline [68Ga]Ga-DOTATOC PET/CT. In addition, five clinical features were also considered: grading (G1-G2-G3), number of PRRT cycles, PRRT cumulative activity, pre- and post-PRRT CgA values. All the features (imaging and clinical) were correlated with the response data. Specifically, due to the redundancy, heterogeneity, and uncertainty of the information represented by the radiomics features, we used an innovative mixed descriptive-inferential sequential approach for the feature selection and reduction process [62]. For each feature, the point biserial correlation (pbc) index between features and the dichotomic outcome (PD vs. SD, PR, CR) was calculated, sorting the features in pbc descending order. Then, a cycle started to add one column at a time, performing a logistic regression analysis by comparing the p-value of each iteration and stopping in the case of a growing p-value. Accordingly, the features with valuable association with the outcome were identified and assessed (singularly and in combination) for response to PRRT prediction. Finally, the discriminant analysis (DA) was used for implementing the classification model using the k-fold strategy to split data into training and validation sets. In this way, the PET studies were divided into k-folds. One of the folds was used as the validation set and the remaining folds were combined in the training set. This process was repeated k-times using each fold as the validation set and the other remaining sets as the training set. In our study, k = 5 was empirically determined by trial-and-error strategy (k range: 5–15, step size of 5).

For the most significant features, we also assessed the percentage difference value before (T0) and after PRRT (T1) in terms of delta radiomics, translating the pre-PRRT [68Ga]Ga-DOTA-peptide PET/CT ROI in the same lesion area of the follow-up performed within nine months after PRRT. The delta radiomics was then calculated using the following formula:

$$\Delta = 100 * (\text{Feature T1} - \text{Feature T0})/\text{Feature T0}$$

Finally, we performed a per-district analysis (lymph node, liver, and bone) evaluating all the pre-PRRT PET/CT features in response to PRRT prediction.

The differences of the most significant features and delta radiomics between responders and non-responders were compared using a non-parametric Mann–Whitney U test. The ability of the most significant radiomics features to predict the response to PRRT was assessed with ROC analysis. The AUC was reported.

In addition, a site-dependent sub-analysis was performed for the most represented districts of our cohort (lymph node, liver, and bone), evaluating both the pre-PRRT PET/CT parameters, radiomics features, and the delta radiomics for the most significant parameters in the response to PRRT prediction.

5.4.4. Results

A total of 38 GEP NET patients with a median age of 58 years (range 35–79; mean 59; 15 out of 38 female) were retrospectively included and underwent a baseline [68Ga]Ga-DOTATOC PET/CT (mean activity 151.1±55.5 MBq, range 93–330 MBq; median 120.5 MBq) a mean of 1.4±0.7 months (0–2) before complete PRRT with a median cumulative dose of 29.0 GBq (23.9–32.8 GBq), followed by [68Ga]Ga-DOTATOC PET/CT (mean activity 165±62.6 MBq, range 93–330 MBq; median 128.5 MBq) a mean of 8.7±1.1 months (3–9) after the last PRRT cycle. The primary sites originated from the pancreas in 17 out of 38, ileum 14 out of 38, colon three out of 38, stomach two out of 38, and jejunum two out of 38. Grading was distributed as follows: 9/38 G1, 27/38 G2, 2/38 G3. [177Lu]Lu-DOTATOC PRRT was performed a median of five cycles (5–7; total 200; mean 5.3±0.5) with a mean administered activity of 29±1.5 GBq. Baseline CgA was 277 ng/mL (17–1315; mean 394.7±376.1 ng/mL), while follow-up CgA was 125.5 ng/mL (16–1630; mean 380.5±426 ng/mL).

At baseline [68Ga]Ga-DOTATOC PET/CT, we obtained 324 SSTR-positive lesions with at least 16 voxels. Based on their location, lesions were divided as follows: 169 in 324 liver, 91 in 324 lymph nodal, 42 in 324 bone lesions, and 22 in 324 parenchymal (different than liver). At the qualitative assessment of follow-up [68Ga]Ga-DOTATOC PET/CT, 133 in 324 lesions were classified as PD and 191 lesions as responsive to therapy (SD + PR + CR).

Through LifeX software, 65 features were extracted from baseline [68Ga]Ga-DOTATOC PET/CT for each lesion. From the reduction and selection process, the combination of three features, two from PET (HISTO_Skewness; HISTO_Kurtosis) and one clinical (Grading) proved able to predict each lesion's response to PRRT in terms of

progression vs. positive results, regardless of their nature (parenchymal, lymph nodes, bone lesions), with an AUC ROC, sensitivity, and specificity of 0.744, 66.4%, and 70.3%, respectively. However, the best predictive result was obtained for HISTO_Skewness, with an optimal cut-off at 2.45 reaching an AUC ROC, sensitivity, and specificity of 0.745, 80.6%, and 67.2%, respectively. Moreover, HISTO_Kurtosis, with an optimal cut-off at 6.94 reached an AUC ROC, sensitivity, and specificity of 0.722, 61.2%, and 75.9%, respectively. Differently, the SUVmax was not significant ($p = 0.49$) to predict the response to PRRT in terms of progression vs. objective benefit or response (AUC ROC 0.523, sensitivity 36.7%, specificity 63.3%), as shown in Figure 16.

Figure 16. *ROC curve analysis for HISTO_Skewness, HISTO_Kurtosis, Grading, their combination (Combined Model) and SUVmax in the prediction of response to PRRT (early FU status) in terms of PD vs. positive results (SD, PR, CR).*

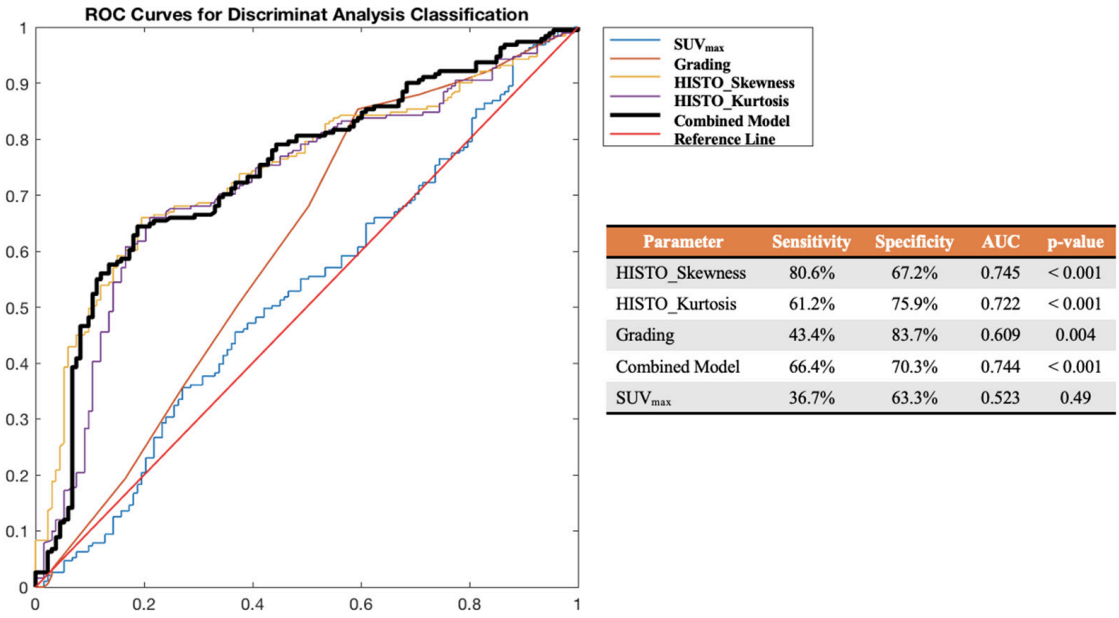

Parameter	Sensitivity	Specificity	AUC	p-value
HISTO_Skewness	80.6%	67.2%	0.745	< 0.001
HISTO_Kurtosis	61.2%	75.9%	0.722	< 0.001
Grading	43.4%	83.7%	0.609	0.004
Combined Model	66.4%	70.3%	0.744	< 0.001
SUV_{max}	36.7%	63.3%	0.523	0.49

Furthermore, HISTO_Skewness and HISTO_Kurtosis were significantly higher ($p < 0.001$) in non-responders' lesions than in responders' lesions before and after PRRT. Indeed, for such features, we also assessed the delta radiomics. After PRRT, in responsive lesions (SD + PR + CR) we observed a mean percentage reduction for ΔHISTO_Skewness (-3.31%±664.3%) and a mean percentage increase for ΔHISTO_Kurtosis (15.98%±71.4%). Differently, for progressive lesions (PD), we observed a higher mean percentage increase for ΔHISTO_Skewness (112.54%±348.3%;

p = 0.209) and for ΔHISTO_Kurtosis (5.81%±52.3%), less evident than responsive/stable lesions (p = 0.255).

We also performed a site-dependent sub-analysis for the most represented districts of our cohort (lymph node, liver, and bone), evaluating all the most significant pre-PRRT PET/CT features in response to PRRT prediction, also considering the ΔHISTO_Skewness and ΔHISTO_Kurtosis. The following PET features showed a statistically significant difference between responder and non-responder lesions at the Mann–Whitney test: for the lymph node lesions (n = 91; 41 in 91 non-responsive and 50 in 91 responsive), SUVmin and SUVmean (both p<0.028); metabolic tumor volume (MTV; p<0.0028); HISTO_Skewness and HISTO_Kurtosis (both p<0.028); shape (mL, p=0.012). For liver lesions (n = 169; 61 in 169 non-responsive and 108/169 responsive), MTV (p<0.001), all HISTO features (p < 0.041), GLCM_Energy (p=0.05), and GLCM_Entropy (p=0.048). Finally, for bone lesions (n = 42; 24 in 42 nonresponsive and 18 in 42 responsive), only HISTO_Skewness and HISTO_Kurtosis (both p<0.014) showed a statistically significant difference between responder and non-responder lesions. The mean values of HISTO_Skewness, HISTO_Kurtosis and SUVmax for responder and non-responder patients in the three districts are presented in Table 4.

Table 4. *The values of HISTO_Skewness, HISTO_Kurtosis, and SUVmax (median DS, range) for responder and non-responder patients in the three main districts affected by the disease.*

District	Responders	Non-Responders	*p*
Lymph nodes (n = 91)			
HISTO_Skewness	2.01 ± 2.12 (−1.10–7.66)	3.02 ± 1.44 (0.02–5.60)	**0.006**
HISTO_Kurtosis	11.03 ± 11.79 (1.66–60.40)	13.72 ± 8.85 (1.85–36.05)	**0.028**
SUV_{max}	18.67 ± 12.14 (2.88–51.88)	18.16 ± 13.86 (2.77–75.17)	0.738
Liver (n = 169)			
HISTO_Skewness	1.35 ± 2.25 (−4.47–7.66)	3.63 ± 1.90 (−0.51–7.63)	**0.0001**
HISTO_Kurtosis	9.04 ± 11.90 (1.81–60.40)	19.34 ± 13.86 (1.75–60.09)	**0.0001**
SUV_{max}	19.39 ± 10.17 (4.91–55.86)	20.87–10.14 (9.12–55.26)	0.326
Bone (n = 42)			
HISTO_Skewness	2.40 ± 1.89 (0.51–6.67)	4.03 ± 1.87 (0.49–7.74)	**0.014**
HISTO_Kurtosis	11.57 ± 12.83 (2.35–48.00)	23.13 ± 15.46 (2.17–61.34)	**0.015**
SUV_{max}	10.31 ± 9.41 (2.06–36.07)	28.42 ± 28.61 (1.67–93.50)	**0.047**

For the lymph node district, the AUC of HISTO_Skewness was 0.67 (best cut-off at 2.45 with a sensibility and specificity of 76% and 60%, respectively), while the AUC of HISTO_Kurtosis was 0.64 (best cut-off at 8.10 with a sensibility and specificity of 76% and 58%, respectively). For the liver district, the AUC of HISTO_Skewness was 0.76 (best cut-off at 1.94 with a sensibility and specificity of 87% and 67%, respectively), while the AUC of HISTO_Kurtosis was 0.75 (best cut-off at 6.55 with a sensibility and specificity of 87% and 68%, respectively). For the bone district, the AUC of HISTO_Skewness was 0.73 (best cut-off at 3.33 with a sensibility and specificity of 79% and 78%, respectively), while the AUC of HISTO_Kurtosis was 0.72 (best cut-off at 15.33 with a sensibility and specificity of 79% and 78%, respectively). For the other before-mentioned parameters, the ROC curve was not informative (AUC < 0.5).

Finally, in Table 5 we summarized the results of the per-site sub-analysis performed on the Δradiomics of HISTO_Skewness and HISTO_Kurtosis. Accordingly, only ΔHISTO_Skewness for the liver district and ΔHISTO_Kurtosis for the bone district showed a statistically significant difference between PRRT responder and non-responder lesions (p=0.031 and p=0.022, respectively). However, the ROC curve for these two parameters was not informative (AUC < 0.6), probably related to the small sample analyzed.

Table 5. *The values of ΔHISTO_Skewness and ΔHISTO_Kurtosis (median ± DS, range) for PRRT responder and non-responder lesions in the three main districts affected by the disease.*

District	Responders	Non-Responders	*p*
Lymph node (*n* = 91)			
ΔHISTO_Skewness	21.18 ± 265.75% (−880.0–1533.3)	176.83 ± 469.34% (−96.3–2550.0)	0.886
ΔHISTO_Kurtosis	13.97 ± 83.08% (−82.9–340.5)	−4.48 ± 40.84% (−85.2–96.2)	0.604
Liver (*n* = 169)			
ΔHISTO_Skewness	−17.72 ± 865.36% (−6300.0–4800.0)	134.23 ± 324.32% (−180.00–1203.82)	**0.031**
ΔHISTO_Kurtosis	9.76 ± 52.45% (−94.83–193.68)	14.64 ± 60.64% (−94.07–175.68)	0.906
Bone (n = 42)			
ΔHISTO_Skewness	6.84 ± 70.95% (−125.0–134.53)	−24.54 ± 71.06% (−240.8–56.6)	0.334
ΔHISTO_Kurtosis	66.15 ± 113.10% (−28.1–338.5)	−0.33 ± 41.43% (−55.7–103.7)	**0.022**

5.4.5. Discussion and conclusion

In our model, the [68Ga]Ga-DOTATOC PET/CT radiomics features "HISTO_Skewness" and "HISTO_Kurtosis" were able to predict the PRRT response based on a lesion for primary tumors as well as metastasis regardless of the origin with an AUC ROC, sensitivity, and specificity of 0.745, 80.6%, 67.2%, and 0.722, 61.2%, 15.9%, respectively, vs. 0.523 for the SUVmax that was not significant to predict the response to PRRT ($p = 0.49$). Moreover, the combination of two radiomics features (HISTO_Skewness; HISTO_Kurtosis) together with one clinical feature (Grading) was able to predict the PRRT response with an AUC ROC, sensitivity, and specificity of 0.744, 66.4%, and 70.3%, respectively, but did not improve the accuracy over the HISTO_Skewness.

So far, very few studies have investigated the role of ML in the prediction of response to PRRT in GEP-NET patients. Wetz et al. have reported on the predictive role of "asphericity" in GEP-NET patients enrolled for PRRT [137]. They observed that a higher level of "asphericity" was associated with poorer outcomes. However, compared to our study investigating [68Ga]Ga-DOTATOC PET/CT, features were derived from [111In]DTPA0-octreotide scintigraphy, which has a lower affinity to SSTR2 compared to PET radiopharmaceuticals, and different image modalities than PET/CT and/or PET/MRI. More recently, Önner et al. assessed the value of two predefined first-order features, "skewness" and "kurtosis" (interestingly the same to our study), in the prediction of response to PRRT in 22 GEP-NET patients for a total of 326 lesions [138]. Differently from our study, they considered SD as a non-response to PRRT, even if in the clinical practice the stability of disease is a warranted result in this scenario considering that PRRT is approved for progressive, metastatic, and usually heavily treated NET patients. Similar to our results, they observed that such features were significantly higher in non-responder patients ($p<0.001$ for skewness and $p=0.004$ for kurtosis, vs. a $p<0.001$ in our study for both).

In a different scenario from our paper (survival analysis), Werner et al. described their experience in a multicentric cohort of 142 NET patients (108/142 GEP NET) applying predefined features. The authors reported that four features, namely "entropy" (similar to our results for lymph node lesions), "correlation", "short-zone emphasis", and "homogeneity", provided a significant distinction between responders from non-responders. Furthermore, "entropy" proved to be independently associated with PFS

and OS, while “skewness” was independently associated with OS. Moreover, conventional PET parameters did not predict any of these outcomes [136]. Similarly, in our study, we observed that the SUVmax was not significant to predict the response to PRRT ($p = 0.49$), and only slightly significant for the distinction between PRRT responder and non-responder bone lesions ($p = 0.047$). The same group later observed, in 31 pNET (G1-G2) patients who underwent PRRT, that a cut-off > 6.7 for “entropy” reached a significant predictive ability for longer OS (AUC 0.71) [131].

Moreover, in our study, for the most statistically significant PET features, we assessed the percentage variations in terms of delta radiomics: in responsive/stable lesions, we observed a mean % reduction for ΔHISTO_Skewness (-3.3%±664.3%) and a mean % increase for ΔHISTO_Kurtosis (16%±71.4%); for progressive lesions, we observed a mean % increase for ΔHISTO_Skewness (112.5%±348.3%) and ΔHISTO_Kurtosis (5.8%±52.3%), less evident than for responsive/stable lesions. In a small, heterogeneous NET cohort [135], Weber et al. applied textural analysis to [68Ga]Ga-DOTATOC PET/MRI liver lesions before and after PRRT at different dosages/radiopharmaceuticals using only predefined features. In terms of delta radiomics, they observed that patients undergoing therapy with SSA showed a trend in “entropy” decrease (-0.07±0.16) when compared to patients undergoing PRRT (0.14±0.43).

In our preliminary experience, we aimed to give weight to a predictive model of response to PRRT based on the most significant [68Ga]Ga-DOTATOC PET/CT features. In the lesion progression prediction, a HISTO_Skewness = 2.45 reached an AUC ROC of 0.745 (sensitivity 80.6%, specificity 67.2%) and a HISTO_Kurtosis = 6.94 reached an AUC ROC of 0.722 (sensitivity 61.2%, specificity 75.9%), with similar results if considered together with clinical parameters.

Moreover, in the district sub-analysis, we observed that Δradiomics has a different tendency to increase or decrease for each feature, thus further reflecting NET’s heterogeneity in the liver (often extensive lesions with central necrosis) bone (often mixed and small lesions) and lymph node (possible desmoplastic reaction) [33].

As already stated, both [68Ga]Ga-DOTATOC PET/CT SUVmax and PET lesion volume are considered suboptimal parameters to assess the response to PRRT. Therefore, the potential added value of RFs is to provide prognostic additional information to conventional parameters, and HISTO_Skewness and HISTO_Kurtosis belong to this subset of features, as previously demonstrated [119]. The opportunity to

assess for each patient the single lesion's heterogeneity and predict each lesion's response to PRRT would enhance physicians to early address patients to the best options of care, reducing costs and potential toxicities [134], improving quality of life and survival.

The presented preliminary "theragnomics" model proved to be superior to conventional quantitative parameters to predict the response of GEP-NET lesions in patients treated with complete [177Lu]Lu-DOTATOC PRRT, regardless of the lesion site.

CHAPTER 6

6.1 DISCUSSION

Because PET radiomics in NENs is still in its early stages, especially applied to [68Ga]Ga-DOTA-labelled somatostatin analog PET/CT, the methodology is less standardized and studies are more explorative compared to radiomics studies in other fields.

For that reason, in this doctoral research, we have developed both technical and clinical studies. The technical studies developed respectively concerning the phantom, the creation of a semi-automatic segmentation approach, and the impact of reconstruction algorithms are a small step towards the unresolved harmonization problem of all the pre-processing steps required to ensure repeatability and reproducibility of data and results. However, we evaluated only a few of the many variables that must be taken into account to achieve robust semiquantitative or radiomic features, such as variabilities in scanner hardware from different manufacturers, injected activity, acquisition time after injection for functional imaging, acquisition time per bed position, CT parameters used for attenuation correction of PET data, matrix size, slice thickness of reconstructed images, respiratory motion, PET reconstruction algorithm and other post-reconstruction steps, such as the size of bin and segmentation methods used. This highlights the need for standardization, especially if such image analysis approaches are tested in multicenter studies [7, 22, 26, 61]. Indeed, in the future, our technical studies will have to be replicated in a multi-center setting to be validated.

In our clinical studies, we examined the potential of radiomics for several key objectives in the management of NENs patients: prediction of tumor grade, prognostic assessment, and prediction of response to PRRT. Despite the attractive results reported above, there is still considerable work required to apply the results of this research in clinical practice: a sufficiently large and homogeneous study sample is hardly available due to the rarity of NENs, patients with NENs hardly perform a dual-imaging with [18F]F-FDG and [68Ga]Ga-DOTA-peptides PET to evaluate the “NETPET score”, the inherent heterogeneity of these tumors makes a standardized approach in the methodology applied to PET imaging difficult compared to other tumors (high variability of uptake for both [18F]F-FDG and [68Ga]Ga-DOTA-peptides imaging compared to other tumors), these are mostly exploratory and univariable analyses with a

lack of external validation. Despite this, some encouraging results obtained through the above-mentioned articles suggest that a significant role in 'non-invasive' patient management in the clinical practice and in the clinical decision support system (CDSS) could be played by some RFs in the future, such as first-order statistics (such as entropy), metabolic tumor burden (MTB) from [18F]F-FDG PET/CT images, somatostatin receptor tumor burden (SRTB) from [68Ga]Ga-DOTA-peptides PET/CT images and GLRLM features.

Finally, as part of the results of this doctoral project, the publication of negative results regarding the use of radiomics in lung neuroendocrine tumors was also very relevant: indeed, the publication of negative findings in the field of radiomics is equally important to that of positive results to understand the directions for meaningful research that will bring the field to the next level.

6.2 CONCLUSION

In conclusion, the results obtained from our research are promising but need to be further investigated in a multi-center setting to assess possible validation. In this scenario, based on the results of our studies, technical studies and clinical studies that used radiomics for the prediction of response or long-term outcome seem to be more relevant endpoints comparing with studies focus on the identification of tumor grade, since these latter presumably require even more large and homogeneous samples and the availability of several data (histopathological, genetic, radiological and nuclear medical).

BIBLIOGRAPHY

1. Lambin P, Leijenaar RTH, Deist TM, et al (2017) Radiomics: The bridge between medical imaging and personalized medicine. In: Nat. Rev. Clin. Oncol. https://www.ncbi.nlm.nih.gov/pubmed/?term=Lambin++Radiomics%3A+the+bridge+between+medical+imaging+and+personalized+medicine. Accessed 7 Feb 2020
2. Cook GJR, Azad G, Owczarczyk K, et al (2018) Challenges and Promises of PET Radiomics. Int J Radiat Oncol Biol Phys 102:1083–1089. https://doi.org/10.1016/j.ijrobp.2017.12.268
3. Yousefirizi F, Pierre Decazes, Amyar A, et al (2022) AI-Based Detection, Classification and Prediction/Prognosis in Medical Imaging:: Towards Radiophenomics. PET Clin. 17:183–212
4. Serkova NJ (2011) Translational imaging endpoints to predict treatment response to novel targeted anticancer agents. Drug Resist Updat 14:224–235. https://doi.org/10.1016/j.drup.2011.04.004
5. James ML, Gambhir SS (2012) A molecular imaging primer: Modalities, imaging agents, and applications. Physiol. Rev. 92:897–965
6. Jennings M, Marcu LG, Bezak E (2015) PET-specific parameters and radiotracers in theoretical tumour modelling. Comput Math Methods Med 2015:415923. https://doi.org/10.1155/2015/415923
7. Lovinfosse P, Visvikis D, Hustinx R, Hatt M (2018) FDG PET radiomics: a review of the methodological aspects. Clin. Transl. Imaging 6:379–391
8. Gerlinger M, Rowan AJ, Horswell S, et al (2012) Intratumor heterogeneity and branched evolution revealed by multiregion sequencing. N Engl J Med 366:883–892. https://doi.org/10.1056/NEJMoa1113205
9. Ziv E, Durack JC, Solomon SB (2016) The Importance of Biopsy in the Era of Molecular Medicine. Cancer J. (United States) 22:418–422
10. McQuerry JA, Chang JT, Bowtell DDL, et al (2017) Mechanisms and clinical implications of tumor heterogeneity and convergence on recurrent phenotypes. J. Mol. Med. 95:1167–1178
11. Grillo F, Albertelli M, Brisigotti MP, et al (2016) Grade increases in

gastroenteropancreatic neuroendocrine tumor metastases compared to the primary tumor. Neuroendocrinology 103:452–459. https://doi.org/10.1159/000439434

12. Oronsky B, Ma PC, Morgensztern D, Carter CA (2017) Nothing But NET: A Review of Neuroendocrine Tumors and Carcinomas. Neoplasia (United States) 19:991–1002
13. Simbolo M, Mafficini A, Sikora KO, et al (2017) Lung neuroendocrine tumours: deep sequencing of the four World Health Organization histotypes reveals chromatin-remodelling genes as major players and a prognostic role for TERT, RB1, MEN1 and KMT2D. J Pathol 241:488–500. https://doi.org/10.1002/path.4853
14. Inzani F, Petrone G, Rindi G (2018) The New World Health Organization Classification for Pancreatic Neuroendocrine Neoplasia. Endocrinol. Metab. Clin. North Am. 47:463–470
15. Klimstra DS (2016) Pathologic Classification of Neuroendocrine Neoplasms. Hematol. Oncol. Clin. North Am. 30:1–19
16. Hofland J, Kaltsas G, de Herder WW (2020) Advances in the Diagnosis and Management of Well-Differentiated Neuroendocrine Neoplasms. Endocr Rev 41:. https://doi.org/10.1210/endrev/bnz004
17. Tirosh A, Kebebew E (2018) The utility of 68Ga-DOTATATE positron-emission tomography/computed tomography in the diagnosis, management, follow-up and prognosis of neuroendocrine tumors. Futur Oncol 14:111–122. https://doi.org/10.2217/fon-2017-0393
18. Giovannini E, Giovacchini G, Borsò E, et al (2018) [68 Ga]-Dota Peptide PET/CT in Neuroendocrine Tumors: Main Clinical Applications. Curr Radiopharm 12:11–22. https://doi.org/10.2174/1874471012666181212101244
19. Carideo L, Prosperi D, Panzuto F, et al (2019) Role of Combined [68Ga]Ga-DOTA-SST Analogues and [18F]FDG PET/CT in the Management of GEP-NENs: A Systematic Review. J Clin Med 8:1032. https://doi.org/10.3390/jcm8071032
20. Chan DLH, Pavlakis N, Schembri GP, et al (2017) Dual somatostatin receptor/FDG PET/CT imaging in metastatic neuroendocrine tumours: Proposal for a novel grading scheme with prognostic significance. Theranostics 7:1149–1158. https://doi.org/10.7150/thno.18068

21. Hatt M, Tixier F, Pierce L, et al (2017) Characterization of PET/CT images using texture analysis: the past, the present… any future? Eur. J. Nucl. Med. Mol. Imaging 44:151–165
22. Ha S, Choi H, Paeng JC, Cheon GJ (2019) Radiomics in Oncological PET/CT: a Methodological Overview. Nucl. Med. Mol. Imaging (2010). 53:14–29
23. Lambin P, Rios-Velazquez E, Leijenaar R, et al (2012) Radiomics: Extracting more information from medical images using advanced feature analysis. Eur J Cancer 48:441–446. https://doi.org/10.1016/j.ejca.2011.11.036
24. Gillies RJ, Kinahan PE, Hricak H (2016) Radiomics: Images are more than pictures, they are data. Radiology 278:563–577. https://doi.org/10.1148/radiol.2015151169
25. Sanduleanu S, Woodruff HC, de Jong EEC, et al (2018) Tracking tumor biology with radiomics: A systematic review utilizing a radiomics quality score. Radiother. Oncol. 127:349–360
26. Zwanenburg A (2019) Radiomics in nuclear medicine: robustness, reproducibility, standardization, and how to avoid data analysis traps and replication crisis. Eur J Nucl Med Mol Imaging 46:2638–2655. https://doi.org/10.1007/s00259-019-04391-8
27. Castiglioni I, Gilardi MC (2018) Radiomics: is it time to compose the puzzle? Clin Transl Imaging 6:411–413. https://doi.org/10.1007/s40336-018-0302-y
28. O'Connor JPB, Aboagye EO, Adams JE, et al (2017) Imaging biomarker roadmap for cancer studies. Nat Rev Clin Oncol 14:169–186. https://doi.org/10.1038/nrclinonc.2016.162
29. Zwanenburg A, Vallières M, Abdalah MA, et al (2020) The image biomarker standardization initiative: Standardized quantitative radiomics for high-throughput image-based phenotyping. Radiology 295:328–338. https://doi.org/10.1148/radiol.2020191145
30. Bailly C, Bodet-Milin C, Bourgeois M, et al (2019) Exploring tumor heterogeneity using PET imaging: The big picture. Cancers (Basel). 11
31. Yao JC, Hassan M, Phan A, et al (2008) One hundred years after "carcinoid": Epidemiology of and prognostic factors for neuroendocrine tumors in 35,825 cases in the United States. J Clin Oncol 26:3063–3072. https://doi.org/10.1200/JCO.2007.15.4377
32. Castaño JP, Sundin A, Maecke HR, et al (2014) Gastrointestinal neuroendocrine

tumors (NETs): New diagnostic and therapeutic challenges. Cancer Metastasis Rev 33:353–359. https://doi.org/10.1007/s10555-013-9465-1

33. Modlin IM, Oberg K, Chung DC, et al (2008) Gastroenteropancreatic neuroendocrine tumours. Lancet Oncol. 9:61–72
34. Deroose CM, Hindié E, Kebebew E, et al (2016) Molecular imaging of gastroenteropancreatic neuroendocrine tumors: Current status and future directions. J Nucl Med 57:1949–1956. https://doi.org/10.2967/jnumed.116.179234
35. Mafficini A, Scarpa A (2019) Genetics and Epigenetics of Gastroenteropancreatic Neuroendocrine Neoplasms. Endocr Rev 40:506–536. https://doi.org/10.1210/er.2018-00160
36. Kwekkeboom DJ, De Herder WW, Kam BL, et al (2008) Treatment with the radiolabeled somatostatin analog [177Lu- DOTA0,Tyr3]octreotate: Toxicity, efficacy, and survival. J Clin Oncol 26:2124–2130. https://doi.org/10.1200/JCO.2007.15.2553
37. Dasari A, Shen C, Halperin D, et al (2017) Trends in the incidence, prevalence, and survival outcomes in patients with neuroendocrine tumors in the United States. JAMA Oncol 3:1335–1342. https://doi.org/10.1001/jamaoncol.2017.0589
38. Li X, Hou Y, Shi T, et al (2020) Clinicopathological characteristics and genetic analysis of pulmonary carcinoid tumors: A single-center retrospective cohort study and literature review. Oncol Lett 19:2446–2456. https://doi.org/10.3892/ol.2020.11347
39. Sundin A, Arnold R, Baudin E, et al (2017) ENETS Consensus Guidelines for the Standards of Care in Neuroendocrine Tumors: Radiological, Nuclear Medicine and Hybrid Imaging. In: Neuroendocrinology. S. Karger AG, pp 212–244
40. Uccella S, La Rosa S, Volante M, Papotti M (2018) Immunohistochemical Biomarkers of Gastrointestinal, Pancreatic, Pulmonary, and Thymic Neuroendocrine Neoplasms. Endocr. Pathol. 29:150–168
41. Ćwikła JB, Bodei L, Kolasinska-Ćwikła A, et al (2015) Circulating transcript analysis (NETest) in GEP-NETs treated with somatostatin analogs defines therapy. J Clin Endocrinol Metab 100:E1437–E1445. https://doi.org/10.1210/jc.2015-2792
42. Hofland J, Zandee WT, de Herder WW (2018) Role of biomarker tests for

diagnosis of neuroendocrine tumours. Nat. Rev. Endocrinol. 14:656–669

43. Papotti M, Bongiovanni M, Volante M, et al (2002) Expression of somatostatin receptor types 1-5 in 81 cases of gastrointestinal and pancreatic endocrine tumors: A correlative immunohistochemical and reverse-transcriptase polymerase chain reaction analysis. Virchows Arch 440:461–475. https://doi.org/10.1007/s00428-002-0609-x
44. Lamberts SWJ, Reubi JC, Krenning EP (1993) Validation of somatostatin receptor scintigraphy in the localization of neuroendocrine tumors. Acta Oncol (Madr) 32:167–170. https://doi.org/10.3109/02841869309083907
45. Krenning EP, Breeman WAP, Kooij PPM, et al (1989) LOCALISATION OF ENDOCRINE-RELATED TUMOURS WITH RADIOIODINATED ANALOGUE OF SOMATOSTATIN. Lancet 333:242–244. https://doi.org/10.1016/S0140-6736(89)91258-0
46. Geijer H, Breimer LH (2013) Somatostatin receptor PET/CT in neuroendocrine tumours: Update on systematic review and meta-analysis. Eur. J. Nucl. Med. Mol. Imaging 40:1770–1780
47. Pauwels E, Cleeren F, Bormans G, Deroose CM (2018) Somatostatin receptor PET ligands - the next generation for clinical practice. Am J Nucl Med Mol Imaging 8:311–331
48. Bozkurt MF, Virgolini I, Balogova S, et al (2017) Guideline for PET/CT imaging of neuroendocrine neoplasms with 68Ga-DOTA-conjugated somatostatin receptor targeting peptides and 18F–DOPA. Eur J Nucl Med Mol Imaging 44:1588–1601. https://doi.org/10.1007/s00259-017-3728-y
49. Zaknun JJ, Bodei L, Mueller-Brand J, et al (2013) The joint IAEA, EANM, and SNMMI practical guidance on peptide receptor radionuclide therapy (PRRNT) in neuroendocrine tumours. Eur. J. Nucl. Med. Mol. Imaging 40:800–816
50. Virgolini I, Ambrosini V, Bomanji JB, et al (2010) Procedure guidelines for PET/CT tumour imaging with 68Ga-DOTA- conjugated peptides: 68Ga-DOTA-TOC, 68Ga-DOTA-NOC, 68Ga-DOTA-TATE. Eur J Nucl Med Mol Imaging 37:2004–2010. https://doi.org/10.1007/s00259-010-1512-3
51. Panagiotidis E, Alshammari A, Michopoulou S, et al (2017) Comparison of the impact of 68Ga-DOTATATE and 18F-FDG PET/CT on clinical management in patients with Neuroendocrine tumors. J Nucl Med 58:91–96. https://doi.org/10.2967/jnumed.116.178095

52. Strosberg J (2018) 177Lutetium-Dotatate delays decline in quality of life in patients with midgut neuroendocrine tumors. Oncotarget 9:33059–33059
53. Liberini V, Huellner MW, Grimaldi S, et al (2020) The Challenge of Evaluating Response to Peptide Receptor Radionuclide Therapy in Gastroenteropancreatic Neuroendocrine Tumors: The Present and the Future. Diagnostics 10:1083. https://doi.org/10.3390/diagnostics10121083
54. Albertelli M, Dotto A, Di Dato C, et al (2020) PRRT: identikit of the perfect patient. Rev. Endocr. Metab. Disord. 1–17
55. Singh S, Asa SL, Dey C, et al (2016) Diagnosis and management of gastrointestinal neuroendocrine tumors: An evidence-based Canadian consensus. Cancer Treat. Rev. 47:32–45
56. Zwanenburg A, Vallières M, Abdalah MA, et al (2020) The image biomarker standardization initiative: Standardized quantitative radiomics for high-throughput image-based phenotyping. Radiology 295:328–338. https://doi.org/10.1148/radiol.2020191145
57. Mayerhoefer ME, Materka A, Langs G, et al (2020) Introduction to Radiomics. J. Nucl. Med. 61:488–495
58. Zwanenburg A, Leger S, Vallières M, Löck S (2016) Image biomarker standardisation initiative
59. Gatta R, Depeursinge A, Ratib O, et al (2020) Integrating radiomics into holomics for personalised oncology: from algorithms to bedside. Eur. Radiol. Exp. 4
60. Duron L, Balvay D, Perre S Vande, et al (2019) Gray-level discretization impacts reproducible MRI radiomics texture features. PLoS One 14:. https://doi.org/10.1371/journal.pone.0213459
61. Traverso A, Wee L, Dekker A, Gillies R (2018) Repeatability and Reproducibility of Radiomic Features: A Systematic Review. Int J Radiat Oncol Biol Phys 102:1143–1158. https://doi.org/10.1016/j.ijrobp.2018.05.053
62. Hatt M, Krizsan AK, Rahmim A, et al (2022) Joint EANM/SNMMI guideline on radiomics in nuclear medicine. Eur J Nucl Med Mol Imaging 1–24. https://doi.org/10.1007/s00259-022-06001-6
63. Bailly C, Bodet-Milin C, Couespel S, et al (2016) Revisiting the Robustness of PET-Based Textural Features in the Context of Multi-Centric Trials. PLoS One 11:e0159984. https://doi.org/10.1371/journal.pone.0159984

64. Orlhac F, Thézé B, Soussan M, et al (2016) Multiscale Texture Analysis: From 18F-FDG PET Images to Histologic Images. J Nucl Med 57:1823–1828. https://doi.org/10.2967/jnumed.116.173708
65. Tixier F, Hatt M, Le Rest CC, et al (2012) Reproducibility of tumor uptake heterogeneity characterization through textural feature analysis in 18F-FDG PET. J Nucl Med 53:693–700. https://doi.org/10.2967/jnumed.111.099127
66. Leijenaar RTH, Carvalho S, Velazquez ER, et al (2013) Stability of FDG-PET Radiomics features: An integrated analysis of test-retest and inter-observer variability. Acta Oncol (Madr) 52:1391–1397. https://doi.org/10.3109/0284186X.2013.812798
67. van Velden FHP, Kramer GM, Frings V, et al (2016) Repeatability of Radiomic Features in Non-Small-Cell Lung Cancer [18F]FDG-PET/CT Studies: Impact of Reconstruction and Delineation. Mol Imaging Biol 18:788–795. https://doi.org/10.1007/s11307-016-0940-2
68. Weber WA, Gatsonis CA, David Mozley P, et al (2015) Repeatability of 18F-FDG PET/CT in advanced non-small cell lung cancer: Prospective assessment in 2 multicenter trials. J Nucl Med 56:1137–1143. https://doi.org/10.2967/jnumed.114.147728
69. Balon HR, Brown TLY, Goldsmith SJ, et al (2011) The SNM practice guideline for somatostatin receptor scintigraphy 2.0. J Nucl Med Technol 39:317–324. https://doi.org/10.2967/jnmt.111.098277
70. Oberg K, Modlin IM, De Herder W, et al (2015) Consensus on biomarkers for neuroendocrine tumour disease. Lancet Oncol. 16:e435–e446
71. Nioche C, Orlhac F, Boughdad S, et al (2018) Lifex: A freeware for radiomic feature calculation in multimodality imaging to accelerate advances in the characterization of tumor heterogeneity. Cancer Res 78:4786–4789. https://doi.org/10.1158/0008-5472.CAN-18-0125
72. Foster B, Bagci U, Mansoor A, et al (2014) A review on segmentation of positron emission tomography images. Comput. Biol. Med. 50:76–96
73. Boellaard R, Delgado-Bolton R, Oyen WJG, et al (2015) FDG PET/CT: EANM procedure guidelines for tumour imaging: version 2.0. Eur. J. Nucl. Med. Mol. Imaging 42:328–354
74. Chan TF, Vese LA (2001) Active contours without edges. IEEE Trans Image Process 10:266–277. https://doi.org/10.1109/83.902291

75. Altazi BA, Zhang GG, Fernandez DC, et al (2017) Reproducibility of F18-FDG PET radiomic features for different cervical tumor segmentation methods, gray-level discretization, and reconstruction algorithms. J Appl Clin Med Phys 18:32–48. https://doi.org/10.1002/acm2.12170
76. Orlhac F, Soussan M, Chouahnia K, et al (2015) 18F-FDG PET-derived textural indices reflect tissue-specific uptake pattern in non-small cell lung cancer. PLoS One 10:e0145063. https://doi.org/10.1371/journal.pone.0145063
77. Orlhac F, Nioche C, Soussan M, Buvat I (2017) Understanding changes in tumor texture indices in PET: A comparison between visual assessment and index values in simulated and patient data. J Nucl Med 58:387–392. https://doi.org/10.2967/jnumed.116.181859
78. Leijenaar RTH, Nalbantov G, Carvalho S, et al (2015) The effect of SUV discretization in quantitative FDG-PET Radiomics: The need for standardized methodology in tumor texture analysis. Sci Rep 5:. https://doi.org/10.1038/srep11075
79. Freeman JL, Jafri SZ, Roberts JL, et al (1993) CT of congenital and acquired abnormalities of the spleen. Radiographics 13:597–610
80. Varga I, Babala J, Kachlik D (2018) Anatomic variations of the spleen: current state of terminology, classification, and embryological background. Surg. Radiol. Anat. 40:21–29
81. HALPERT B, GYORKEY F (1957) Accessory spleen in the tail of the pancreas. A M A Arch Pathol 64:266–269
82. Kim SH, Lee JM, Han JK, et al (2006) MDCT and superparamagnetic iron oxide (SPIO)-enhanced MR findings of intrapancreatic accessory spleen in seven patients. Eur Radiol 16:1887–1897. https://doi.org/10.1007/s00330-006-0193-6
83. Kawamoto S, Johnson PT, Hall H, et al (2012) Intrapancreatic accessory spleen: CT appearance and differential diagnosis. Abdom Imaging 37:812–827. https://doi.org/10.1007/s00261-011-9830-x
84. Hamada T, Isaji S, Mizuno S, et al (2004) Laparoscopic spleen-preserving pancreatic tail resection for an intrapancreatic accessory spleen mimicking a nonfunctioning endocrine tumor: Report of a case. Surg Today 34:878–881. https://doi.org/10.1007/s00595-004-2839-9
85. Prasad V, Baum RP (2010) Biodistribution of the Ga-68 labeled somatostatin analogue DOTA-NOC in patients with neuroendocrine tumors: Characterization

of uptake in normal organs and tumor lesions. Q J Nucl Med Mol Imaging 54:61–67

86. Mansor S, Pfaehler E, Heijtel D, et al (2017) Impact of PET/CT system, reconstruction protocol, data analysis method, and repositioning on PET/CT precision: An experimental evaluation using an oncology and brain phantom: An. Med Phys 44:6413–6424. https://doi.org/10.1002/mp.12623
87. Ahn S, Fessler JA (2003) Globally convergent image reconstruction for emission tomography using relaxed ordered subsets algorithms. IEEE Trans Med Imaging 22:613–626. https://doi.org/10.1109/TMI.2003.812251
88. Schwyzer M, Ferraro DA, Muehlematter UJ, et al (2018) Automated detection of lung cancer at ultralow dose PET/CT by deep neural networks – Initial results. Lung Cancer 126:170–173. https://doi.org/10.1016/j.lungcan.2018.11.001
89. Aljared A, Alharbi AA, Huellner MW (2018) BSREM Reconstruction for Improved Detection of In-Transit Metastases with Digital FDG-PET/CT in Patients with Malignant Melanoma. Clin Nucl Med 43:370–371. https://doi.org/10.1097/RLU.0000000000002024
90. Sah BR, Stolzmann P, Delso G, et al (2017) Clinical evaluation of a block sequential regularized expectation maximization reconstruction algorithm in 18F-FDG PET/CT studies. Nucl Med Commun 38:57–66. https://doi.org/10.1097/MNM.0000000000000604
91. Teoh EJ, McGowan DR, Bradley KM, et al (2016) Novel penalised likelihood reconstruction of PET in the assessment of histologically verified small pulmonary nodules. Eur Radiol 26:576–584. https://doi.org/10.1007/s00330-015-3832-y
92. Lindström E, Sundin A, Trampal C, et al (2018) Evaluation of penalized-likelihood estimation reconstruction on a digital time-of-flight PET/CT scanner for 18 F-FDG whole-body examinations. J Nucl Med 59:1152–1158. https://doi.org/10.2967/jnumed.117.200790
93. Khamis H WS MotionFree: device-less digital respiratory gating technique, seamlessly integrated in PET imaging routine. Gen Electr Co
94. Walker MD, Morgan AJ, Bradley KM, McGowan DR (2019) Evaluation of data-driven respiratory gating waveforms for clinical PET imaging. EJNMMI Res 9:. https://doi.org/10.1186/s13550-018-0470-9
95. Brandner ED, Wu A, Chen H, et al (2006) Abdominal organ motion measured

using 4D CT. Int J Radiat Oncol Biol Phys 65:554–560. https://doi.org/10.1016/j.ijrobp.2005.12.042

96. De Ponti E, Morzenti S, Crivellaro C, et al (2018) Motion Management in PET/CT: Technological Solutions. Curr Radiopharm 11:79–85. https://doi.org/10.2174/1874471011666180419150440
97. Guerra L, Ponti E De, Morzenti S, et al (2017) Respiratory Motion Management in PET/CT: Applications and Clinical Usefulness. Curr Radiopharm 10:. https://doi.org/10.2174/1874471010666170519165918
98. Kesner A, Schmidtlein CR, Kuntner C (2019) Real-time data-driven motion correction in PET. EJNMMI Phys. 6:3
99. Catalano OA, Umutlu L, Fuin N, et al (2018) Comparison of the clinical performance of upper abdominal PET/DCE-MRI with and without concurrent respiratory motion correction (MoCo). Eur J Nucl Med Mol Imaging 45:2147–2154. https://doi.org/10.1007/s00259-018-4084-2
100. Travis WD, Brambilla E, Nicholson AG, et al (2015) The 2015 World Health Organization Classification of Lung Tumors: Impact of Genetic, Clinical and Radiologic Advances since the 2004 Classification. J. Thorac. Oncol. 10:1243–1260
101. Limaiem F, Wallen JM (2018) Cancer, Lung Carcinoid Tumors. StatPearls Publishing
102. Jiang Y, Hou G, Cheng W (2019) The utility of 18F-FDG and 68Ga-DOTA-Peptide PET/CT in the evaluation of primary pulmonary carcinoid: A systematic review and meta-analysis. Medicine (Baltimore) 98:e14769. https://doi.org/10.1097/MD.0000000000014769
103. Abgral R, Leboulleux S, Déandreis D, et al (2011) Performance of 18fluorodeoxyglucose-positron emission tomography and somatostatin receptor scintigraphy for high Ki67 (≥10%) well-differentiated endocrine carcinoma staging. J Clin Endocrinol Metab 96:665–671. https://doi.org/10.1210/jc.2010-2022
104. Daniels CE, Lowe VJ, Aubry MC, et al (2007) The utility of fluorodeoxyglucose positron emission tomography in the evaluation of carcinoid tumors presenting as pulmonary nodules. Chest 131:255–260. https://doi.org/10.1378/chest.06-0711
105. Chong S, Lee KS, Kim BT, et al (2007) Integrated PET/CT of pulmonary neuroendocrine tumors: Diagnostic and prognostic implications. Am J

Roentgenol 188:1223–1231. https://doi.org/10.2214/AJR.06.0503

106. Lococo F, Perotti G, Cardillo G, et al (2015) Multicenter comparison of 18F-FDG and 68Ga-DOTA-peptide PET/CT for pulmonary carcinoid. Clin Nucl Med 40:e183–e189. https://doi.org/10.1097/RLU.0000000000000641
107. Polverari G, Ceci F, Bertaglia V, et al (2020) 18F-FDG pet parameters and radiomics features analysis in advanced nsclc treated with immunotherapy as predictors of therapy response and survival. Cancers (Basel) 12:. https://doi.org/10.3390/cancers12051163
108. Orlhac F, Soussan M, Chouahnia K, et al (2015) 18F-FDG PET-derived textural indices reflect tissue-specific uptake pattern in non-small cell lung cancer. PLoS One 10:145063. https://doi.org/10.1371/journal.pone.0145063
109. Hatt M, Majdoub M, Vallières M, et al (2015) 18F-FDG PET uptake characterization through texture analysis: Investigating the complementary nature of heterogeneity and functional tumor volume in a multi-cancer site patient cohort. J Nucl Med 56:38–44. https://doi.org/10.2967/jnumed.114.144055
110. Antunes P, Ginj M, Zhang H, et al (2007) Are radiogallium-labelled DOTA-conjugated somatostatin analogues superior to those labelled with other radiometals? Eur J Nucl Med Mol Imaging 34:982–993. https://doi.org/10.1007/s00259-006-0317-x
111. Rufini V, Calcagni ML, Baum RP (2006) Imaging of Neuroendocrine Tumors. Semin Nucl Med 36:228–247. https://doi.org/10.1053/j.semnuclmed.2006.03.007
112. Shah MH, Goldner WS, Halfdanarson TR, et al (2018) Neuroendocrine and adrenal tumors, version 2.2018 featured updates to the nccn guidelines. JNCCN J. Natl. Compr. Cancer Netw. 16:693–702
113. Ambrosini V, Campana D, Bodei L, et al (2010) 68Ga-DOTANOC PET/CT clinical impact in patients with neuroendocrine tumors. J Nucl Med 51:669–673. https://doi.org/10.2967/jnumed.109.071712
114. Sharma R, Wang WM, Yusuf S, et al (2019) 68Ga-DOTATATE PET/CT parameters predict response to peptide receptor radionuclide therapy in neuroendocrine tumours. Radiother Oncol 141:108–115. https://doi.org/10.1016/j.radonc.2019.09.003
115. Tirosh A, Papadakis GZ, Millo C, et al (2018) Prognostic Utility of Total 68Ga-DOTATATE-Avid Tumor Volume in Patients With Neuroendocrine Tumors. Gastroenterology 154:998-1008.e1. https://doi.org/10.1053/j.gastro.2017.11.008

116. Toriihara A, Baratto L, Nobashi T, et al (2019) Prognostic value of somatostatin receptor expressing tumor volume calculated from 68Ga-DOTATATE PET/CT in patients with well-differentiated neuroendocrine tumors. Eur J Nucl Med Mol Imaging 46:2244–2251. https://doi.org/10.1007/s00259-019-04455-9
117. Kim Y il, Yoo C, Oh SJ, et al (2020) Tumour-to-liver ratio determined by [68Ga]Ga-DOTA-TOC PET/CT as a prognostic factor of lanreotide efficacy for patients with well-differentiated gastroenteropancreatic-neuroendocrine tumours. EJNMMI Res 10:63. https://doi.org/10.1186/s13550-020-00651-z
118. Velikyan I, Sundin A, Sörensen J, et al (2014) Quantitative and qualitative intrapatient comparison of 68Ga-DOTATOC and 68Ga-DOTATATE: Net uptake rate for accurate quantification. J Nucl Med 55:204–210. https://doi.org/10.2967/jnumed.113.126177
119. Liberini V, Rampado O, Gallio E, et al (2021) 68Ga-DOTATOC PET/CT-Based Radiomic Analysis and PRRT Outcome: A Preliminary Evaluation Based on an Exploratory Radiomic Analysis on Two Patients. Front Med 7:601853. https://doi.org/10.3389/fmed.2020.601853
120. Strosberg J, El-Haddad G, Wolin E, et al (2017) Phase 3 trial of 177lu-dotatate for midgut neuroendocrine tumors. In: New England Journal of Medicine. Massachussetts Medical Society, pp 125–135
121. Oberg K, Krenning E, Sundin A, et al (2016) A delphic consensus assessment: Imaging and biomarkers in gastroenteropancreatic neuroendocrine tumor disease management. Endocr Connect 5:174–187. https://doi.org/10.1530/EC-16-0043
122. Ezziddin S, Lohmar J, Yong-Hing CJ, et al (2012) Does the pretherapeutic tumor SUV in 68Ga DOTATOC PET predict the absorbed dose of 177Lu octreotate? Clin Nucl Med 37:. https://doi.org/10.1097/RLU.0b013e31823926e5
123. Lee DY, Kim Y Il (2019) Prognostic Value of Maximum Standardized Uptake Value in 68Ga-Somatostatin Receptor Positron Emission Tomography for Neuroendocrine Tumors: A Systematic Review and Meta-analysis. Clin Nucl Med 44:777–783. https://doi.org/10.1097/RLU.0000000000002694
124. Finocchiaro D, Murray I (2020) Uncertainty analysis of tumour absorbed dose calculations in Molecular Radiotherapy. EJNMMI Phys 7:1–18. https://doi.org/10.1186/s40658-020-00328-5
125. Walrand S, Hanin FX, Pauwels S, Jamar F (2012) Tumour control probability derived from dose distribution in homogeneous and heterogeneous models:

Assuming similar pharmacokinetics, 125Sn 177Lu is superior to 90Y 177Lu in peptide receptor radiotherapy. Phys Med Biol 57:4263–4275. https://doi.org/10.1088/0031-9155/57/13/4263

126. Guerriero F, Ferrari ME, Botta F, et al (2013) Kidney dosimetry in 177Lu and 90Y peptide receptor radionuclide therapy: Influence of image timing, time-activity integration method, and risk factors. Biomed Res Int 2013:. https://doi.org/10.1155/2013/935351
127. Abdulrezzak U, Kurt YK, Kula M, Tutus A (2016) Combined imaging with 68Ga-DOTA-TATE and 18F-FDG PET/CT on the basis of volumetric parameters in neuroendocrine tumors. Nucl Med Commun 37:874–881. https://doi.org/10.1097/MNM.0000000000000522
128. Öksüz MÖ, Winter L, Pfannenberg C, et al (2014) Peptide receptor radionuclide therapy of neuroendocrine tumors with 90Y-DOTATOC: Is treatment response predictable by pre-therapeutic uptake of 68Ga-DOTATOC? Diagn Interv Imaging 95:289–300. https://doi.org/10.1016/j.diii.2013.07.006
129. Kratochwil C, Stefanova M, Mavriopoulou E, et al (2015) SUV of [68Ga]DOTATOC-PET/CT Predicts Response Probability of PRRT in Neuroendocrine Tumors. Mol Imaging Biol 17:313–318. https://doi.org/10.1007/s11307-014-0795-3
130. Gabriel M, Oberauer A, Dobrozemsky G, et al (2009) 68Ga-DOTA-Tyr3-octreotide PET for assessing response to somatostatin-receptor-mediated radionuclide therapy. J Nucl Med 50:1427–1434. https://doi.org/10.2967/jnumed.108.053421
131. Werner RA, Ilhan H, Lehner S, et al (2019) Pre-therapy Somatostatin Receptor-Based Heterogeneity Predicts Overall Survival in Pancreatic Neuroendocrine Tumor Patients Undergoing Peptide Receptor Radionuclide Therapy. Mol Imaging Biol 21:582–590. https://doi.org/10.1007/s11307-018-1252-5
132. Desai H, Borges-Neto S, Wong TZ (2019) Molecular Imaging and Therapy for Neuroendocrine Tumors. Curr Treat Options Oncol 20:78. https://doi.org/10.1007/s11864-019-0678-6
133. Bodei L, Kidd M, Modlin IM, et al (2016) Measurement of circulating transcripts and gene cluster analysis predicts and defines therapeutic efficacy of peptide receptor radionuclide therapy (PRRT) in neuroendocrine tumors. Eur J Nucl Med Mol Imaging 43:839–851. https://doi.org/10.1007/s00259-015-3250-z

134. Bodei L, Schöder H, Baum RP, et al (2020) Molecular profiling of neuroendocrine tumours to predict response and toxicity to peptide receptor radionuclide therapy. Lancet Oncol. 21:e431–e443
135. Weber M, Kessler L, Schaarschmidt B, et al (2020) Treatment-related changes in neuroendocrine tumors as assessed by textural features derived from 68Ga-DOTATOC PET/MRI with simultaneous acquisition of apparent diffusion coefficient. BMC Cancer 20:. https://doi.org/10.1186/s12885-020-06836-y
136. Werner RA, Lapa C, Ilhan H, et al (2017) Survival prediction in patients undergoing radionuclide therapy based on intratumoral somatostatin-receptor heterogeneity. Oncotarget 8:7039–7049. https://doi.org/10.18632/oncotarget.12402
137. Wetz C, Apostolova I, Steffen IG, et al (2017) Predictive Value of Asphericity in Pretherapeutic [111In]DTPA-Octreotide SPECT/CT for Response to Peptide Receptor Radionuclide Therapy with [177Lu]DOTATATE. Mol Imaging Biol 19:437–445. https://doi.org/10.1007/s11307-016-1018-x
138. Önner H, Abdülrezzak Ü, Tutuş A (2020) Could the skewness and kurtosis texture parameters of lesions obtained from pretreatment Ga-68 DOTA-TATE PET/CT images predict receptor radionuclide therapy response in patients with gastroenteropancreatic neuroendocrine tumors? Nucl Med Commun 41:1034–1039. https://doi.org/10.1097/MNM.0000000000001231

PUBLICATIONS

ARTICLES

1. Balma M. et al. The role of theragnostics in breast cancer: a systematic review of the last 12 years. In press
2. Liberini V. et al. Radiomics and artificial intelligence in prostate cancer: new tools for molecular hybrid imaging and theragnostics. Eur Radiol Exp. 2022 Jun 15;6(1):27. doi: 10.1186/s41747-022-00282-0. PMID: 35701671; PMCID: PMC9198151.
3. Ceci F. et al. Event-free survival after 68 Ga-PSMA-11 PET/CT in recurrent hormone-sensitive prostate cancer (HSPC) patients eligible for salvage therapy. Eur J Nucl Med Mol Imaging. 2022 Jul;49(9):3257-3268. doi: 10.1007/s00259-022-05741-9. Epub 2022 Feb 26. PMID: 35217883; PMCID: PMC9250462.
4. Balma M. et al. Non-conventional and Investigational PET Radiotracers for Breast Cancer: A Systematic Review. Front Med (Lausanne). 2022 Apr 12;9:881551. doi: 10.3389/fmed.2022.881551. PMID: 35492341; PMCID: PMC9039137.
5. Thuillier P. et al. Prognostic value of whole-body PET volumetric parameters extracted from 68Ga-DOTATOC-PET/CT in well-differentiated neuroendocrine tumors. J Nucl Med. 2022 Jul;63(7):1014-1020. doi: 10.2967/jnumed.121.262652. Epub 2021 Nov 5. PMID: 34740949.
6. Husmann L. et al. Staging of Alveolar Echinococcosis with PET/CT: Prediction of Benzimidazole Therapy Duration in Inoperable Patients. Sci Rep. 2022 Jul 6;12(1):11392. doi: 10.1038/s41598-022-15641-5. PMID: 35794149; PMCID: PMC9259695.
7. Liberini V. et al. Predictive value of baseline [18F]FDG PET/CT for response to systemic therapy in patients with advanced melanoma. J Clin Med. 2021 Oct 27;10(21):4994. doi: 10.3390/jcm10214994. PMID: 34768517; PMCID: PMC8584809.
8. Liberini V. et al. BSREM for brain metastases detection with [18F]FDG PET/CT in lung cancer patients. J Digit Imaging. 2022 Jun;35(3):581-593. doi:

10.1007/s10278-021-00570-y. Epub 2022 Feb 25. PMID: 35212859; PMCID: PMC9156589.

9. Liberini V. et al. Histopathological Features of Parathyroid Adenoma and [18F]F-Choline Uptake in PET/MR of Primary Hyperparathyroidism. Clin Nucl Med. 2022 Feb 1;47(2):101-107. doi: 10.1097/RLU.0000000000003987. PMID: 35006103.
10. Liberini V. et al. NSCLC Biomarkers to Predict Response to Immunotherapy with Checkpoint Inhibitors (ICI): From the Cells to In Vivo Images. Cancers (Basel). 2021 Sep 10;13(18):4543. doi: 10.3390/cancers13184543. PMID: 34572771; PMCID: PMC8464855.
11. Messerli M. et al. Clinical evaluation of data-driven respiratory gating for PET/CT in an oncological cohort of 149 patients: impact on image quality and patient management. Br J Radiol. 2021 Oct 1;94(1126):20201350. doi: 10.1259/bjr.20201350. Epub 2021 Sep 14. PMID: 34520673.
12. Liberini V. et al. Improved detection of in-transit metastases of malignant melanoma with BSREM reconstruction in digital [18 F]FDG PET/CT. Eur Radiol. 2021 Oct;31(10):8011-8020. doi: 10.1007/s00330-021-07852-7. Epub 2021 Mar 25. PMID: 33768288.
13. Liberini V. et al. The Future of Cancer Diagnosis, Treatment and Surveillance: A Systemic Review on Immunotherapy and Immuno-PET Radiotracers. Molecules. 2021 Apr 11;26(8):2201. doi: 10.3390/molecules26082201. PMID: 33920423; PMCID: PMC8069316.
14. Thuillier P. et al. Diagnostic value of both conventional PET parameters and radiomic features extracted from ^{18}F-FDG PET/CT for histologic subtype classification and characterization of lung neuroendocrine neoplasms. Biomedicines. 2021 Mar 10;9(3):281. doi: 10.3390/biomedicines9030281. PMID: 33801987; PMCID: PMC8001140.
15. Liberini V. et al. COVID-19 and Aspiration Pneumonia: Similar Pulmonary Findings with Different Diagnoses-a Pitfall in [18F]FDG PET/CT. SN Compr Clin Med. 2021 Jul 29:1-4. doi: 10.1007/s42399-021-01030-y. Epub ahead of print. PMID: 34345767; PMCID: PMC8321507.
16. Liberini V. et al. The Challenge of Evaluating Response to Peptide Receptor Radionuclide Therapy in Gastroenteropancreatic Neuroendocrine Tumors: The

Present and the Future. Diagnostics (Basel). 2020 Dec 12;10(12):1083. doi: 10.3390/diagnostics10121083.

17. Liberini V. et al. Impact of segmentation and discretization on radiomic features in 68Ga-DOTA-TOC PET/CT images of neuroendocrine tumor. EJNMMI Phys. 2021 Feb 27;8(1):21. doi: 10.1186/s40658-021-00367-6. PMID: 33638729; PMCID: PMC7914329.
18. Liberini V. et al. ^{68}Ga-DOTATOC PET/CT based radiomic analysis and PRRT outcome: a preliminary evaluation based on an exploratory radiomic analysis. Front Med (Lausanne). 2021 Jan 26;7:601853. doi: 10.3389/fmed.2020.601853.
19. Liberini V. et al. Impact of PET data driven respiratory motion correction of ^{68}Ga-DOTATATE PET/CT for differentiating neuroendocrine tumors (NET) and intrapancreatic accessory spleens (IPAS). Sci Rep 11, 2273 (2021). https://doi.org/10.1038/s41598-020-80855-4
20. Nervo A. et al. Bone metastases from differentiated thyroid carcinoma: current knowledge and open issues. J Endocrinol Invest. 2020 Aug 3. doi: 10.1007/s40618-020-01374-7.
21. Polverari G. et al. ^{18}F-FDG PET/CT Parameters and Radiomics Features Analysis in Advanced NSCLC treated with Immunotherapy as Predictors of Therapy Response and Survival. Cancers 2020, 12, 1163; doi:10.3390/cancers12051163.
22. Finessi M. et al. Major limits of dosimetrically determined activities in advanced differentiated thyroid carcinoma. Q J Nucl Med Mol Imaging. 2019 Sep; 63 (3): 258-266. doi: 10.23736/S1824- 4785.19.03211-4.
23. Liberini V. et al. ^{68}Ga-DOTA-TOC PET/CT: a typical case of von Hippel-Lindau disease. Clin Nucl Med. 2019 Feb; 44 (2): 125-126. doi: 10.1097/RLU.0000000000002395.
24. Motta et al. Undetectable antimicrobial plasma concentrations in an HIV-positive patient with protein-losing enteropathy and chylothorax during Mycobacterium genavense and Leishmania abdominal infections. J. Antimicrob Chemother, 2018 Feb 1;73(2):546-548. doi: 10.1093/jac/dkx385.

ABSTRACT

1. Liberini V. et al. Development of 3D-printed inserts for NEMA-phantom simulating necrotic tumor lesions for the evaluation of reproducibility of PET/CT radiomic features Abstracts book of the Annual Congress of the European Association of Nuclear Medicine – EAMN Annual Congress 2022 - TROP (Top Rated Oral Presentation) Session: Radiomics - Oral Presentation. Annual Congress of the European Association of Nuclear Medicine October 15-19, 2022 Barcelona, Spain. Eur J Nucl Med Mol Imaging 49 (Suppl 1), 1–751 (2022). https://doi.org/10.1007/s00259-022-05924-4.
2. Albano D. et al. [18F]FDG PET/CT role in FUO: an Italian multicentric study Abstracts book of the Annual Congress of the European Association of Nuclear Medicine – EAMN Annual Congress 2022. Annual Congress of the European Association of Nuclear Medicine October 15-19, 2022 Barcelona, Spain. Eur J Nucl Med Mol Imaging 49 (Suppl 1), 1–751 (2022). https://doi.org/10.1007/s00259-022-05924-4.
3. Evangelista L. et al. ITA-IMMUNO-PET: The Role Of FDG PET/CT In The Evaluation Of Response To Immunotherapy In Patient (PTS) With Lung Cancer (LG) And Malignant Melanoma (MM).Abstracts book of the Annual Congress of the European Association of Nuclear Medicine – EAMN Annual Congress 2022. Annual Congress of the European Association of Nuclear Medicine October 15-19, 2022 Barcelona, Spain. Eur J Nucl Med Mol Imaging 49 (Suppl 1), 1–751 (2022). https://doi.org/10.1007/s00259-022-05924-4.
4. Albano D. et al. 18F-FDG PET/CT role in FUO: an Italian Multicentric Study. 15th National Congress of the Italian Association of Nuclear Medicine and Molecular Imaging (AIMN). Clin Transl Imaging 10 (Suppl 1), 1–111 (2022). https://doi.org/10.1007/s40336-022-00492-x.
5. Balma M. et al. Interobserver agreement of [18F]PSMA-1007 PET/CT imagesaccording to the E-PSMA criteria in prostate cancer (PCA)patients with biochemical recurrence after primary surgery. 15th National Congress of the Italian Association of Nuclear Medicine and Molecular Imaging (AIMN). Clin Transl Imaging 10 (Suppl 1), 1–111 (2022). https://doi.org/10.1007/s40336-022-00492-x.

6. Nicolotti D.G. et al. [18F]PSMA-1007 PET/CT impact on decision-making strategiesfor prostate cancer patients with biochemical recurrence at lowPSA values after primary surgery: a retrospective preliminaryevaluation. 15th National Congress of the Italian Association of Nuclear Medicine and Molecular Imaging (AIMN). Clin Transl Imaging 10 (Suppl 1), 1–111 (2022). https://doi.org/10.1007/s40336-022-00492-x.
7. Buschiazzo A. et al. Monitoring treated brain neoplasms patients with 11C-MET PETand MRI: a retrospective sampling of discrepancies in evaluatingtreatment response or identifying focal relapse. 15th National Congress of the Italian Association of Nuclear Medicine and Molecular Imaging (AIMN). Clin Transl Imaging 10 (Suppl 1), 1–111 (2022). https://doi.org/10.1007/s40336-022-00492-x.
8. Evangelista L. et al. ITA-IMMUNO-PET: comparison between CT and FDG PET/CTin the evaluation of response to immunotherapy and their impacton the prognosis. 15th National Congress of the Italian Association of Nuclear Medicine and Molecular Imaging (AIMN). Clin Transl Imaging 10 (Suppl 1), 1–111 (2022). https://doi.org/10.1007/s40336-022-00492-x.
9. Bianchi A. et al. ITA-IMMUNO-PET: suspected adverse events correlatedto immunotherapy assessed by FDG PET/CT. 15th National Congress of the Italian Association of Nuclear Medicine and Molecular Imaging (AIMN). Clin Transl Imaging 10 (Suppl 1), 1–111 (2022). https://doi.org/10.1007/s40336-022-00492-x.
10. Evangelista L. et al. ITA-IMMUNO-PET: the prognostic role of baseline FDG PET/CT in patients candidates to immunotherapy. 15th National Congress of the Italian Association of Nuclear Medicine and Molecular Imaging (AIMN). Clin Transl Imaging 10 (Suppl 1), 1–111 (2022). https://doi.org/10.1007/s40336-022-00492-x.
11. De Rimini M.L. et al. ITA-IMMUNO-PET: the role of FDG PET/CT in the evaluationof response to immunotherapy. 15th National Congress of the Italian Association of Nuclear Medicine and Molecular Imaging (AIMN). Clin Transl Imaging 10 (Suppl 1), 1–111 (2022). https://doi.org/10.1007/s40336-022-00492-x.
12. Laudicella R. et al. [68GA]DOTATOC PET/CT machine-learning applicationsin the prediction of response in GEP-NETS undergoing[177LU]DOTATOC

PRRT: the ‘‘THERAGNOMICS’’ concept. 15th National Congress of the Italian Association of Nuclear Medicine and Molecular Imaging (AIMN). Clin Transl Imaging 10 (Suppl 1), 1–111 (2022). https://doi.org/10.1007/s40336-022-00492-x.

13. Liberini V. et al. Interobserver agreement for [18F]F-PSMA-1007 PET/CT images according to the E-PSMA criteria in prostate cancer patients. Journal of Nuclear Medicine. Vol. 63, Issue supplement 2. June 1, 2022.
14. Laudicella R. et al. [68GA]DOTATOC PET/CT machine-learning applicationsin the prediction of response in GEP-NETS undergoing[177LU]DOTATOC PRRT: the ‘‘THERAGNOMICS’’ concept. Journal of Nuclear Medicine. Vol. 63, Issue supplement 2. June 1, 2022.
15. Ceci F. et al. A0200 - Event-Free survival after 68Ga-PSMA-11 PET/CT in recurrent Hormone-Sensitive Prostate Cancer (HSPC) patients eligible for salvage therapy. European Urology, Volume 81, Supplement 1, 2022, Page S312, ISSN 0302-2838, https://doi.org/10.1016/S0302-2838(22)00287-1.
16. Liberini V. et al. Parathyroid Histopathology and [18F]F-Choline Uptake in PET/MR in Primary Hyperparathyroidism. Abstracts book of the Annual Congress of the European Association of Nuclear Medicine – EAMN Annual Congress 2021 - TROP (Top Rated Oral Presentation) Session: Nuclear Medicine Imaging and Therapy in Thyroid and Parathyroid Disorders. European Association of Nuclear Medicine October 20-23, 2021 Virtual. Eur J Nucl Med Mol Imaging 48 (Suppl 1), 1–648 (2021). https://doi.org/10.1007/s00259-021-05547-1.
17. Thuillier P. et al. Prognostic value of whole-body PET volumetric parameters extracted from 68Ga-DOTATOC-PET/CT in well-differentiated neuroendocrine tumors. Abstracts book of the Annual Congress of the European Association of Nuclear Medicine – EAMN Annual Congress 2021 - Clinical Oncology Track – TROP (Top Rated Oral Presentation) Session: Neuroendocrine- Oral Presentation. European Association of Nuclear Medicine October 20-23, 2021 Virtual. Eur J Nucl Med Mol Imaging 48 (Suppl 1), 1–648 (2021). https://doi.org/10.1007/s00259-021-05547-1.
18. Liberini V. et al. Predictive value of baseline [18F]FDG PET/CT for response to systemic therapy in patients with advanced melanomas. Abstracts book of the Annual Congress of the European Association of Nuclear Medicine – EAMN

Annual Congress 2021 - Clinical Oncology Track - TROP (Top Rated Oral Presentation) Session: Gynaecological and Melanoma - Oral Presentation. European Association of Nuclear Medicine October 20-23, 2021 Virtual. Eur J Nucl Med Mol Imaging 48 (Suppl 1), 1–648 (2021). https://doi.org/10.1007/s00259-021-05547-1.

19. Liberini V. et al. BSREM for Brain Metastases Detection with [18F]FDG PET/CT in Lung Cancer Patients. Abstracts book of the Annual Congress of the European Association of Nuclear Medicine – EAMN Annual Congress 2021 - Cutting Edge Science Track - Featured Session: PET Reconstructions and Corrections - Oral presentation. European Association of Nuclear Medicine October 20-23, 2021 Virtual. Eur J Nucl Med Mol Imaging 48 (Suppl 1), 1–648 (2021). https://doi.org/10.1007/s00259-021-05547-1.
20. Thuillier P. et al. Valeur pronostique des paramètres volumétriques corps entier extraits de la TEP/TDM au 68Ga-DOTATOC dans les tumeurs neuroendocrines bien différenciées. Annales d'Endocrinologie, Volume 82, Issue 5, 2021, Page 274, ISSN 0003-4266, https://doi.org/10.1016/j.ando.2021.08.056.
21. Thuillier P. et al. Valeur prédictive des paramètres volumétriques corps entier et osseux de la 18F-FDG-TEP/TDM préthérapeutique dans la réponse au Lenvatinib chez les patients traités pour un cancer différencié de la thyroïde réfractaire à l'iode. Annales d'Endocrinologie, Volume 81, Issue 4, 2020, Page 251, ISSN 0003-4266, https://doi.org/10.1016/j.ando.2020.07.293.
22. Liberini V. et al. Impact of PET data driven respiratory motion correction of ^{68}Ga-DOTATATE PET/CT for differentiating neuroendocrine tumors (NET) and intrapancreatic accessory spleens (IPAS). EJNMMI. September 2020; vol 47 (suppl 1): 1-753. Abstracts book of the Annual Congress of the European Association of Nuclear Medicine – Oral presentation.
23. Polverari G. et al. ^{18}F-FDG PET Parameters and Radiomics Features Analysis in Advanced NSCLC treated with Immunotherapy as Predictors of Therapy Response and Survival. EJNMMI. September 2020; vol 47 (suppl 1): 1-753. Abstracts book of the Annual Congress of the European Association of Nuclear Medicine – Oral presentation.
24. Califaretti E. et al. ^{18}F-FDG PET/CT whole body volumetric evaluation in iodine-refractory differentiated thyroid cancer as predictors of Lenvatinib response. EJNMMI. September 2020; vol 47 (suppl 1): 1-753. Abstracts book of

the Annual Congress of the European Association of Nuclear Medicine – Oral presentation.

25. Liberini V. et al. Peptide Receptor Radionuclide Therapy (PRRT) Putcome Prediction in Neuroendocrine Tumors (NET): Could Radiomic Features Analysis of 68Ga-DOTATOC PET/CT Have a Roll? Neuroendocrinology 2020. Vol. 110 (suppl 1). Abstracts of the 17th Annual ENETS Conference for the Diagnosis and Treatment of Neuroendocrine Tumor Disease.
26. Liberini V. et al. Robustness of Radiomic Features in 68Ga-DOTATOC PET/CT: A Monocentric Experience for Neuroendocrine Tumors. Neuroendocrinology 2020. Vol. 110 (suppl 1). Abstracts of the 17th Annual ENETS Conference for the Diagnosis and Treatment of Neuroendocrine Tumor Disease.
27. Liberini V. et al. A Study of Radiomic Features Robustness for 68Ga-DOTATOC PET/CT in Neuroendocrine Tumors. EJNMMI. October 2019; vol 46 (suppl 1): 1-952. Abstracts book of the Annual Congress of the European Association of Nuclear Medicine – Oral Presentation.
28. Nicolotti D. et al. Impact of late pelvic acquisition on 68Ga-PSMA-11 PET/CT positivity rate and inter-rter reliability analysis. EJNMMI. October 2019; vol 46 (suppl 1): 1-952. Abstracts book of the Annual Congress of the European Association of Nuclear Medicine.
29. Ceci F. et al. 68Ga-PSMA-11 PET/CT in hormone-naïve recurrent prostate cancer: prospective, single-center study in patients eligible for salvage therapy. EJNMMI. October 2019; vol 46 (suppl 1): 1- 952. Abstracts book of the Annual Congress of the European Association of Nuclear Medicine.
30. Ceci F. et al. Salvage radiotherapy guided by 68Ga-PSMA-11 PET/CT in patients with biochemical persistence (BCP) after radical prostatectomy for prostate cancer. EJNMMI. October 2019; vol 46 (suppl 1): 1-952. Abstracts book of the Annual Congress of the European Association of Nuclear Medicine.
31. Finessi M. et al. Comparison of 68Ga DOTATOC PET/CT with morphological imaging in staging of neuroendocrine tumors. EJNMMI. October 2019; vol 46 (suppl 1): 1-952. Abstracts book of the Annual Congress of the European Association of Nuclear Medicine.
32. Pilati E. et al. Impact of 68Ga DOTATOC PET/CT in the Therapeutic Management of Neuroendocrine Tumors. EJNMMI. October 2019; vol 46

(suppl 1): 1-952. Abstracts book of the Annual Congress of the European Association of Nuclear Medicine.

33. Liberini V. et al. Can texture analysis be used for a vivo “imaging biopsy” in neuroendocrine tumors? A first step feasibility study with 68Ga-DOTATOC PET/CT. Neuroendocrinology 2019; 108 (suppl 1): I-X. Abstracts of the 16th Annual ENETS Conference for the Diagnosis and Treatment of Neuroendocrine Tumor Disease.
34. Pilati E. et al. Impact of 68Ga DOTATOC PET/CT in the therapeutic management of neuroendocrine tumors. Clin Transl Imaging (2019), vol 7 (Supp 1): S1-S138. AIMN XIV Annual Congress Abstract.
35. Liberini V. et al. Can texture analysis be used for a vivo “imaging biopsy” in neuroendocrine tumors? A first step feasibility study with 68Ga-DOTATOC PET/CT. Clin Transl Imaging (2019), vol 7 (Supp 1): S1-S138. AIMN XIV Annual Congress Abstract – selected for highlight.
36. Liberini V. et al. A strange case of multiple fractures: a case report. Clin Transl Imaging (2017), vol 5 (Suppl 1): S1–S153. AIMN XIII Annual Congress Abstract.
37. Liberini V. et al. The role of lymphoscintigraphy in the diagnosis of lymphocele after renal transplant: a case report. Clin Transl Imaging (2017), vol 5 (Suppl 1): S1–S153. AIMN XIII Annual Congress Abstract.
38. Balma M. et al. The role of ^{123}I-FP- CIT SPECT in the study of the serotonergic system in amyotrophic lateral sclerosis: a potential aid in understanding etiopathogenesis. Clin Transl Imaging (2017), vol 5 (Suppl 1): S1–S153. AIMN XIII Annual Congress Abstract.
39. Galati A. et al. FP- CIT gender differences. Removing the background to focus on the target. Clin Transl Imaging (2017), vol 5 (Suppl 1): S1–S153. AIMN XIII Annual Congress Abstract.

BOOK CHAPTER

1. Liberini V., Finessi M. et Deandreis D. (2021) A Patient with Follicular Thyroid Cancer and a Painful Bone Metastases at Risk for Pathologic Fracture. Chapter pp 275-295. Thyroid Cancer. A case-based approach. II edition. Editors: Giorgio Grani, David S. Cooper, Cosimo Durante. Springer. https://doi.org/10.1007/978-3-030-61919-0_31
2. Finessi M., Liberini V. et Deandreis D. (2020) Cancer staging with 18F-FDG PET/CT in hyperglycemic patients. Chapter pp 641-654. Obesity and Diabetes. Editors: Faintuch J., Faintuch S. (eds) Springer, Cham. https://doi.org/10.1007/978-3-030-53370-0_47